FIRST PRINCIPLES STUDY OF STRUCTURAL AND ELECTRONIC PROPERTIES OF SOME SELECTED HALIDE PEROVSKITE MATERIALS

Narasak Pandech

A Thesis Submitted in Partial Fulfillment of the Requirements for the

Degree of Doctor of Philosophy in Physics

Suranaree University of Technology

Academic Year 2019

การศึกษาสมบัติเชิงโครงสร้างและอิเล็กทรอนิกส์ของสารกลุ่มแฮไลด์เพอรอฟสไกต์บางชนิดโดยวิธีเฟิร์สพรินซิเพิล

นายณราศักดิ์ พันเดช

วิทยานิพนธ์นี้เป็นส่วนหนึ่งของการศึกษาตามหลักสูตรปริญญาวิทยาศาสตรดุษฎีบัณฑิต
สาขาวิชาฟิสิกส์
มหาวิทยาลัยเทคโนโลยีสุรนารี
ปีการศึกษา 2562

FIRST PRINCIPLES STUDY OF STRUCTURAL AND ELECTRONIC PROPERTIES OF SOME SELECTED HALIDE PEROVSKITE MATERIALS

Suranaree University of Technology has approved this thesis submitted in partial fulfillment of the requirements for the Degree of Doctor of Philosophy.

Thesis Examining Committee

_____

(Assoc. Prof. Dr. Panomsak Meemon)

Chairperson

_____

(Assoc. Prof. Dr. Sirichok Jungthawan)

Member (Thesis Advisor)

_____

(Prof. Dr. Sukit Limpijumnong)

Member

_____

(Assoc. Prof. Dr. Jiraroj T-Thienprasert)

Member

_____

(Asst. Prof. Dr. Suwit Suthirakun)

Member

_____
(Assoc. Prof. Dr. Chatchai Jothityangkoon)

Vice Rector for Academic Affairs

and Quality Assurance

_____
(Prof. Dr. Santi Maensiri)

Dean of Institute of Science

ฉราศักดิ์ พันเดช : การศึกษาสมบัติเชิงโครงสร้างและอิเล็กทรอนิกส์ของสารกลุ่มแฮไลด์เพอรอฟสไกต์บางชนิดโดยวิธีเฟิร์สพรินซิเพิล (FIRST PRINCIPLES STUDY OF STRUCTURAL AND ELECTRONIC PROPERTIES OF SOME SELECTED HALIDE PEROVSKITE MATERIALS) อาจารย์ที่ปรึกษา : รองศาสตราจารย์ ดร.สิริโชค จึงถาวรรณ, 154 หน้า.

ในวิทยานิพนธ์ฉบับนี้ได้มีการศึกษาคุณสมบัติเชิงโครงสร้างและอิเล็กทรอนิกส์ของสารประกอบแฮไลด์เพอรอฟสไกต์ ABX_3, (A = CH_3NH_3 หรือ เมทิลแอมโมเนียมโมเลกุล; B = Pb, Sn, Ge; X = I, Br, Cl) โดยวิธีคำนวณแบบเฟิร์สพรินซิเพิล (first-principles) หรือ แอบ อินิชิโอ (*ab initio*) ค่าอันตรกิริยาของ แวน เดอร์ วาลส์ (van der Waals interaction) ได้ถูกพิจารณาร่วมด้วยกับระเบียบวิธีคำนวณแบบเฟิร์สพรินซิเพิล เพื่อศึกษาผลของตัวแปรนี้ต่ออันตรกิริยาภายในระหว่างเมทิลแอมโมเนียมโมเลกุลและ โครงสร้างของ BX_6 ในสารเพอรอฟสไกต์ดังกล่าว ผลการศึกษาพบว่าอันตรกิริยาภายในระหว่างเมทิลแอมโมเนียมโมเลกุลและโครงสร้างของ BX_6 มีอิทธิพลต่อการวางตัวและตำแหน่งของเมทิลแอมโมเนียมโมเลกุลซึ่งส่งผลให้โครงสร้างของ BX_6 เกิดการบิดเบี้ยว และมีผลต่อโครงสร้างและคุณสมบัติอิเล็กทรอนิกส์ของสารกลุ่มนี้ โดยสามารถเปลี่ยนลักษณะของโครงสร้างแถบพลังงานจากช่องว่างพลังงานแบบตรง (direct bandgap) ไปเป็นช่องว่างพลังงานแบบไม่ตรง (indirect bandgap) และความน่าเชื่อถือของการศึกษานี้ยืนยันได้จากการคำนวณโดยฟังก์ชันนัลลูกผสม (hybrid functional) และการคำนวณแบบความต้องกันตนเองแบบจีดับเบิลยู (self-consistent GW) รวมกับการพิจารณาผลจากการคู่ควบสปิน-วงโคจร (spin-orbit coupling) ด้วย

สาขาวิชาฟิสิกส์   ลายมือชื่อนักศึกษา _____

ปีการศึกษา 2562   ลายมือชื่ออาจารย์ที่ปรึกษา _Sirichok_
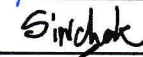
ลายมือชื่ออาจารย์ที่ปรึกษาร่วม _____

NARASAK PANDECH : FIRST-PRINCIPLES STUDY OF STRUCTURAL AND ELECTRONIC PROPERTIES OF SOME SELECTED HALIDE PEROVSKITE MATERIALS. THESIS ADVISOR : ASSOC. PROF. SIRICHOK JUNGTHAWAN, 154 PP.

STRUCTURAL/ELECTRONIC PROPERTIES/HALIDE PEROVSKITES/FIRST PRINCIPLES

In this thesis, the structural and electronic properties of selected halide perovskite materials ABX_3, (A = CH_3NH_3 shortly MA^+; B = Pb, Sn, Ge; X = I, Br, Cl) were studied using first principles (or *ab initio*) methods. Van der Waals (vdW) correction to DFT is considered for revealing the effects of the internal interactions between the MA^+ cation and the BX_6 inorganic framework. Our results reveal that the vdW-interactions between the MA^+ cation and the inorganic framework can strongly affect the optimized orientation and position of the molecule and the resulting distortion of the inorganic framework. Consequently, it also affects the electronic properties of the materials and specifically can change the band structure from direct to indirect bandgap. The robustness of this result is studied by comparing hybrid functional calculations and quasiparticle self-consistent GW calculations as well as spin-orbit coupling.

School of Physics

Academic Year 2019

Student's Signature _Narasak_

Advisor's Signature _Sirichok_

Co-advisor's Signature _____

ACKNOWLEDGEMENTS

CONTENTS

CONTENTS (Continued)

CONTENTS (Continued)

LIST OF TABLES

LIST OF TABLES (Continued)

LIST OF FIGURES

LIST OF FIGURES (Continued)

LIST OF FIGURES (Continued)

LIST OF FIGURES (Continued)

LIST OF FIGURES (Continued)

LIST OF FIGURES (Continued)

LIST OF FIGURES (Continued)

LIST OF ABBREVIATIONS

DSSCs   = Dye-sensitized solar cells

PCEs   = power conversion efficiencies

FP-LMTO   = full-potential linearized muffin-tin orbital

DFT   = Density Functional Theory

GGA   = Generalized Gradient Approximation

LDA   = Local Density Approximation

HSE   = Heyd-Scuseria-Ernzerhof

SOC   = spin-orbit coupling

MA   = Methylammonium

PAW   = Projector Augmented Wave

PBE   = Perdew-Burke-Ernzerhof

PWs   = Plane-waves

USPPs   = Ultra Soft Pseudo Potentials

VASP   = Vienna *Ab-initio* Simulation Package

CHAPTER I

INTRODUCTION

1.1   Motivation

Human heavily and increasingly used fossil fuel for power in daily life. This causes deterioration of the environment, leading to many problems such as the global warming, particulate pollutant (2.5 microns or smaller in size), and air and water pollutions. Moreover, the main fossil fuels, such as coal, oil, and natural gas reserves are getting lower in the next few decades. Therefore, alternative energy resources are the urgent task for a sustainable world. Photovoltaic solar cell is one of the most promising approaches of havesting solar energy by conversion of solar energy into electricity.

The development of solar cells has been achieved from decades ago. Presently, dye-sensitized solar cells (DSSCs), the third-generation solar cells, have attracted a great attention due to their easy and low-cost fabrication and relatively high efficiency followed the first two generations, Si-based and Cd-based solar cells (O'Regan and Grätzel, 1991; Tang, 1986; Yu *et al.*, 1995). Recent development of DSSCs is the introduction of organic-inorganic halide perovskites such as $CH_3NH_3PbI_3$ (MAPbI$_3$) as the absorber layer in DSSCs (Kojima *et al.*, 2009). It attracted vast attention on account of a significant improvement in power conversion efficiencies (PCEs) that have risen from 4% up to 22% in a short period of research time (Im *et al.*, 2011; Kim *et al.*, 2012; Lee *et al.*, 2012; Burschka *et al.*, 2013).

Perovskites of the general formula ABX_3 have played a central role in the evaluation of materials chemistry and condensed matter physics over the last 70 years (Kieslich *et al.*, 2014). This family of solid-state materials covers a wide range of intriguing properties, including both application-oriented phenomena and fundamental physics and chemistry (Kieslich *et al.*, 2015).
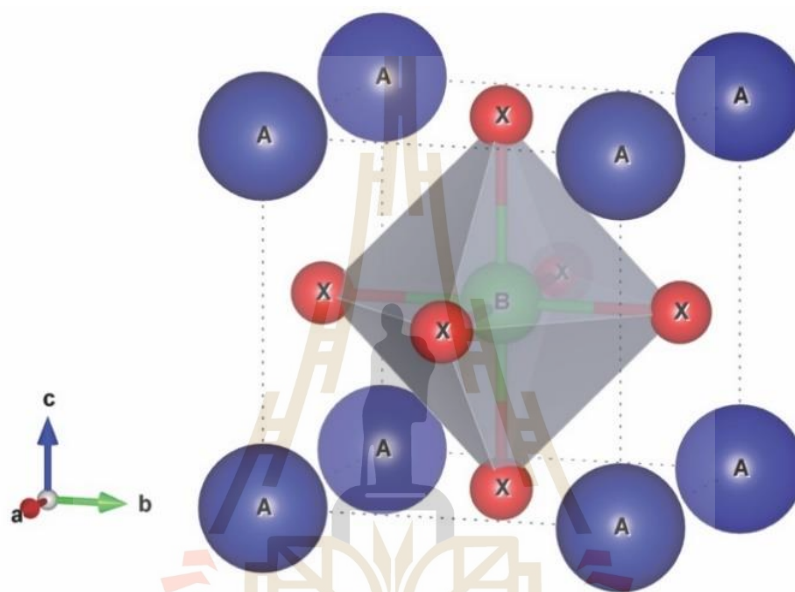
Figure 1.1 Illustration of the ideal cubic ABX_3 perovskite structure. Monovalent *A*-site cation, divalent *B*-site cation, and *X*-site anions are located at the corner of the unit cell (deep blue sphere), at the body center of the unit cell (green sphere), and at the face center of the unit cell (red sphere), respectively.

By definition, a perovskite generally refers to a class of materials with chemical formula ABX_3 with the crystal structure shown in Figure 1.1. Calcium titanium oxide ($CaTiO_3$) is an example of materials with such structure. Perovskites take their name from the natural mineral, which was discovered in 1839 and named after mineralogist L.A. Perovski (1792-1856) (De Graef and McHenry, 2012). The ideal cubic perovskite

structure (as illustrated in Figure 1.1) which consists of a monovalent A-site cation (deep blue sphere) located at the corner of the unit cell, a divalent B-site cation (green sphere) located at the body center of the unit cell, and X-site anions (red sphere) located at the face center of the unit cell. Victor Goldschmidt was the first to describe the perovskite crystal structure by using the concept of tolerance factor (Goldschmidt, 1926). In ideal cubic-symmetry perovskites, the B cation is in 6-fold coordination, surrounded by an octahedron of the X anions, and the A cation is in 12-fold cuboctahedral coordination. A- and B-cations are different positive charges compensated by the negative X-anions. The size of the ions has to obey the Goldschmidt criterion. The detail of the Goldschmidt condition is discussed further in Section 3.2

Materials with perovskite structure are very common because of the adaptability of this structure toward A, B, or X site substitution, which allows for the great variability in materials and properties (Kieslich *et al.*, 2014). The most abundant inorganic perovskites are oxides (ABO_3) which have many interesting properties, including phase transition, ferroelectricity, supper-conductivity, elastic properties etc. (Tao and Irvine, 2006; Scott *et al.*, 2008; Pérez-Tomas *et al.*, 2019; Lu *et al.*, 2018; Tao *et al.*, 2004; Lan *et al.*, 2016). Previously, we used the first principles calculation to study some interesting properties such as elastic properties of oxide perovskites (ABO_3). The pressure-dependent of sound velocities and elastic properties of the cubic PbBO_3 (B = Ti, Zr) under pressure were studied (Pandech *et al.*, 2013). The elastic constants of cubic phase of perovskite ATiO$_3$ (A = Be, Mg, Ca, Sr, and Ba) and PbBO_3 (B = Ti, Zr, and Hf) were systematically calculated by using the energy-strain relation. The calculations of elastic constants by using the energy-strain relation were explained in detail by using the SrTiO$_3$ as an illustration case (Pandech *et al.*, 2016). The elastic

constants have found to be linearly increased with the applied pressure. The effects of cation species on the elastic properties were also investigated (Pandech $et\ al.$, 2015). The compressive elastic constant, (C_{11}) is maximum when the cation atoms A and B have comparable size. Oxide perovskites (ABO$_3$) are fastinated materials and there are some interesting properties worth to be explored such as the electronics properties under pressure (Tariq $et\ al.$, 2015; Liu $et\ al.$, 2011).

Perovskite compounds may refer to the compound ABX_3 having similar structure as ABO$_3$. Some perovskite structures can form with sulfur (or other group VI elements) (Snyder $et\ al.$, 1992). More common alternatives to oxide are obtained by replacing oxygen atoms with atoms of group VII, for examples of fluorides (such as NaMgF$_3$, KMgF$_3$ and KZnF$_3$). Particularly relevant is also the group of organic and/or inorganic halide perovskites (e.g., CsPbI$_3$, CH$_3$NH$_3$PbI$_3$, CH$_3$NH$_3$PbB$_3$, and CH$_3$NH$_3$PbCl$_3$) can be formed (Poglitsch and Weber, 1987).

The class of perovskite materials so-called halide perovskites has been known for decades and has been studied, in particular, on dielectric properties (Weber, 1978; Poglitsch and Weber, 1987; Xu $et\ al.$, 1991). However, in 2009, this class of materials has been used in solar cell application for the first time by Miyasaka' s research group (Kojima $et\ al.$, 2009). They fabricated the light absorber part based on A = CH$_3$NH$_3$ (Methylammonium, MA), B = Pb and X = Br or I in a dye-sensitized solar cell as shown in Figure 1.2. The power conversion efficiency (PCE) of their solar cell was only 3.8% and the cell was stable for only a few minutes due to a corrosive liquid electrolyte. After the work of Miyasaka, a few research groups attempted to improve the PCE and the stability of halide perovskite solar cell, but a few improvements of PCE to 6.5% by Park's group in 2011 (Im $et\ al.$, 2011). However, because the advantage in low cost of

materials and simple to manufacture of the halide perovskite solar cell, then there are three breakthroughs which triggered and renewed interest in the halide perovskite solar cell research in 2012. First, Kanatzidis' research group (Chung *et al.*, 2012) used $A =$ Cs instead of MA to solve the stability of the perovskite solar cell and achieved more than 10% PCE. After that, in August of the same year, Park's research group in South Korea cooperated with Grätzel's research group in Switzerland reported 9.7% of PCE with 500 hours of stability in $CH_3NH_3PbI_3$ (Kim *et al.*, 2012). In October 2012, Snaith and Miyasaka 's research groups (Lee *et al.*, 2012) reported that the halide perovskite was stable if put it in contact with a solid-state hole transporter and reported 10.9% of PCE. In 2013, 15% PCE perovskite solar cell was achieved in Grätzel's research (Burschka *et al.*, 2013) by using mesoscopic/sensitized architecture and in Snaith's research group (Docampo *et al.*, 2013) by using planar architecture. In 2014, Yang's research group (Zhou *et al.*, 2014) reported about 19.3% PCE in their planar thin-film-architecture-based solar cell and in the same year the National Renewable Energy Laboratory (NREL) reported a non-stability efficiency of 22.1% from the researchers in Korea Research Institute of Chemical Technology (KRICT) in early 2016 (National Renewable Energy Laboratory, 2016; Polman *et al.*, 2016). From the pioneer work of Miyasaka *et al.*, the PCE of halide perovskite solar cells significantly improved from 3.8% to above 20% in year 2009 to 2016, making them the new type of photovoltaic materials.
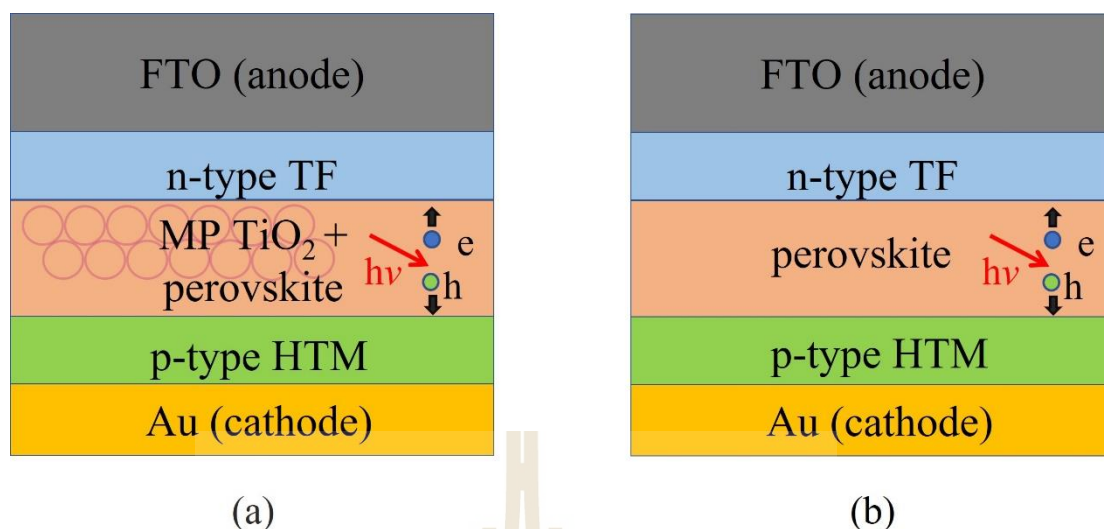
Figure 1.2 (a) Mesoscopic/sensitized halide perovskite solar cell with mesoporous (MP) TiO2. (b) Planar halide perovskite solar cell without a mesoporous TiO2 layer. FTO, TF, and HTM stand for fluorine doped tin oxide (FTO), thin film (TF), and hole transporting material (HTM) (Jung and Park, 2015).

Although the halide perovskite solar cells achieve the great PCE, however, the fundamental reasons behind the successive PCE of the halide perovskite solar cells are still not well understood and under controversy. The present of the organic molecules, $CH_3NH_3^+$, leads to the complicated crystal structure of the materials. Especially, at a high-temperature range, the molecules are randomly re-oriented. The influences of molecular orientations on the structural and electronic properties are rarely investigated. Even though, some works attempt to understand the effect of the organic molecule, MA^+ cation on the physical properties of these materials. For examples, Bechtel *et al.* (Bechtel *et al.*, 2016) performed the density functional theory (DFT) for the MAPbI3 to mapping out the energy landscape of the MA^+ cation as a function of molecular rotational variables, such as a polar angle θ and azimuthal angle ϕ of the CN

axis of the molecule vs. the [001] and [100] cubic axes, the rotation angle α of the molecule about its axis and also the displacement of the molecule from its center along its axis. Their main finding is that the displacement of the molecule and the translation along its direction away from the nominal center of the dodecahedral site are quite important. The optimum orientations found in their work are close to [100] and [111] directions. But in their work, the main inorganic framework of Pb-I is kept being as a simple cubic structure. In reality, the rotation of MA^+ cation can distort the structure and might change the electronic properties of these materials. Motta *et al*. (Motta *et al.*, 2015) also performed the DFT study of molecular orientations on the structural and electronic properties of the $MAPbI_3$. It has been found that the molecular orientations are sensitive to the initial orientation of the molecule being along [100] or [111]. The molecule will rotate from [100] orientation toward [110] or equivalent direction and consequently affect the electronic band structure of the material. Base on these two works, the high temperature, α-phase is considered. Quarti *et. al*. (Quarti *et al.*, 2014) present the DFT study of an interplay of orientational order and electronic properties of the room temperature, β-phase of $MAPbI_3$. In their work, various orientations of the MA^+ cations are considered, such as a polar (ferroelectric) structures with the MA^+ orientations giving rise to a net dipole alignment and other an apolar (antiferroelectric) structures with the MA^+ orientations giving a non-dipole alignment. They found that a ferroelectric-like orientations which leading to a quasi *I4cm* structure are preferred stability structure than that antiferroelectric structure.

1.2   Research Objectives

In this thesis, we have conducted a van der Waals-corrected density functional theory (vdW-DFT) calculations to examine the importance of vdW interactions on the structural parameters and the electronic properties of the studied halide perovskite materials. The selected materials are $CH_3NH_3BX_3$ (B = Pb, Sn, Ge and X = I, Br, Cl).

The structural relaxation and electronic band structure calculations are carried out by using the Perdew-Burke-Ernzerhof (PBE) exchange-correlation functionals. It is well known that even the PBE with vdW corrected DFT can significantly underestimate the gap. Therefore, the more accurate Heyd-Scuseria-Ernzerhof (HSE) screened hybrid functional (HSE06) and the quasiparticle self-consistent GW method are used to calculate the band structures. The investigation on the calculation results obtained from different level of functionals will be discussed.

Finally, spin-orbit coupling is known to be important in particular in the Pb- and Sn-based compounds thus, the effect of both GW self-energy corrections and spin-orbit coupling (SOC) on the electronic structure in relation to the orientation of the MA molecules and their corresponding induced structural distortions are studied. The SOC can induce symmetry breaking and affect the location of CBM in k-space.

1.3   Thesis Outline

This thesis covers the theoretical study of structural and electronic properties of selected halide perovskite materials, ABX_3 (A = CH_3NH_3 : B = Pb, Sn, Ge: X = Cl, Br, I). The calculations are performed within the framework of DFT as implemented in Vienna *Ab initio* Simulation Package (VASP). The exchange-correlation functional of Perdew, Burke and Ernzerhof (PBE) is used for structural relaxation. The non-local

hybrid exchange-correlation function (HSE06) is used for electronic structure calculations. Additionally, the band structures are calculated by using the all electron full-potential linearized muffin-tin orbital (FP-LMTO) method as implemented in Questaal Suite (https://www.questaal.org.). The calculated results with different level of functionals are discussed.

Chapter II, the theoretical approaches used in this thesis are discussed in detail. It begins with the introduction to the density functional theory (DFT) and its requirements. The approximations methods used in DFT are discussed.

Chapter III covers the calculation of structural parameters compared with other theoretical and experimental values, crystal structures, formability, and phases transition of studied halide perovskite materials.

Chapter IV covers the effects of the methylammonium cation rotations on the structural and electronic properties of studied materials. The influences of van der Waals-correction on DFT calculations and the calculated results with different level of functionals are discussed in detail.

Chapter V, the main findings in this work are summarized. Based on our results, future interesting researches on structural and electronic properties of halide perovskite materials are suggested for various applications.

CHAPTER II

THEORETICAL APPROACH

For atomistic calculations of materials, in-depth information could be derived from the electron wave functions. In principle, the electronic wave functions of the system are obtained by solving many-body Schrödinger equations. However, in practice, it is nearly impossible to directly solve the full set of Schrödinger equations of the many-electrons problem. The method of approximations is need to simplify the complicated many-body problems into solvable ones. In this chapter, the theories, approximation methods, and software used in this thesis are briefly explained.

2.1 Electronic Structure Problem

A central goal of most electronic structure theories is to seek for the solution to the non-relativistic time-independent many-body Schrödinger equation as,

$$H\Psi\left(\{R_A\},\{r_i,\sigma_i\}\right) = E\Psi\left(\{R_A\},\{r_i,\sigma_i\}\right). \tag{2.1}$$

For a system containing M nuclei and N electrons, the many-body wavefunction (Ψ) is a function of all spatial coordinates of nuclei ($\{R_A\}, A = 1, 2, ...M$). The Hamiltonian (H) is a sum of all possible interactions between electrons and nuclei. In the atomic unit, H can be expressed as,

$$H = -\sum_{i=1}^{N}\frac{\nabla_i^2}{2} - \sum_{A=1}^{M}\frac{\nabla_A^2}{2M_A} + \sum_{i=1}^{N}\sum_{j>i}^{N}\frac{1}{|r_i-r_j|} + \sum_{A=1}^{M}\sum_{B>A}^{M}\frac{Z_A Z_B}{|R_A-R_B|} - \sum_{i=1}^{N}\sum_{A=1}^{M}\frac{Z_A}{|r_i-R_A|}. \tag{2.2}$$

Where M_A is the ratio of the mass of nucleus A to the mass of an electron, and Z_A is the atomic number of nucleus A. The ∇_i^2 and ∇_A^2 are the Laplacian operators. The first two terms in the Eq. 2.2 represent the kinetic energies of all electrons and nuclei, respectively. The third and fourth term are the Coulomb repulsion between electrons and between nuclei, respectively. The fifth term is the Coulomb attraction between electrons and nuclei. The time-independent many-body Schrödinger equation in Eq. 2.1 is relatively simple but nearly impossible to solve (Martin, 2004). There are numerous attempts to find reasonable approximations to reduce the complexity. The first well known important approximation is the Born-Oppenheimer approximation (Born and Oppenheimer, 1927) obtained by decoupling the dynamics of the electrons and nuclei.

2.2 Born-Oppenheimer Approximation

Considering Newton's law of motion, a proton mass is approximately 2000 times larger than the mass of an electron. Therefore, the electrons are much lighter than the nuclei such that the timescale of the dynamical response of the electrons is a few orders of magnitude faster than that of nuclei. Basically, this allows us to separate or decouple the dynamics of the electrons and the nuclei. This modest approximation is called the *Born-Oppenheimer approximation*. In practice, the nuclei are treated as static classical particles with respect to the electrons that are treated as quantum particles. As a result, the kinetic energies of nuclei (the second term of Eq. 2.2) can be neglected and the potential energies arising from Coulomb repulsion between nuclei (the fourth term of Eq. 2.2) is a constant for fixed configuration of the nuclei. The full Hamiltonian in Eq. 2.2 is reduced to the electronic Hamiltonian (H_e),

$$H_e = -\sum_{i=1}^{N} \frac{\nabla_i^2}{2} + \sum_{i=1}^{N} \sum_{j>i}^{N} \frac{1}{|r_i - r_j|} - \sum_{i=1}^{N} \sum_{A=1}^{M} \frac{Z_A}{|r_i - R_A|}. \tag{2.3}$$

The solution to above Schrödinger equation involving the electronic Hamiltonian (H_e) becomes

$$H_e \Psi_e \left(\{R_A\}, \{r_i, \sigma_i\} \right) = E_e \Psi_e \left(\{R_A\}, \{r_i, \sigma_i\} \right). \tag{2.4}$$

In Eq. 2.4, the electronic wavefunction (Ψ_e) depends on nuclear coordinates ($\{R_A\}$) only parametrically, thus the configuration of nuclei $\{R_A\}$ can be fixed. For simplicity, electronic spatial and spin coordinates ($\{r_i, \sigma_i\}$) can be put together into one variable $\{x_i\}$ (i.e., $\{x_i\} = \{r_i, \sigma_i\}$) and the Eq. 2.4 can be rewritten as

$$H_e \Psi_e \left(\{x_i\} \right) = E_e \Psi_e \left(\{x_i\} \right). \tag{2.5}$$

The total energy for some fixed configurations of the nuclei including the constant nuclear repulsion term leads to,

$$E_{Total} = E_e + \sum_{A=1}^{M} \sum_{B>A}^{M} \frac{Z_A Z_B}{|R_A - R_B|}. \tag{2.6}$$

With the Born-Oppenheimer approximation, the electronic structure problem is reduced to solving less complicated problem, Eq. 2.5. Note that, the Born-Oppenheimer approximation is certainly not universally valid and it may break down in some cases when there are multiple potential energy surfaces close to each other in energy. Since the motion of the electrons is correlated to each other, which essentially requires the treatment of 3^N variables for an N-electrons system, this makes the Schrödinger equation involving the electronic Hamiltonian (H_e) still complex. The main concern is how to properly describe the interactions between the electrons. Many approximate

methods have been developed to solve Schrödinger or Schrödinger-like equations by mapping the *N*-electron Schrödinger equation into one-electron Schrödinger equations moving in an effective potential that are feasible to solve. The approximation schemes can be divided into two main approaches: (i) the wavefunction based methods, where the many-electron wavefunction is the central variable, for example, the Hartree-Fock approximation (Hartree, 1928), and (ii) density-functional theory (DFT), where the electron density is treated as the central entity rather than the many-body wavefunction.

2.3   Density Functional Theory

The density functional theory (DFT) is the widely adopted method to describe the interactions between the electrons in the many-electron Schrödinger equation. The key idea of DFT is to describe the complicated many-body electron interactions through its density $n(\vec{r})$ instead of its wavefunction ψ_i. Using the electron density $n(\vec{r})$ over the electron wavefunction offers a great advantage of much-reduced dimensionality. In contrast to the many-body wavefunction, the electron density always depends on 3-dimension regardless of the number of electrons in the system. The DFT has become the most widely used electronic structure method nowadays especially in the computational materials science and condensed matter physics community.

The DFT has been successively applied to wide range of material structures such as standard bulk materials, nanostructures, molecules, and complex materials, for example, proteins and carbon nanotubes (Lee *et al.*, 2002; Fox *et al.*, 2014; Christian Wagner *et al.*, 2012). The central idea of DFT is to describe the complicated many-body electron interactions through its density, $n(\vec{r})$ (Parr and Yang, 1989). Based on variational principle, the electron charge density serving as the variational parameter

(Hohenberg and Kohn, 1964) is used to seek for the ground state wave functions of the system. The comprehensive discussion of the DFT can be found in the excellent review articles (Parr, 1983; Ziegler, 1991; Geerlings *et al.*, 2003; Jones and Gunnarsson, 1989) and textbooks (Parr and Yang, 1989; Dreizler and Gross, 1990; Martin, 2004). The brief explanation of DFT is following.

First, the electron density is defined as

$$n(\vec{r}) = N \int ... \int \left| \Psi(x_1, x_2, ..., x_N) \right|^2 d\sigma_1 dx_2 ... dx_N \tag{2.7}$$

where $\{x_i\}$ represent both spatial and spin coordinates. $n(\vec{r})$ determines the probability of finding any of the N electrons within the volume $\vec{r}$ but arbitrary spin while the other N-1 electrons have arbitrary positions and spin in the state represented by Ψ. This is a nonnegative simple function of three spatial variables (*x*, *y*, and *z*). It is clear that Eq. 2.7 integrates to the total number of electrons,

$$N = \int n(\vec{r}) d\vec{r} . \tag{2.8}$$

2.3.1 Thomas-Fermi Model

In 1920s Thomas and Fermi proposed the model to describe the electronic energy in term of electronic density (Thomas, 1927; Fermi, 1927). In their model, the kinetic energy of electrons is derived from the quantum statistical theory based on the uniform electron gas, but the electron-nuclei and electron-electron interactions are described classically. Then, the kinetic energy of the electrons is defined as,

$$T[n] = C_F \int n^{5/3}(\vec{r}) d\vec{r} \text{ , with } C_F = \frac{3}{10} (2\pi^2)^{2/3} = 2.871 . \tag{2.9}$$

In this approximation, the kinetic energy of the electrons is expressed in terms of the

electron density $n(\vec{r})$. Therefore, the total energy including the interactions between

electron-nuclei and electron-electron, in terms of $n(\vec{r})$, can be expressed as,

$$E[n] = C_F \int n^{5/3}(\vec{r}) d\vec{r} - Z \int \frac{n(\vec{r})}{r} d\vec{r} + \frac{1}{2} \int\int \frac{n(\vec{r_1})n(\vec{r_2})}{|\vec{r_1} - \vec{r_2}|} d\vec{r_1} d\vec{r_2} \qquad (2.10)$$

The second and third terms are the electron-nuclei and electron-electron interactions,

respectively. The Thomas-Fermi model proposes that the total energy is solely

determined by the electron density.

2.3.2 The Hohenberg and Kohn Theorem

In 1964, Hohenberg and Kohn first derived the fundamentals of the density

functional theory which redefines the electronic Hamiltonian as a function of electron

density $n(\vec{r})$ (Hohenberg and Kohn, 1964). The theorem based on two principles: (i)

Uniqueness theorem, there exists a one-to-one correspondence between *initial*

condition, external potential $V_{ext}(\vec{r})$, and *solution*, electron density $n(\vec{r})$; and (ii)

variational principle, the ground-state total energy can be found by variational of

electron density/wavefunction.

Consider a certain system consisting of electrons moving under the external

potential, $V_{ext}(\vec{r})$, Hohenberg and Kohn proposed that the ground state energy and all

properties of electron wavefunction in the external potential can be determined from

the electron density, $n(\vec{r})$. The ground-state energy of many-electron wavefunction can

be written as (Hohenberg and Kohn, 1964)

$$E\left[n\left(\vec{r}\right)\right] = T\left[n\left(\vec{r}\right)\right] + V_{ne}\left[n\left(\vec{r}\right)\right] + V_{ee}\left[n\left(\vec{r}\right)\right],$$

$$E\left[n\left(\vec{r}\right)\right] = \int V_{ext}\left(\vec{r}\right)n\left(\vec{r}\right)d^3r + F_{HK}\left[n\left(\vec{r}\right)\right], \tag{2.11}$$

where

$$F_{HK}\left[n\left(\vec{r}\right)\right] = T\left[n\left(\vec{r}\right)\right] + V_{ee}\left[n\left(\vec{r}\right)\right]. \tag{2.12}$$

In Eq. 2.11, the $V_{ext}(\vec{r})$ is the external potential generated by the interactions between nuclei and electrons. $F_{HK}\left[n\left(\vec{r}\right)\right]$ is an unknown function, but it is a universal function of the electron density $n(\vec{r})$. It does not depend on the external potential and includes all kinetic energy and electron-electron interaction terms (Parr and Yang, 1989)

The difficulty to determine the ground state energy in the Hohenberg and Kohn theory is an unknown function $F_{HK}\left[n\left(\vec{r}\right)\right]$. In principle, the introduction of $F_{HK}\left[n\left(\vec{r}\right)\right]$ is to reformulate the interacting many-electron system to a non-interacting one such that the complexity of manybody interactions is buried inside $F_{HK}\left[n\left(\vec{r}\right)\right]$. It still to be the major problem to determine the universal function $F_{HK}\left[n\left(\vec{r}\right)\right]$. However, it enables one to understand the roles of these interactions on the ground-state wavefunctions by applying different kinds of approximations to $F_{HK}\left[n\left(\vec{r}\right)\right]$. For sufficiently simple functional of $n(\vec{r})$, determining the ground state energy and density in a given external potential $V_{ext}(\vec{r})$ would be possible if the $F_{HK}\left[n\left(\vec{r}\right)\right]$ is known (by approximation rather than exact) since it requires merely minimization of a functional of the three-dimensional density function.

2.3.3 The Kohn and Sham Equation

In 1965, Kohn and Sham (Kohn and Sham, 1965) published a paper that coined the density-functional theory into real-world practice, a practical electronic structure theory. The main complication of the Thomas-Fermi theory is the description of the kinetic energy. Similar to Hartree-Fock approximation (Hartree, 1928), the problem has been addressed by introducing the idea of non-interacting electrons moving in an effective filed. They proposed that the universal function $F_{HK}\left[n(\vec{r})\right]$ in Equation 2.12 can be defined as a sum of three parts, the kinetic energy of non-interacting electrons (T_s), the Hartree energy (E^{Hatree}), and all the many-body quantum effects are put together into the exchange and correlation energy (E_{xc}). Therefore, the ground-state energy functional which obtained in the previous section can be written as,

$$
\begin{aligned}
E\left[n(\vec{r})\right] &= \int V_{ext}(\vec{r})n(\vec{r})d^3r + F_{HK}\left[n(\vec{r})\right], \\
E\left[n(\vec{r})\right] &= \int V_{ext}(\vec{r})n(\vec{r})d^3r + T_s\left[n(\vec{r})\right] + E^{Hartree}\left[n(\vec{r})\right] + E_{xc}\left[n(\vec{r})\right].
\end{aligned}
\tag{2.13}
$$

Where the third term in Eq. 2.13, $E^{Hartree}\left[n(\vec{r})\right]$ is the electron-electron Coulomb energy (also often referred to as Hartree energy) can be defined as,

$$
E^{Hartree}\left[n(\vec{r})\right] = \frac{e^2}{2}\iint \frac{n(\vec{r})n(\vec{r}^{'})}{\left|\vec{r}-\vec{r}^{'}\right|}d^3r\,d^3r^{'}.
\tag{2.14}
$$

The second term in Eq. 2.13, $T_s\left[n(\vec{r})\right]$ is the kinetic energy of the non-interacting system with the same density. Note that, it is not to be confused with the exact kinetic energy function $\left(T\left[n(\vec{r})\right]\right)$. The difference between $T\left[n(\vec{r})\right]$ and $T_s\left[n(\vec{r})\right]$ is

supposed to be small so that it is inserted into the exchange-correlation energy, the last

term, $E_{xc}\left[n\left(\vec{r}\right)\right]$ in Equation 2.13 (Parr and Yang, 1989).

The above-mentioned effective potential of considered electronic structure

problem is defined as,

$$V_{eff}\left[n\left(\vec{r}\right)\right] = \frac{\delta\left\{\int n\left(\vec{r}\right)V_{ext}\left(\vec{r}\right)d\vec{r} + E^{Hartree}\left[n\left(\vec{r}\right)\right] + E_{xc}\left[n\left(\vec{r}\right)\right]\right\}}{\delta n\left(\vec{r}\right)}$$

$$V_{eff}\left[n\left(\vec{r}\right)\right] = V_{ext}\left(\vec{r}\right) + \int\frac{n\left(\vec{r}'\right)}{\left|\vec{r}-\vec{r}'\right|}d^3r' + v_{xc}\left(\vec{r}\right).$$

(2.15)

Where $v_{xc}\left(\vec{r}\right)$ is the exchange-correlation potential which is defined as,

$$v_{xc}\left(\vec{r}\right) = \frac{\delta E_{xc}\left[n\left(\vec{r}\right)\right]}{\delta n\left(\vec{r}\right)}.$$

(2.16)

Finally, the Kohn-Sham DFT has changed our perspective in the seeking for the

solutions of many-electron system by solving a single-electron problem Schrödinger-

like equation. The ground state solution of an electron in the effective potential $V_{eff}\left(\vec{r}\right)$

is expressed as,

$$\left[-\frac{\hbar^2}{2m}\nabla^2 + V_{eff}\left(\vec{r}\right)\right]\phi_i\left(\vec{r}\right) = \varepsilon_i\phi_i\left(\vec{r}\right).$$

(2.17)

Here $\{\phi_i\}$ are the Kohn-Sham one-electron orbitals and the electron density for this

system is given by (Kohn and Sham, 1965)

$$n\left(\vec{r}\right) = \sum_{i=1}^{N}\left|\phi_i\left(\vec{r}\right)\right|^2,$$

(2.18)

where N is the number of electrons. Finally, the total energy can be determined from

the electron density through

$$E = \sum_{i=1}^{N} \varepsilon_i + \frac{1}{2} \iint \frac{n(\vec{r})n(\vec{r}\,')}{\left| \vec{r} - \vec{r}\,' \right|} + E_{xc}\left[n(\vec{r}) \right] - \int v_{xc}(\vec{r})n(\vec{r})d\vec{r}. \qquad (2.19)$$

Eq. 2.15, 2.17 and 2.18 are the notable Kohn-Sham equation. Note that the $V_{eff}(\vec{r})$ depends on the $n(\vec{r})$ through Eq. 2.18. Therefore, the Kohn-Sham equation must be solved self-consistently.

Initially, a guess of $n(\vec{r})$ is used to construct V_{eff}, which is an important function needed to define the Kohn-Sham equation in Eq. 2.17. The Kohn-Sham equation then can be solved to obtain the wavefunctions ϕ_i. Then the obtained ϕ_i are used to construct an improved $n(\vec{r})$. The improved $n(\vec{r})$ is used to construct new V_{eff} in Eq. 2.17. This sequence of improving solutions is iteratively computed until convergence is reached, i.e., the $n(\vec{r})$ remains unchanged (or the difference between the iterations is smaller than some tolerance). Finally, the total energy is calculated from Eq. 2.19 with the most recent electron density.

The Kohn-Sham equation is considered to be exact since there is no approximation imposed. The exact ground state density and total energy could be obtained if the Kohn-Sham energy functional is known. Unfortunately, the exchange-correlation (xc) functional (E_{xc}) is not known exactly. It includes i) the non-classical aspects of the electron-electron interactions and ii) the difference between the kinetic energy of the real system and the fictitious non-interacting system. Therefore, different levels of approximation are involved in order to approximate E_{xc}.

2.4   The Exchange Correlation Functions

The form of the exchange-correlation energy functional has to be known in order to solve the Kohn-Sham equations in Eq. 2.15 and Eq. 2.17. However, the exact form $E_{xc}\left[n(\vec{r})\right]$ is not known. Since the birth of DFT some sort of approximations for $E_{xc}\left[n(\vec{r})\right]$ have been used. By now there is an almost endless list of approximated functionals with varying levels of complexity. Generally, two popular approximations of $E_{xc}\left[n(\vec{r})\right]$; the local density approximation (LDA) and the generalized gradient approximation (GGA) are usually used. The details of the exchange-correlation functions are described below.

2.4.1 The Local Density Approximation (LDA)

LDA was introduced by Kohn and Sham in 1965 (Kohn and Sham, 1965) and it is the most widely used approximation in crystalline solid materials. It is assumed that the electron density can be treated locally as a uniform electron gas. Within LDA, the $E_{xc}\left[n(\vec{r})\right]$ depends on the value of the electron density at a particular point $\vec{r}$ in the system and the exchange-correlation energy is defined as (Parr and Yang, 1989),

$$E_{xc}^{LDA}\left[n(\vec{r})\right] = \int n(\vec{r})\,\varepsilon_{xc}\left[n(\vec{r})\right]d^3r, \tag{2.20}$$

where $\varepsilon_{xc}\left[n(\vec{r})\right]$ is the exchange-correlation energy per particle of a homogeneous electron gas with the density $n(\vec{r})$. The $\varepsilon_{xc}\left[n(\vec{r})\right]$ can be written as a sum of exchange and correlation energy

$$\varepsilon_{xc}\left[n(\vec{r})\right] = \varepsilon_{x}\left[n(\vec{r})\right] + \varepsilon_{c}\left[n(\vec{r})\right], \tag{2.21}$$

where $\varepsilon_x\left[n(\vec{r})\right]$ and $\varepsilon_c\left[n(\vec{r})\right]$ are the exchange and correlation energy density of a homogeneous electron gas of density $n(\vec{r})$, respectively. The analytical form of the exchange energy $\varepsilon_x\left[n(\vec{r})\right]$ of a homogeneous electron gas was derived by Dirac in 1930 (Dirac, 1930) and written as

$$\varepsilon_x\left[n(\vec{r})\right] = -C_x n(\vec{r})^{1/3}, C_x = \frac{3}{4}\left(\frac{3}{\pi}\right)^{1/3}. \tag{2.22}$$

The correlation energy $\varepsilon_c\left[n(\vec{r})\right]$ is much more complicated and generally obtained by parametrization of many-body systems (Gell-Mann and Brueckner, 1957)) (Ceperley and Alder, 1980). For a homogeneous electron gas with different densities, the correlation energy was calculated by Ceperley and Alder (Ceperley and Alder, 1980) by means of quantum Monte Carlo calculations. Modern LDA functionals tend to be exceedingly similar, differing only in how their correlation contributions have been fitted to the many-body free electron gas data. For example, the Vosko-Wilk-Nusair (VWN) (Vosko *et al.*, 1980), Perdew-Zunger (PZ) (Perdew and Zunger, 1981), and Perdew-Wang (PW) (Perdew and Wang, 1992) functionals are based on common LDA functionals.

In principle, the LDA is supposed to be valid only for slow varying electron density system. Fortunately, the LDA works surprisingly well for broader range of system, especially for metals. A partial explanation for this success of the LDA is systematic error cancellation. Typically, in inhomogeneous systems, LDA underestimates correlation but overestimates exchange, resulting in unexpectedly good values of E_{xc}^{LDA}. This error cancellation is not accidental, but systematic, and caused by

the fact that for any density the LDA satisfies a number of so-called sum rules (Gunnarsson and Lundqvist, 1976; Gunnarsson *et al.*, 1976; Ziegler *et al.*, 1977; Burke *et al.*, 1998).

In general, LDA tends to overestimate cohesive energies by ∼15-20% and underestimates lattice constants by ∼2-3% for metals and insulators. Problem with LDA becomes more severe for weakly bonded systems, such as vdW interactions and H-bonded systems. Long-range vdW interactions are completely omitted in LDA.

2.4.2 Generalized Gradient Approximation (GGA)

Since there are quite a number of limitation in LDA. There are many great efforts to develop approximation method beyond the local uniform densities system. The first attempt was the so-called gradient-expansion approximations (GEA) where gradient of the electron density ($n(\vec{r})$) is included for approximation of the exchange-correlation energy. The gradient corrections of the form $\left|\nabla n(\vec{r})\right|$, $\left|\nabla n(\vec{r})\right|^2$, $\left|\nabla^2 n(\vec{r})\right|$, etc., are systematically imposed to the LDA in order to capture rapidly varying electron densities. In practice, including of the low-order gradient corrections rarely improves on the LDA, and often even worsens it. Higher-order corrections are exceedingly difficult to calculate. To correct the gradient of electron density, instead of using the power-series-like gradient expansions one could introduce more general functions of $n(\vec{r})$ and $\nabla n(\vec{r})$. Therefore, generalized gradient approximation (GGA) was proposed to take into account the variation of electron density around the nuclei. In this

approximation, the exchange-correlation energy $E_{xc}\left[n(\vec{r})\right]$ is written as a function of

the electron densities and their gradients $\nabla n(\vec{r})$, (Kohn, 1999)

$$E_{xc}^{GGA}\left[n(\vec{r})\right] = \int f^{GGA}\left[n(\vec{r}), \nabla n(\vec{r})\right]n(\vec{r})d^3r. \qquad (2.23)$$

The GGA is often called the semi-local functionals due to their dependence on

the $\nabla n(\vec{r})$. For many properties, for example, geometries and ground-state energies of

the molecules and the solid, GGAs give better results than the LDAs. Especially for the

covalent bonds and weakly bonded systems, many GGAs work better than LDAs.

Because of the flexibility in the choice of f^{GGA}, there are many developed GGA

functionals depending on the studied systems.

The functional form of f^{GGA} is taken as a correction to LDA exchange and

correlation. Within the GGA the exchange energy takes the form

$$E_{xc}^{GGA}\left[n(\vec{r})\right] = \int n(\vec{r})\varepsilon_x^{unif}\left(n(\vec{r})\right)F_x^{GGA}(s)d^3r. \qquad (2.24)$$

$F_x^{GGA}(s)$ in the above equation is the exchange enhancement factor and tells how much

exchange energy is enhanced over its LDA value for a given $n(\vec{r})$. The choice of the

$F_x^{GGA}(s)$ makes one GGA differ from another. There are many forms of the $F_x^{GGA}(s)$

to approximate the $E_{xc}^{GGA}\left[n(\vec{r})\right]$. One of very popular GGA exchange functionals

applied in this thesis is the Perdew-Burke-Ernzerhof (PBE) functional which has the

following form (Perdew *et al.*, 1996):

$$F_x^{GGA}(s) = 1 + \kappa - \frac{\kappa}{1 + \mu s^2/\kappa} \qquad (2.25)$$

In PBE, κ and μ are the parameters obtained from physical constraints (non-empirical).

2.4.3 The Hybrid Functionals

The hybrid functionals are the developed functionals beyond the LDA/GGA functionals. In these functionals, the "exact exchange" which calculated from the Hartree-Fock functional is added to some conventional treatment of the DFT exchange and correlation. The philosophy behind the hybrid functionals is simple and rooted in the "adiabatic connection" formula, which is a rigorous *ab initio* formula for the exchange-correlation energy of DFT. There are many forms of the hybrid functionals in DFT such as PBE0 (Adamo and Barone, 1999), B3LYP (Kim and Jordan, 1994; Stephens *et al.*, 1994), and HSE (Heyd *et al.*, 2003).

In this thesis, the Heyd-Scuseria-Ernzerhof (HSE) functionals are used in electronic properties calculations. The HSE retains only short-range (*SR*) Fock exchange and preserves the accuracy of PBE0 while avoiding the cost and pathologies of long-range (*LR*) Fock exchange. The HSE functionals define a 2-dimensional space of DFT functionals, set by the fraction of Fock exchange, *a*, at zero electron separation and length scale, ω^{-1}, on which the short-range Fock exchange is computed as,

$$E_{xc}^{HSE} = aE_x^{HF,SR}(\omega) + (1-a)E_x^{PBE,SR}(\omega) + E_x^{PBE,LR}(\omega) + E_c^{PBE}. \qquad (2.26)$$

a is so-called the mixing parameter and ω is an adjustable parameter controlling the short-range Fock exchange. Generally, the standard values of $a = \dfrac{1}{4}$ and $\omega = 0.2$ (usually referred to as HSE06) have been shown to give good results for most systems.

2.5   Van der Waals Density Functional

The problem for the local and semi-local functional of DFT is that it takes into consideration only the electronic density at point $\sim r$ (and its immediate vicinities). The density and its gradient expansion of variations arise more than 3-4 Å away from the point being evaluated. That is where attractive van der Waals (vdW) interactions arise. In fact, the standard LDA and GGA functionals do not properly account for non-local electronic correlation effects such as vdw forces. These forces are important interactions in many sparse materials (Marom *et al.*, 2010; Graziano *et al.*, 2012). Typically, vdWs are also important for system of the molecule on the metal surfaces (Carrasco *et al.*, 2014; Carrasco *et al.*, 2013; Carrasco *et al.*, 2011), three- and two-dimensional solid (Kaloni *et al.*, 2012; Kaloni *et al.*, 2014; Motta *et al.*, 2015), and the molecular complexes (Kaloni *et al.*, 2016; Tkatchenko *et al.*, 2012). They are widely accepted models examining the impact of vdW interactions on the binding of the weakly interacting system. A general outcome from these investigations is that the inclusion of vdW forces to GGA functionals often results in improved binding energies and adsorption distances that are in better agreement with available experimental data.

In general, vdW-inclusive in DFT methods can be classified into two groups (Grimme *et al.*, 2016): (i) approaches based on semi-empirical corrections typically complemented by a dispersion correction to the Kohn-Sham energy, and (ii) non-local correlation density functionals, which directly modify the Kohn-Sham Hamiltonian.

The first generations of the dispersion correction methods are DFT-D and DFT-D2, the detailed of these methods can be found in the articles of Grimme *et al.* (Grimme, 2004; Grimme, 2006). In DFT-D2 method, the correction term takes the form,

$$E_{disp} = -\frac{1}{2}\sum_{i=1}^{N_{at}}\sum_{j=1}^{N_{at}}\sum_{L}{}' \frac{C_{6ij}}{r_{ij,L}^{6}} f_{d,6}\left(r_{ij,L}\right),$$ (2.27)

where the summations over all atoms N_{at} and all translations of the unit cell $L = (l_1, l_2, l_3)$, the "prime" indicates that $i \neq j$ for $L = 0$, C_{6ij} denotes the dispersion coefficient for the atom pair ij, $r_{ij,L}$ is the distance between atom i located in the reference cell $L = 0$ and atom j in in the cell L, and the term $f\left(r_{ij}\right)$ is a damping function whose role into scale the force field such as to minimize contributions from interactions within typical bonding distances. In Eq. 2.27, the parameters C_{6ij} and R_{0ij} are computed by using the following combination rules:

$$C_{6ij} = \sqrt{C_{ii} + C_{6jj}},$$ (2.28)

$$R_{0ij} = R_{0i} + R_{0j},$$ (2.29)

the values of C_{6ii} and R_{0i} are tabulated for each element and are insensitive to the particular chemical situation. In the origin DFT-D method of Grimme, the Fermi-type damping function is used:

$$f_{d,6}\left(r_{ij}\right) = \frac{s_6}{1 + e^{-d\left(r_{ij}/\left(s_R R_{0ij}\right)-1\right)}},$$ (2.30)

whereby the global scaling parameter s_6 has been optimized for several different DFT functional such as PBE ($s_6 = 0.75$) BLYP ($s_6 = 1.2$) and B3LYP ($s_6 = 1.05$). The parameter S_R usually fixed at 1.0.

The DFT-D3 method of Grimme *et al*. (Grimme *et al.*, 2010) is used in the thesis. In this method, the vdW-energy expression is given as,

$$E_{disp} = -\frac{1}{2}\sum_{i=1}^{N_{at}}\sum_{j=1}^{N_{at}}\sum_{L}{}' \left(f_{d,6}\left(r_{ij,L}\right)\frac{C_{6ij}}{r_{ij,L}^{6}} + f_{d,8}\left(r_{ij,L}\right)\frac{C_{8ij}}{r_{ij,L}^{8}} \right), \tag{2.31}$$

Unlike in the DFT-D2, the dispersion coefficient C_{6ij} is geometry-dependent as they are adjusted on the basis of geometry (coordination number) around atoms i and j. In this method, the damping function takes the form:

$$f_{d,n}\left(r_{ij}\right) = \frac{s_n}{1 + 6\left(r_{ij}/\left(s_{R,n}R_{0ij}\right)\right)^{-\alpha_n}}, \tag{2.32}$$

where $R_{0ij} = \sqrt{\dfrac{c_{8ij}}{c_{6ij}}}$, the parameters α_6, α_8, $s_{R,8}$ are fixed at values of 14., 16., and 1., respectively, and s_6, s_8 and $s_{R,6}$ are adjustable parameters whose values depend on the choice of exchange-correlation functional.

2.6 Bloch's Theorem and Plane Wave Basis Sets

Even with the DFT and a simple exchange-correlation function, the direct calculation of large number of electrons in the electric field from an almost infinite number of ions is still impossible. In a direct calculation of a real system, the wave function has to be calculated for every single electron in the system which is in the order of 10^{23} electrons. In addition, to fully describe each electron wave function, the basis set, if not carefully chosen, could be infinitely large. However, the fact that crystalline has a periodicity of ions can be used to reduce the computational effort based on Bloch's theorem (Ashcroft and Mermin, 1976; Blöchl, 1994). By using this theorem, it is possible to express the wave function of an infinite crystal in terms of the periodic function with the same periodicity, the primitive unit cell.

Bloch's theorem uses the periodicity of a crystal to describe the real space electron wave functions in terms of a periodic function. Bloch's plane wave function can be written as a product of the wave part, $e^{i\vec{k}\cdot\vec{r}}$ and a periodic part, $u_{n\vec{k}}\left(\vec{r}\right)$ (Kittle, 1996),

$$\psi_{n\vec{k}}\left(\vec{r}\right) = e^{i\vec{k}\cdot\vec{r}}u_{n\vec{k}}\left(\vec{r}\right), \tag{2.33}$$

where

$$u_{n\vec{k}}\left(\vec{r}\right) = u_{n\vec{k}}\left(\vec{r}+\vec{R}\right). \tag{2.34}$$

Equation 2.33 and 2.34 are the well-known as Bloch's theorem, where $\vec{r}$ is the position in the crystal, $\vec{R}$ is the lattice translation vector in the crystal, $\vec{k}$ is the wave vector, n is the band index representing different solutions that have the same wave vector $\vec{k}$. Using the Fourier transform of the periodic function to the reciprocal space, the wave function in Equation 2.11 can be written in the sum plane waves form as (Kittle, 1996),

$$\psi_{n\vec{k}}\left(\vec{r}\right) = \sum_{G} u_{n\vec{k}}\left(\vec{G}\right)e^{i\left(\vec{k}+\vec{G}\right)\cdot\vec{r}}, \tag{2.35}$$

where $\vec{G}$ is the reciprocal lattice vectors. This allows the calculations to be done in the reciprocal space. In order to limit the number of plane wave used for the expansion, the plane waves used in the calculations are those with the kinetic energy smaller than the energy cutoff, E_{cutoff}, (Martin, 2004),

$$\frac{\hbar^2}{2m}\left|k+G\right|^2 < E_{cutoff}. \tag{2.36}$$

The value of required energy cutoff depends on the required accuracy of the results and the complication of the wave functions which is mainly related to the elements under study.

2.7   Special k-point in the Brillouin Zone

The Brillouin zone is the Wigner-Seitz cell in the reciprocal lattice, which is defined by the planes that are the perpendicular bisectors of the vectors from the origin to the reciprocal lattice points. The first Brillouin zone is the smallest unit cell in the reciprocal space corresponding to the crystal unit cell in real space (Martin, 2004). In principle, we have to compute the wave functions at every k-point, infinitely many, in the first Brillouin zone. In practice, it is impossible to do calculations with the infinite number of k-points. Since the wavefunctions are quite similar for k-points in the same vicinity, it is possible to sampling a limited number of k-points in the first Brillouin zone as a representative set based on crystal symmetry. There are various k-point sampling methods introduced for different crystal symmetries. In this work, we employed the sampling method introduced by Monkhorst and Pack (Monkhorst and Pack, 1976).

2.8   Pseudopotentials

Electrons in materials can be divided into two types based on their bonding role: core electrons and valence electrons. The core electrons are in the inner shell of each atom where the potentials decrease rapidly. The valence electrons are in the outer shell. The valence-electron wavefunctions are orthogonal to the core-electron wavefunctions. A set of plane-waves (PWs) with a certain value of E_{cutoff}, that is enough to describe the valence region, is not guaranteed to properly describe the core region due to rapid varying wavefunctions. The wavefunctions in the core region have a fast oscillation characteristic (Heine, 1980). However, the physical and chemical properties of materials depend mainly on the interactions of the valence electrons between the atoms.

As a matter of fact, it is reasonable to replace all-electron full-potentials with pseudopotentials that consider only the valence region and provide more computational efficient. In the pseudopotential approach, the core electrons are approximated to be "*frozen*". The properties of the systems are calculated based on an assumption that core electrons are independent of structural modifications and irrelevant in the chemical bonding . In the pseudopotential scheme, the deep core potential part is replaced by a smooth pseudopotential, $V^{PS}(\vec{r})$ as illustrated in Figure 2.1. Removing the core electrons from the calculations should not seriously affect the bonding properties in materials because the core electrons should remain almost inacted under all deformations. The corresponding set of pseudo wavefunctions, $\psi^{PS}(\vec{r})$ and all-electron wavefunctions, $\psi(\vec{r})$ are matched outside a selected core radius, r_c. Inside r_c, $\psi^{PS}(\vec{r})$ does not have the fast oscillation features and low cutoff energy of the plane waves is considered to be enough. As a result, the wave function which is the solution to pseudopotential becomes very smooth in the core area as illustrated in Figure 2.1.
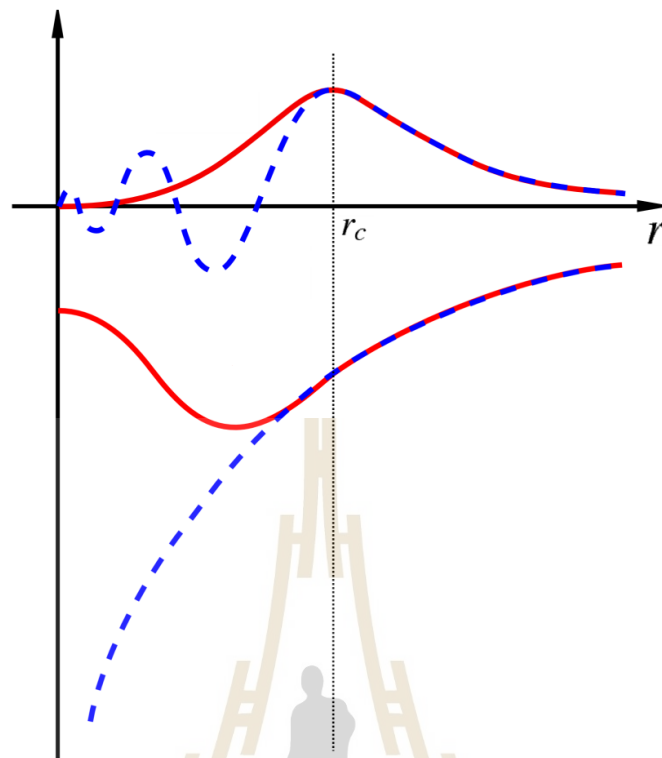
Figure 2.1 Illustrations of the pseudopotential and the pseudo wavefunction. The blue dash lines represent the real electrons wavefunction (top), $\psi(\vec{r})$, and real potential (bottom), $V(\vec{r})$. The red solid lines represent the corresponding pseudo wave functions (top), $\psi^{PS}(\vec{r})$ based on the pseudopotential (bottom), $V^{PS}(\vec{r})$. The cutoff radius, r_c represents a critical radius at which all-electron and pseudo wavefunction/potential are matched.

2.8.1 Norm-conserving Pseudopotentials

Mathematically, the pseudopotential replaces the core potential by fictitious function such that a number of requirements are needed to impose to the pseudopotential. The crucial requirement of the pseudopotential is the norm-conserving conditions. This is to ensure that the integration of both pseudo and all-electron

wavefunctions within the core region be the same (Hamann *et al.*, 1979). The norm-conserving conditions are defined from the following list of conditions (Martin, 2004).

(i). Inside the core, the real and pseudo wavefunctions reproduce the same charge density, this can be defined as,

$$\int_0^{r_c} \psi_{AE}^*(\vec{r})\psi_{AE}(\vec{r})d^3\vec{r} = \int_0^{r_c} \psi_{PS}^*(\vec{r})\psi_{PS}(\vec{r})d^3\vec{r} \,. \tag{2.37}$$

The left-hand and right-hand side of Eq. 2.37 represent charge density derived by the all-electron and pseudo wavefunctions, respectively, are the same inside the core. Whereas the all-electron and pseudo wavefunctions are the same outside the core,

$$\psi_{AE}(\vec{r}) = \psi_{PS}(\vec{r}) \;;\; r > r_c. \tag{2.38}$$

(ii). The eigenvalues should be conserved, i.e.,

$$\varepsilon^{AE} = \varepsilon^{PS} \tag{2.39}$$

(iii) The logarithmic derivatives of all-electron and pseudo wavefunctions and their first-order energy derivatives match at r_c.

The logarithmic derivative for an angular momentum l, can be written as

$$D_l(\varepsilon) = \frac{d}{dr}\ln\psi_l(r;\varepsilon)\Big|_{r_c} = \frac{\psi_l'(r;\varepsilon)}{\psi_l(r;\varepsilon)}, \tag{2.40}$$

where $\psi_l(r;\varepsilon)$ is the solution of the radial Kohn-Sham equation for a fixed potential and fixed energy ε.

The norm-conserving pseudopotentials, V^{PS} can be divided into the local potential, ($V_{loc}^{PS}(r)$) and the non-local potential, ($V_{nonloc}^{PS}(r)$) (Kleinman and Bylander, 1982) as,

$$V^{PS} = V_{loc}^{PS}(r) + V_{nonloc}^{PS}(r) = V_{loc}^{PS}(r) + \sum_l |\beta_l\rangle V_l \langle\beta_l|. \tag{2.41}$$

The non-local part is the deviation from the all-electron potential and is confined inside r_c. The projector $|\beta_l\rangle$ acts on the wavefunctions with angular momentum (l), which is localized within r_c.

2.8.2 Ultrasoft Pseudopotentials

Although pseudopotentials allow the expansion of pseudo wavefunctions using a set of plane waves as a basis, there are still quite a large number of plane waves required to produce accurate wave functions. A small increase in the number of plane waves used in the basis set significantly impact the computational resource. To reduce the number of plane waves needed, an ultrasoft pseudopotentials (USPPs) approach were introduced. The USPPs approach was introduced by Vanderbilt in 1990 (Vanderbilt, 1990), in order to allow the calculations to be performed with the lowest possible cutoff energy for a plane-wave basis set.

The norm-conserving requirements have been relaxed in USPPs, to obtain shallower potentials and smoother wave functions in the core region. Instead of using the plane wave to describe the full valence electron wave function, an only a small portion of the wave function is calculated within the USPPs scheme. This allows one to reduce substantially the planewave cutoff energy in the calculations (Meyer, 2006).

2.8.3 Projector Augmented Waves

The projector augmented waves (PAW) method was proposed by Blöchl (Blöchl, 1994). In this method, a smooth wavefunction (ψ) is created. There exists a linear transformation which relates the all-electron wave function (ψ) to the smooth wavefunction (ψ) by the linear transformation operator, τ through the relationship,

$$|\psi\rangle = \tau |\psi\rangle. \tag{2.42}$$

Utilizing the linear transformation of PAW method, the all-electron wavefunction (ψ) can be written as

$$|\psi\rangle = |\psi\rangle + \sum_m \left(|\psi_m\rangle - |\psi_m\rangle \right) \langle p_m |\psi\rangle, \tag{2.43}$$

where ψ_m is the localized all-electron partial wave for state m, ψ_m is the localized smooth partial wave for state m, and $\langle p_m |$ is the localized projection operator. The linear transformation operator τ can be written as,

$$\tau = 1 + \sum_m \left(|\psi_m\rangle - |\psi_m\rangle \right) \langle p_m |. \tag{2.44}$$

In Eq. 2.44, the linear transformation operator τ can be used to add back the core potential of an all-electron wavefunction to a smoothed wavefunction. Note that Equation 2.22 can be for the core as well as valence states (Martin, 2004).

2.9 Hellmann-Feynman Theorem

The Hellmann-Feynman theorem derives from the relationship between the derivative of the total energy and the derivation of the Hamiltonian. If λ is a parameter in the Hamiltonian, (H), we can write the derivative of energy with respect to λ as

$$\frac{\partial E}{\partial \lambda} = \frac{\partial}{\partial \lambda} \langle \psi |H|\psi\rangle = \left\langle \frac{\partial \psi}{\partial \lambda} \Big| H \Big| \psi \right\rangle + \left\langle \psi \Big| \frac{\partial H}{\partial \lambda} \Big| \psi \right\rangle + \left\langle \psi \Big| H \Big| \frac{\partial \psi}{\partial \lambda} \right\rangle,$$

$$\frac{\partial E}{\partial \lambda} = E \left\langle \frac{\partial \psi}{\partial \lambda} \Big| \psi \right\rangle + \left\langle \psi \Big| \frac{\partial H}{\partial \lambda} \Big| \psi \right\rangle + E \left\langle \psi \Big| \frac{\partial \psi}{\partial \lambda} \right\rangle,$$

$$\frac{\partial E}{\partial \lambda} = E \frac{\partial}{\partial \lambda} \langle \psi | \psi \rangle + \left\langle \psi \left| \frac{\partial H}{\partial \lambda} \right| \psi \right\rangle,$$

$$\frac{\partial E}{\partial \lambda} = \left\langle \psi \left| \frac{\partial H}{\partial \lambda} \right| \psi \right\rangle. \tag{2.45}$$

where $\psi(\lambda)$ is an eigenfunction of H. Equation 2.45 is a well-known Hellmann-Feynman theorem (Hellmann, 1937). It shows that the derivative of the total energy with respect to a parameter λ can be calculated using the derivative of the operator instead. If λ is **R**, the forces are obtained and the Hellmann-Feynman force theorem is written as,

$$F_i = -\frac{\partial E}{\partial R_i} = -\int n(\vec{r}) \frac{\partial V_{ext}(\vec{r})}{\partial R_i} d^3\vec{r} - \frac{\partial E_{II}}{\partial R_i} = -\left\langle \psi \left| \frac{\partial H}{\partial R_i} \right| \psi \right\rangle - \frac{\partial E_{II}}{\partial R_i}, \tag{2.46}$$

where E_{II} is the electrostatic nucleus-nucleus (ion-ion) interactions.

2.10 The Vienna *Ab initio* Simulation Package (VASP)

In this thesis, the calculations were performed by using the Vienna *Ab initio* Simulation Package (VASP) developed by Kresse, Hafner and Furthmüller (Kresse and Furthmüller, 1996a; Kresse and Furthmüller, 1996b; Kresse and Furthmüller, 2012). In VASP, the electron wavefunctions are described by using the plane waves (PWs) basis set. The ultrasoft pseudopotentials (USPPs) (Vanderbilt, 1990) and projector augmented wave (PAW) (Blöchl, 1994) potentials needed for the calculations are included in the package. In this thesis, the pseudopotentials (without PAW) that are sufficient to provide a good description of elastic properties are mainly employed. The k-point samplings are based on the Monkhorst-Pack approach (Monkhorst and Pack,

1976) The main computational part for solving the Kohn-Sham equation self-consistently utilized an iterative matrix-diagonalization scheme such as a conjugate gradient scheme (Teter *et al.*, 1989; Bylander *et al.*, 1990) and block Davidson scheme (Davidson, 1983). The Broyden/Pulay mixing scheme (Pulay, 1980; Johnson, 1988) is an efficiency used for mixing the original and new electronic charge density during the self-consistency calculation loops. The computational scheme used by the VASP codes is illustrated in Figure 2.2. More details can be found in the manual of VASP (Kresse and Furthmüller, 2012) and an article by the developers (Kresse and Hafner, 1994; Kresse and Furthmüller, 1996b).
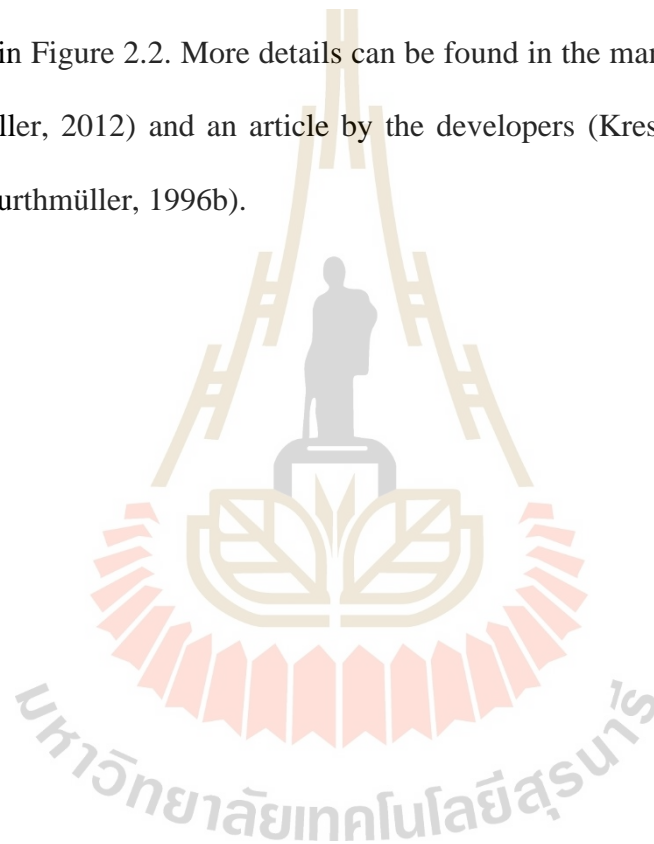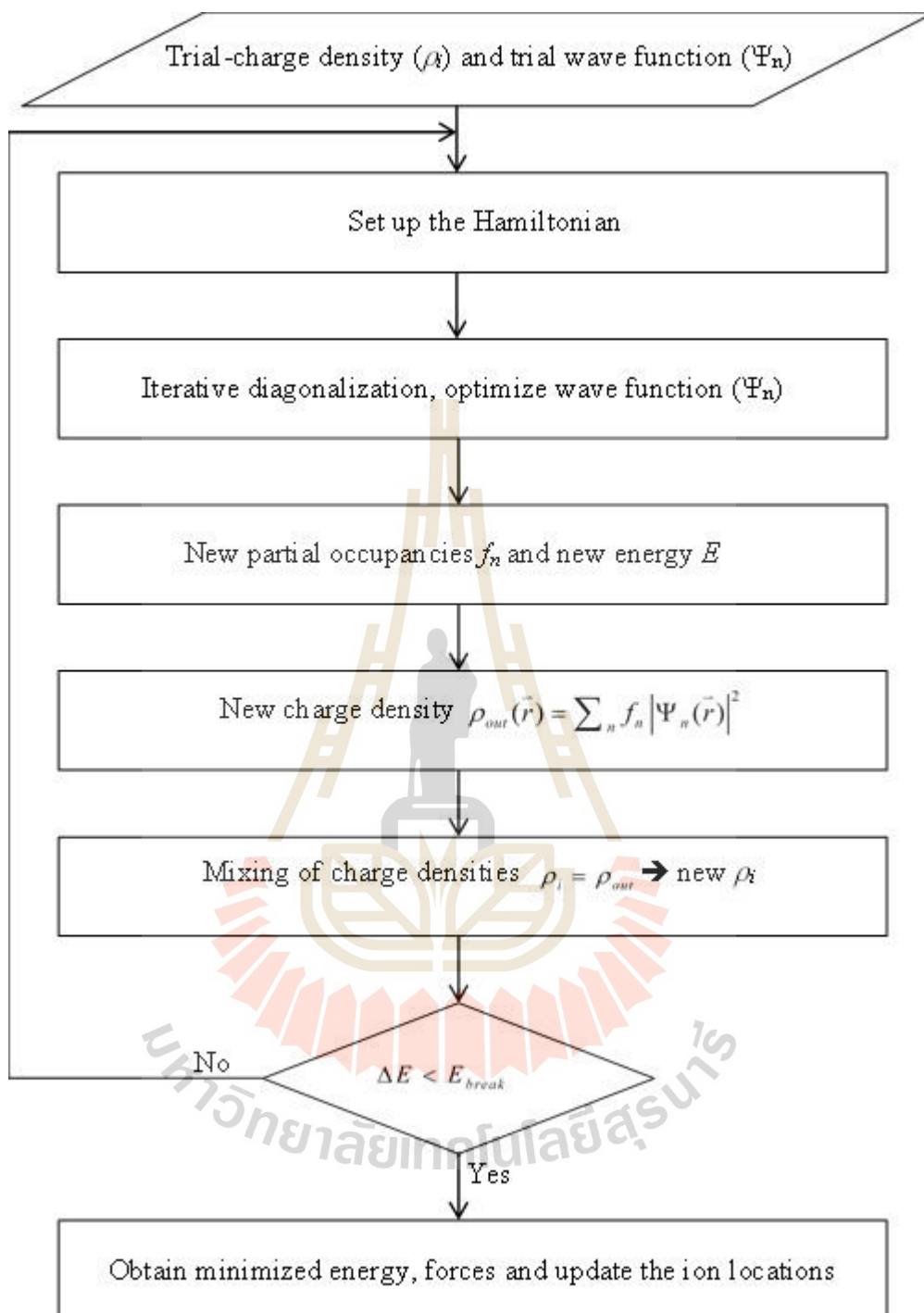
Figure 2.2 The self-consistency scheme used in the VASP codes.

2.11 *GW* Approximation

When considering an electron in the electron gas, the electrons already in the electron gas try to avoid the new electron via the electrons repulsion and the Pauli exclusion principle. In electrons repulsion and the Pauli exclusion principle give rise the exchange and correlation energy. However, the exchange-correlation energy terms in LDA and GGA do not involve any dynamic excitations, so both LDA and GGA are only suitable to study the ground-state properties. In DFT, one focuses on the mean-field average of the exchange-correlation energy resulting from the interactions as it enters the total energy of the system. In this thesis, one part of the electronic properties of the studied materials is calculated by using the *GW* approximation. In this section, the *GW* approximation is briefly described.

According to the limitation of DFT in excited state calculation, another approach, so-called many-body perturbation theory is needed to use in the excited state calculation. In this approach, the central quantity is $G\left(t_2, r_2; t_1, r_1\right)$, the electron propagator. It gives the probability amplitude to create an electron at the position r_1 at the time t_1 from the ground state, subsequently travelling to another position r_2 at a time t_2 where it is annihilated. Its Fourier transform from time to energy describes a spectral function with peaks at the quasiparticle energies. These are the excitation energies for an electron which we conventionally call "the band structure". The above describes the motion of an added electron to the first available empty state, as would be measured in an inverse photoemission. On the other words, the above describes the motion of a hole in the occupied bands. The effects from the interaction of electron and hole with another electrons as it propagates are embodied in the so-called self-energy

operator, which describes all interactions beyond the Hartree potential. In 1965, Hedin (Hedin, 1965) proposed the method to calculate the self-energy in terms of the screened Coulomb interaction W. In his GW approximation, the product of G and W is the electron self-energy, which usually denoted by Σ. The Green's function or propagator can be written in terms of a quasiparticle wave function. The quasiparticle excitation energies and wavefunction can be obtained from

$$\left[-\frac{\nabla^2}{2} + V_{ext}\left(\vec{r}\right) + V_H\left(\vec{r}\right) \right]\phi_i\left(\vec{r}\right) + \int d\vec{r} \, \Sigma\left(\vec{r}, \vec{r}, \varepsilon_i^{GW}\right)\phi_i\left(\vec{r}\right) = \varepsilon_i^{GW}\phi_i\left(\vec{r}\right). \quad (2.47)$$

The Eq. 2.47 closely resembles the Kohn-Sham equation in DFT but this is deceiving. At first sight, it appears that the exchange-correlation potential is replaced by a non-local and energy-dependent self-energy operator term. However, the meaning of both equations is different. The Kohn-Sham equation describes the energies of fictitious non-interacting particles in the effective potential which happen to have the same density as the real interacting electrons in the external potential and it is used only as an intermediate step to obtain the ground-state total energy. While the Eq. 2.47 describes the actual excitation energies that would be probed by one-particle spectroscopies, such as photoemission and inverse photo-emission.

Resemblance of the Eq. 2.47 and the Kohn-Sham equation is exploited in practice to solve the Eq. 2.47. It is usually solved by perturbation theory starting from the Kohn-Sham equation. In that sense, the electron self-energy provides a shift of the Kohn-Sham one-electron eigenvalues as well as a lifetime through its imaginary part. Assuming the wavefunctions of the Eq. 2.47 are the same as those in Kohn-Sham equation in Eq. 2.17, the eigenenergy of Eq. 2.47 is

$$\varepsilon_i^{GW} = \varepsilon_i^{LDA} + \left\langle \phi_i^{LDA} \left[\left[\Sigma\left(\vec{r}, \vec{r}, \varepsilon_i^{GW}\right) - V_{xc}^{LDA}\left(\vec{r}\right) \right]\right] \phi_i^{LDA} \right\rangle \quad (2.48)$$

Expanding the Σ around ε_i^{LDA}, we have

$$\varepsilon_i^{GW} = \varepsilon_i^{LDA} + Z_i \left\langle \phi_i^{LDA} \left[\Sigma\left(\vec{r},\vec{r}',\varepsilon_i^{LDA}\right) - V_{xc}^{LDA}\left(\vec{r}\right) \right] \phi_i^{LDA} \right\rangle \quad (2.49)$$

where $Z_i = \left(1 - \left\langle \phi_i^{LDA} \left[\dfrac{\partial}{\partial \varepsilon} \Sigma\left(\vec{r},\vec{r}',\varepsilon\right)\Big|_{\varepsilon=\varepsilon_i^{LDA}} \right] \phi_i^{LDA} \right\rangle \right)^{-1}$ is the renormalization factor.

However, this means that the result still depends on the starting point of LDA, as we will be discussed next section. The problem is addressed by the so-called quasiparticle self-consistent *GW* method.

2.12 Quasiparticle Self-consistent (QS) *GW* Approximation

From Eq. 2.48, we can see that the accuracy of the *GW* calculations depends on the starting point. The so-called quasiparticle self-consistent *GW* (QS*GW*) formalism was proposed by Van Schilfgaarde *et al.* (van Schilfgaarde *et al.*, 2006) to rectify this problem. The starting point for *GW* approach is defined in terms of the zero-th order Hamiltonian, which is usually taken to be the DFT Kohn-Sham equation

$$H^0 \phi_i\left(\vec{r}\right) \equiv \left(-\frac{\nabla^2}{2} + V_{eff} \right) \phi_i\left(\vec{r}\right) \equiv \left(-\frac{\nabla^2}{2} + V_{ext} + V_H + V_{xc} \right) \phi_i\left(\vec{r}\right) = \varepsilon_i \phi_i\left(\vec{r}\right). \quad (2.50)$$

It provides the corresponding Green's function G^0

$$G^0 = \frac{1}{\omega - H_0 \pm i\delta} \quad (2.51)$$

where, with small δ, the $\pm$ sign depends on whether $\omega > \mu$, or $\omega < \mu$ with μ is the chemical potential or Fermi level. Once G^0 is determined, we can then calculate the electron self-energy and the following "Hamiltonian"

$$H\left(\omega\right) = -\frac{\nabla^2}{2} + V_{ext} + V_H + \Sigma\left[G^0\left(\omega\right)\right]. \quad (2.52)$$

This is the operator entering the quasiparticle equation Eq. 2.47. Because it is energy-dependent and contains the complex $\Sigma(\omega)$, it is actually a non-hermitian operator. This is solved in perturbation theory and will thus be the more accurate, the closer the H^0 is to H. Next, Van Schilfgaarde and Kotani (van Schilfgaarde *et al.*, 2006) came up with a prescription to obtain a new H^0 from the self-energy Σ. The new H^0 is defined in terms of non-local and energy independent exchange-correlation potential V_{xc} in the following way

$$V_{xc}^{QSGW} = \frac{1}{2}\sum_{ij}|\phi_i\rangle\langle\phi_i|\left\{\mathrm{Re}\left[\Sigma(\varepsilon_i)\right]+\mathrm{Re}\left[\Sigma(\varepsilon_j)\right]\right\}|\phi_j\rangle\langle\phi_j| \qquad (2.53)$$

where Re signifies the Hermitian part; ϕ_i and ε_i are eigenfunctions and eigenvalues in Eq. 2.50. It allows the eigenstates of the original H^0 to become intermixed, so that the final solutions may be farther away from the DFT starting point of H^0. The new H^0 then defines a new G^0, which gives a new Σ, a new V_{xc}^{QSGW} and the set of equations can be iterated to convergence. This ultimately makes the method independent of the starting point and the eigenvalues of the H^0 converge to those of the quasiparticle equation. Of course, the actual energy-dependent self-energy $\Sigma(\omega)$ still contains additional information on the lifetime and possibly even a more complex spectral shape than a simple broadened quasiparticle peak. It may contain for example satellite structures. In this way, QS*GW* provides better accuracy than one-shot *GW* and should not be dependent on the starting point.

2.13   Full-Potential Linear Muffin-Tin Orbital (FP-LMTO) Method

The Muffin-Tin Orbital (MTO) method is one method used to solve the single-particle Schrödinger equation with periodic boundary condition. In full-potential linear muffin tin orbital (FP-LMTO) method, the unit cell is divided into atom centered muffin tin spheres and a interstitial region outside these spheres. Inside the muffin tin spheres, the potentials can be solved numerically by means of expansions in spherical harmonics (Methfessel *et al.*, 1989). In the interstitial region, the potential is calculated by using numerical integration which results in the matrix elements (Methfessel *et al.*, 2000),

$$V_{ij}^{(IR)} = \int_{IR} H_i^*(\vec{r})V(\vec{r})H_j(\vec{r})d\vec{r} \qquad (2.54)$$

where $V_{ij}^{(IR)}$ is the matrix element potential in the interstitial region, the functions $H_i(\vec{r})$ (or $H_j(\vec{r})$) is the envelope functions, which are augmented inside the muffin tin sphere to obtain the final basis function, $V(\vec{r})$ is the interstitial potential and IR denoted the interstitial region. The results also depend on how the suitable interstitial region is chosen. The general way of obtaining the interstitial region is presented as follow. The basis functions and the interstitial potential are smoothly extended through the atomic sphere in some manner. Then these smooth functions are replaced into Eq. 2.54 to integrate for the potential of the interstitial region. Finally, the unwanted contributions inside the spheres are subtracted in conjunction with the augmentation step. In FP-LMTO, the smooth extension must be built for the sphere on which the function is the centered by matching an analytical expression (i.e. a polynomial) at the sphere radius (Methfessel *et al.*, 2000). Alternatively, Hankel functions can be used to represent interstitial quantities. These functions make basis function quite similar to the real basis

functions. Moreover, a smoothed Hankel functions that are bent more than normal Hankel functions near the muffin tin sphere, is introduced. This smoothed Hankel functions lead to the smaller basis functions. A different approach (to the interstitial potential matrix elements) is to re-expand the product of any two envelopes as a sum of an auxiliary atom-centered basis function. The matrix element in Eq. 2.54 then reduces to a linear combination of integrals of the auxiliary atom centered basis function times the interstitial potential. In this way the three-center integrals in Eq. 2.54 can be reduced to a sum of two-center integrals (Methfessel *et al.*, 1989). The expansion can be obtained approximately by using Gauss's theorem to fit on the surfaces of the muffin-tin spheres (Methfessel *et al.*, 1989; Methfessel *et al.*, 2000). For further details, see Ref. (Methfessel *et al.*, 2000).
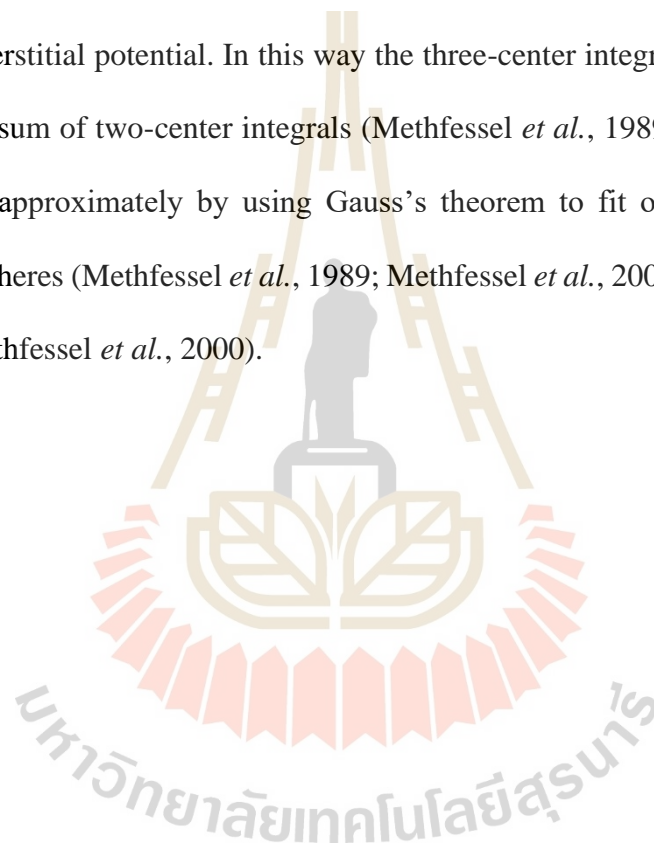
CHAPTER III

CRYSTAL STRUCTURE AND PHASE TRANSITION OF HALIDE PEROVSKITE MATERIALS AND RELATED PEROVSKITE MATERIALS

3.1   Crystal Structure and Phase Transitions

Naturally, the crystal structures of perovskite materials are temperature dependent (Ksepko and Ratuszna, 2018; Yoshiasa *et al.*, 2016; Cheng *et al.*, 2003; Ravel *et al.*, 1998). For example, the structures of a well-known oxide perovskite such as $BaTiO_3$ are changed as changing of the temperature. Above 120 °C (Curie temperature, T_c), the cubic structure could be observed (Han *et al.*, 2013). Below the T_c (around the room temperature), $BaTiO_3$ exhibits the tetragonal phase with an accompanying movement of the Ti atom inside the O_6 octahedra which may be considered to be responsible for the dipole moment and hence for the spontaneous polarization of these type of materials. When the temperature cooled to ~0°C, the tetragonal is transformed into an orthorhombic structure (Ravel *et al.*, 1998). Additionally, the crystal structures of the ABO$_3$ perovskites can depend on the cations atom. For example, $CaTiO_3$ exhibits the orthorhombic *Pbnm* structure, while the $MgTiO_3$ has the trigonal $R\bar{3}$ structure and the $SrTiO_3$ exhibits the cubic $Pm\bar{3}m$ (Culbertson *et al.*, 2020).

The effects of cation species on the structural and elastic properties of ABO_3 perovskites (A = Be, Mg, Ca, Sr, and Ba ; B =Ti, Zr, and Hf) were also studied (Pandech *et al.*, 2015). The lattice constants of the studied materials were found monotonically increased with the cations size. Additionally, the C_{11} elastic constant (represents a longitudinal compression or stifness) was found to increase with the A-site cation until it reaches maximum when the atomic size of the cations are compable. The details of the elastic constants calculations could be found in Appendix.

For the so-called halide perovskites, the B-site occupied by Pb and Sn and form the Pb- and Sn-based halide perovskite materials. The crystal structures of Pb- and Sn-based halide perovskite materials are also temperature-dependent. Their exact structures are still unclear because of the complexity introduced by the MA^+ cation group. Experimentally, many research groups have attempted to identify the structures of the materials using neutron powder diffraction (NPD) and also synchrotron X-ray powder diffraction (Weller *et al.*, 2015; Whitfield *et al.*, 2016). At high temperature the α-structure is cubic (with space group $Pm\bar{3}m$ if the molecular orientations are ignored or MA is replaced by a symmetric Cs ion), as shown in Figure 3.1 (a) and (b). However, the Pb or Sn ferroelectric displacement in its octahedron or the MA in-phase orientation can lead to a non-centrosymmetric tetragonal *P4mm* space group (Stoumpos *et al.*, 2013). The β-phase occurs by alternatingly tilting the octahedra clock and counterclockwise about a single axis, thereby doubling the unit cell to a $\sqrt{2} \times \sqrt{2} \times 1$ cell and making the system tetragonal. In CsSnI$_3$ this leads to the *P4/mbm* group because the tilts are in phase in the c-direction. However, with the additional ferroelectric symmetry breaking of the MA ions, the space group becomes *I4cm*. Others however assigned the *I4/mcm* spacegroup (Weller *et al.*, 2015; Stoumpos *et al.*, 2013)

to this phase in MAPbI$_3$, as shown in Figure 3.1(c) and (d). This phase occurs in SrTiO$_3$ where it also exhibits rotation of the octahedra about the z-axis but which alternates between a clock and counterclockwise along with c-axis thereby doubling the cell again to $\sqrt{2} \times \sqrt{2} \times 2$. On the other hand, the I4/mcm phase which does maintain an inversion symmetry could also result from alternating the MA dipole orientations (Quarti *et al.*, 2014). The transition temperature to this phase depends on the material and occurs at ~180 K in MAPbI$_3$ (Weller *et al.*, 2015), and 200 K in MASnI$_3$ (Stoumpos *et al.*, 2013). Finally, a second transition occurs at a lower temperature to an orthorhombic γ-phase in which octahedral tilts occur about two orthogonal axes and the cell is doubled in the c-direction, as shown in Figure 3.1(e) and (f). The full space group determination in this phase has not been achieved for the different organic ions but is *Pnma* in case of the symmetric A ion and is thus assumed to be derived from this phase (Weller *et al.*, 2015). In MAPbI$_3$, this transition occurs between 100-150K (Weller *et al.*, 2015) while for the Sn case it occurs closer to 100K (Stoumpos *et al.*, 2013). In the low-temperature structure, the BX_6 octahedra are strongly deformed and restrict the rotational motion of MA$^+$ cations (Weller *et al.*, 2015). In this case, the organic cations are fully ordered and pinned and can rotate only along the C-N axis (Weller *et al.*, 2015; Whitfield *et al.*, 2016). When the temperature increases, tetragonal and cubic structures appear. In the high-temperature structures, the organic cations become free to rotate inside the dodecahedral cages and organic cations are disordered (Weller *et al.*, 2015; Whitfield *et al.*, 2016). Nuclear magnetic resonance (NMR) measurements (Knop *et al.*, 1990) have shown that the exact location of the MA-cations cannot be determined in the cubic phase, the reorientation time of the MA-cations is in the order of picoseconds.

Therefore, the presence of organic molecules and their mobility is a challenge in the study of these types of materials.
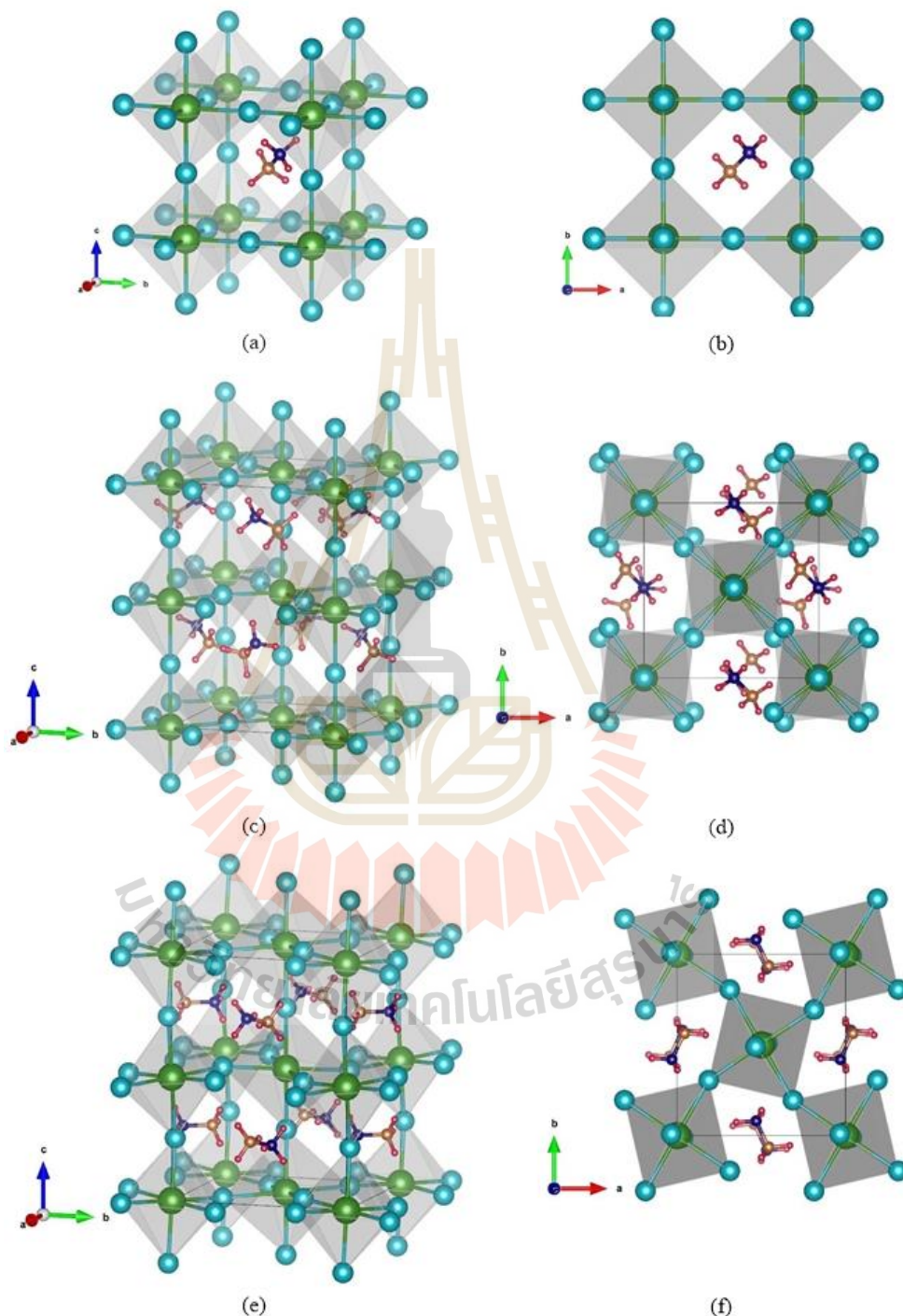
Figure 3.1 The crystal structure of (a-b) high-temperature α-phase, (c-d) intermediate temperature β-phase, and (e-f) low-temperature γ-phase of the MAPbI$_3$. Left panel represents an arbitrary view and right panel represents the top view.

Table 3.1 Summary of phases as the temperature change of studied materials observed in experiments.

Materials/Phase	Temperature (K)	Crystal system	Space group	Lattice (Å)	Volume (Å^3)
$CH_3NH_3PbI_3$					
α[a]	>327.4	cubic	*Pm3m*	$a = 6.328$	253.5
β[a]	162.2-327.4	tetragonal	*I 4/mcm*	$a = 8.855$ $c = 12.659$	992.6
γ[a]	<162.2	orthorhombic	*P na2_1*	$a = 8.861$ $b = 8.581$ $c = 12.620$	959.5
α[b]	400	tetragonal	*P4mm*	$a = 6.3115$ $c = 6.3161$	251.60
β[b]	293	tetragonal	*I4cm*	$a = 8.849$ $c = 12.642$	990.0
$CH_3NH_3PbBr_3$					
α[a]	>236.9	cubic	*Pm3m*	$a = 5.901$	206.3
β[a]	155.1-236.9	tetragonal	*I 4/mcm*	$a = 8.322$ $c = 11.832$	819.4
γ[a]	149.5-155.1	tetragonal	*P 4/mmm*	$a = 5.894$ $c = 5.861$	
δ	<149.5	orthorhombic	*P na2_1*	$a = 7.979$ $b = 8.580$ $c = 11.849$	811.1
$CH_3NH_3PbCl_3$					
α[a]	>178.8	cubic	*Pm3m*	$a = 5.675$	182.8
β[a]	172.9-178.8	tetragonal	*P 4/mmm*	$a = 5.656$ $c = 5.630$	180.1
γ[a]	<172.9	orthorhombic	*P 222_1*	$a = 5.673$ $b = 5.628$ $c = 11.182$	357.0
$CH_3NH_3SnI_3$					
α[b]	293	tetragonal	*P 4mm*	$a = 6.2302$ $c = 6.2316$	241.88
β[b]	200	tetragonal	*I4cm*	$a = 8.7577$ $c = 12.429$	953.2
γ[b]					
$CH_3NH_3SnBr_3$					
α[c]	Room tempt.	cubic	*Pm3m*	$a = 5.89$	
β					
γ					
$CH_3NH_3SnCl_3$					
α[c]	Room tempt.	monoclinic		$a = 5.69$ $b = 8.23$ $c = 7.94$	
β					
γ					
$CH_3NH_3GeI_3$					
α[d]	Room tempt	trigonal	*R3m*	$a = 8.5534$ $b = 8.5534$ $c = 11.162$	
β					
γ					

[a]Experimental study by Poglitsch and Weber (Poglitsch and Weber, 1987)

[b]Experimental study by Stoumpos *et al.* (Stoumpos *et al.*, 2013)

[c]Experimental and theoretical study by Chiarella *et al.* (Chiarella *et al.*, 2008)

[d]Experimental study by Stoumpos *et al.* (Stoumpos *et al.*, 2015)

3.2   Formability of Perovskite Structure

Although, there are many different types of perovskite materials with ABX_3 chemical formula, the formability of the perovskites based on various requirements (i) charge neutrality between the cations and anions, i.e. $N(A) + N(B) = 3N(X)$, where N represents the valence of the A, B, and X ion respectively. (ii) the stability of BX_6 octahedra, which can be predicted by the octahedral factor, μ (Li *et al.*, 2008). (iii) the ionic radii of A, B, and X which needed to meet the requirements for the Goldschmit tolerance factor, t (Goldschmidt, 1926).

The two important factors, μ and t are based on the ionic radii of A, B, and X ions. The octahedral factor, μ which is the ratio of ionic radii of B-site (r_B) and the X-site (r_X) as defined below (Li *et al.*, 2008)

$$\mu = \frac{r_B}{r_X} \tag{3.1}$$

It can be used to assess whether the B-site cation can fit within the BX_6-octahedra hole, which can be estimated the stability of the BX_6-octahedra framework. The radius of an octahedral hole (r_{hole}) formed within the six-closed pack rigid spheres of r_X is $r_{hole} = 0.414\, r_X$. Based on the Pauling's first rule (the radius ratio rule) (Pauling, 1929), the B-site cation with the μ smaller than 0.414 will not be in contact with six X-site anions, which results in the instability of BX_6-octahedra framework leading to a lower coordination number. For the μ slightly greater than 0.414, the octahedral geometry is more stable since the B-site cation is still in contact with six X-site anions. However, the μ rises and reaches to 0.592, a 7-coordinated capped octahedron will be more favourable. Therefore, to stabilize the BX6-octahedral, it requires that $0.414 \leq \mu \leq 0.592$ (Li *et al.*, 2008).

The Goldschmit tolerance factor, t (Goldschmidt, 1926) based on the ionic radii of A, B, and X ions, is used to predict the mismatches in the size of the A, B, and X ions are tolerated to form perovskite structure. It can be defined as

$$t = \frac{(r_A + r_X)}{\sqrt{2}(r_B + r_X)} \qquad (3.2)$$

where r_A, r_B, and r_X are the ionic radii of the respective involved A, B, and X ions. Based on the ionic size restrictions for the involved cations and anions, stability and formability range for the ABX3-perovskite structures can be empirically derived for the tolerance factor in the range of $0.8 \leq t \leq 1.0$ (Goldschmidt, 1926). For a tolerance factor is $0.9 \leq t \leq 1.0$, the perovskites with the cubic structure are formed predominantly. If $0.8 \leq t \leq 0.9$, the perovskite structures would be distorted within the orthorhombic, tetragonal, and orthorhombic structures. In the lower-range, $t < 0.8$, indicates that the A-site cation is too small for the formation of perovskite structure, alternative structures such as the ilmenite-type $FeTiO_3$ are formed instead. In the upper-range, $t > 1.0$, indicates that the A-site cation is too large to form a three-dimensional perovskite, the hexagonal structures are introduced instead comprising the layers of face-sharing octahedral (Travis *et al.*, 2016; Kieslich *et al.*, 2014).

In halide perovskites, the B-site cation is usually occupied by Pb or Sn atom. Therefore, to achieve a more stable perovskite structure the tolerance factor should be closed to 1.0, thus an extremely large A-site cation is needed for given B-site and X-site ions. In cases Pb- and Sn-based halide perovskite, Cs is considered as large as A-site cation, it is almost the largest group I-element in the periodic table. However, it is still not large enough to hole the stable cubic or tetragonal structure in a wide range of temperatures. Therefore, the A-site must be replaced by a slightly larger monovalent

molecule than that Cs atom, such as $CH_3NH_3^+$ (MA^+) or $CH(NH_2)_2^+$ (FA^+) to stabilize the perovskite structure. This can explain the better photovoltaic performance of $CH_3NH_3PbI_3$ with respect to $CsPbI_3$. For the MA lead halide systems, a cubic structure (see Figure 3.1 a-b) is expected when the t lies between 0.89 and 1.0. Generally, small t could lead to lower-symmetry tetragonal (Figure 3.1 c-d) or orthorhombic (Figure 3.1 e-f) structures., whereas larger t ($t > 1$) could destabilize the tree-dimensional (3D) B-X network, leading to a two- dimensional (2D) layer structure. Importantly, by increasing the temperature it is possible to increase the effective size of the ions, thus changing the effective tolerance factor. This makes it possible to activate transformations thermally from lower to higher symmetry crystals, as shown in Table 3.1.

In cases of organic-inorganic halide perovskites, such as $CH_3NH_3PbI_3$, the challenge in determining tolerance factor lies in estimating the ionic radii of the molecular cation. In particular, assuming free rotational freedom around the molecule center of mass, a rigid sphere model is applicable to the organic cation and leads to a consistent set of effective ionic radii as shown in Table 3.2.

By using the effective ionic radii as shown in Table 3.2, we estimate the tolerance factor, t and the octahedral factor, μ of studied materials and tabulated in Table 3.3. For the cases of Pb- and Sn-based halide perovskites, the calculated t factor lies in 0.9 to 1.0 range and the calculated μ factor lies in 0.54 to 0.66 range respectively, confirming the stability of the perovskite structure. Whereas the calculated t factor of Ge-based halide perovskites is slightly larger than 1, indicating that the crystal structure of $CH_3NH_3GeI_3$ is more distorted and cannot stable in cubic symmetry, instead it

observed in trigonal (with R3m space group) in the room temperature (Stoumpos *et al.*, 2015), as summarized in Table 3.1.

Table 3.2 Effective ionic radii of the organic molecular cation (A-site) and Shannon ionic radii of inorganic cations (B-site) as well as effective ionic radii of anions (X-site) (Shannon, 1976; Kieslich *et al.*, 2014).

A-site cations	Effective radius (pm)	B-site cations	Effective radius (pm)	X-site anions	Effective radius (pm)
		Pb^{2+}	119	I^-	220
$CH_3NH_3^+$	217	Sn^{2+}	110	Br^-	196
		Ge^{2+}	73	Cl^-	187

Table 3.3 Calculated tolerance factor, t and octahedral factor, μ of studied materials. MA cation refers to $CH_3NH_3^+$.

Materials	Tolerance factor (t)	Octahedral factor (μ)
MAPbI3	0.91	0.541
MAPbBr3	0.93	0.607
MAPbCl3	0.94	0.657
MASnI3	0.94	0.500
MASnBr3	0.95	0.561
MASnCl3	0.97	0.608
MAGeI3	1.05	0.332
MAGeBr3	1.09	0.372
MAGeCl3	1.11	0.403

3.3   Calculated Lattice Parameters

3.3.1 Structural Optimization

In the structural optimization, the total energies as a function of unit cell volume were calculated as shown in Figure 3.2. The equilibrium volume (V_0) and the bulk modulus (B_0) and its pressure derivative ($B_0{}'$) can be obtained by fitting the calculated results to the Birch-Murnaghan's equation of state (Birch, 1947; Murnaghan, 1944), which is labeled in Eq. 3.3. The details of structural optimization and also the elastic constants calculations which represented by the case of cubic $SrTiO_3$ can be found in the work of Pandech *et al*. (Pandech *et al.*, 2016) as presented the Appendix. The elastic constants can provide us information for prediction of the polarization and polarizability of these materials.
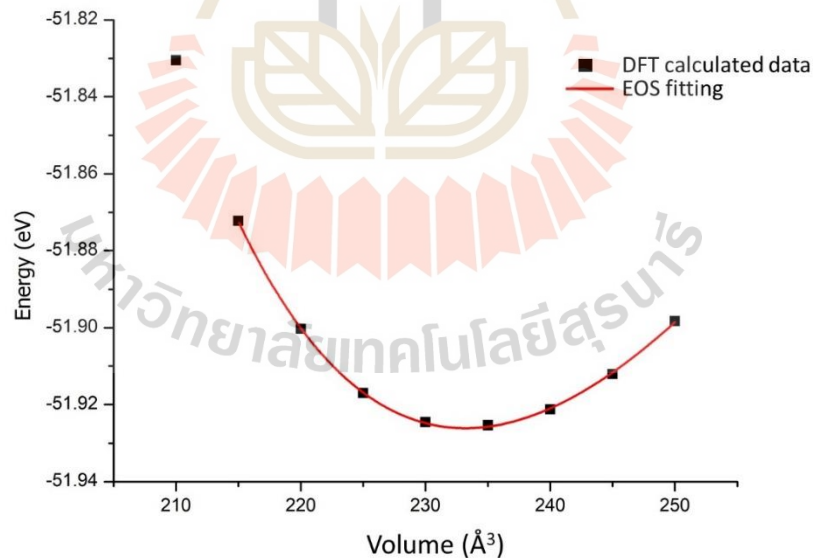
Figure 3.2 Calculated energy of cubic perovskites ABX_3. as a function of unit cell volume (V) obtained from PBE calculation. The equilibrium volume (V_0) and the bulk modulus (B_0) and its pressure derivative ($B_0{}'$) can be obtained by fitting the calculated results to the equation of state.

$$E(V) = E_0 + \frac{9V_0B_0}{16}\left\{\left[\left(\frac{V_0}{V}\right)^{2/3}-1\right]^3 B_0^{'} + \left[\left(\frac{V_0}{V}\right)^{2/3}-1\right]^2\left[6-4\left(\frac{V_0}{V}\right)^{2/3}\right]\right\} \quad (3.3)$$

In cases of organic-inorganic halide perovskite materials, such as $CH_3HN_3PbI_3$, the complexity of the crystal structure was introduced by the present of the freely rotating organic molecule inside the structure. There are several theoretical studies suggested that the van der Waals interaction is significantly important in the structural optimization and also consequently in electronic properties calculations (Motta *et al.*, 2015; Li and Rinke, 2016; Bechtel *et al.*, 2016). In this thesis, the vdW interaction within zero damping DFT-D3 method of Grimme (Grimme, 2004) is considered for collecting the hydrogen bonding between the organic molecules and the halide anions.

The calculated lattice parameters of studied halide perovskite materials with PBE functional are shown in Table 3.4 - Table 3.6, compared with other available calculations and experiments form the literatures. It can be seen that our calculated values are in good agreement with the previous studies. Although in comparison with the experimental values, the lattice constants calculated with PBE functional are overestimated. These behaviours are commonly observed in the calculations of other materials as well. However, the disagreement between the calculated lattice constants and experimental values is less than 2% when the vdW interaction is considered in structural optimization. But, if one does not include the vdW interaction, the disagreements will become larger than 5%, that is the crystal structures are not properly described. The calculated lattice constants without including the vdW interaction are also listed in the parenthesis in Table 3.4 - Table 3.6.

Table 3.4 Calculated lattice constants (in Å) of MAPbX_3 halide perovskite materials in different phases compared to other theoretical and experimental results. The numbers in parenthesis are obtained without vdW interactions.

Materials	Symmetry	Lattice constants (A°)		
		Present-PBE	Another cal.	Expt.(Poglitsch and Weber, 1987)
CH₃NH₃PbI₃	Cubic [$Pm\bar{3}m$]	a = 6.34 (6.48*)	6.22(Yuan *et al.*, 2015)	a = 6.33
	Tetragonal [$I4/mcm$]			a = 8.86 c =12.66
	Orthorhombic [$Pnma$]	a = 8.59 b = 9.24 c = 12.55	a = 8.56(Lee *et al.*, 2015) b = 8.84(Lee *et al.*, 2015) c = 12.59(Lee *et al.*, 2015)	a = 8.58 b = 8.86 c = 12.62
CH₃NH₃PbBr₃	Cubic [$Pm\bar{3}m$]	a = 5.96 (6.08*)	6.03(Yuan *et al.*, 2015)	a = 5.90
	Tetragonal [$I4/mcm$]			a = 8.32 c = 11.83
	Orthorhombic [$Pnma$]	a = 7.89 b = 8.95 c = 12.09		a = 7.98 b = 8.58 c = 11.85
CH₃NH₃PbCl₃	Cubic [$Pm\bar{3}m$]	a = 5.71 (5.83*)	5.99(Yuan *et al.*, 2015)	a = 5.67
	Tetragonal [$I4/mcm$]			
	Orthorhombic [$Pnma$]	a =7.22 b = 8.58 c = 11.48		a =5.67 b = 5.63 c = 11.18

Table 3.5 Calculated lattice constants (in Å) of MASnX_3 halide perovskite materials in different phases compared to other theoretical and experimental results. The numbers in parenthesis are obtained without vdW interactions.

Materials	Symmetry	Present-PBE	Lattice constants (A°) Another cal.	Expt.
CH₃NH₃SnI3	Cubic [$Pm\bar{3}m$]	a = 6.25 (6.42*)	6.32(Bernal and Yang, 2014)/6.16(Yuan *et al.*, 2015)	a = 6.23(Stoumpos *et al.*, 2013)
	Tetragonal [$I4/mcm$]			
	Orthorhombic [$Pnma$]	a = 8.35 b = 9.17 c = 12.56		
CH₃NH₃SnBr₃	Cubic [$Pm\bar{3}m$]	a = 5.89 (6.08*)	6.00(Chiarella *et al.*, 2008)/5.96(Bernal and Yang, 2014)/5.99(Yuan *et al.*, 2015)	a = 5.88(Chiarella *et al.*, 2008)
	Tetragonal [$I4/mcm$]			
	Orthorhombic [$Pnma$]	a = 7.64 b = 8.84 c = 11.60		
CH₃NH₃SnCl₃	Cubic [$Pm\bar{3}m$]	a = 5.68 (5.98*)	5.88(Yuan *et al.*, 2015)	a = 5.72
	Tetragonal [$I4/mcm$]			
	Orthorhombic [$Pnma$]	a = 7.16 b = 8.43 c = 11.72		

Table 3.6 Calculated lattice constants (in Å) of MAGeX_3 halide perovskite materials in different phases compared to other theoretical and experimental results. The numbers in parenthesis are obtained without vdW interactions.

Materials	Symmetry	Lattice constants (A°)		
		Present-PBE	Another cal. (Sun *et al.*, 2016)	Expt.(Stoumpos *et al.*, 2015)
CH₃NH₃GeI₃	Trigonal [*R3m*]	$a = b = 8.42$ $c = 11.24$ $\alpha = 90.1$ $\beta = 98.8$ $\gamma = 120.1$	$a = 8.69, b = 8.87$ $c = 11.53$ $\alpha = 88.27$ $\beta = 91.71$ $\gamma = 121.55$	$a = 8.55, b = 8.55$ $c = 11.16$ $\alpha = 90.0$ $\beta = 90.0$ $\gamma = 120.0$
CH₃NH₃GeBr₃	Trigonal [*R3m*]	$a = b = 7.90$ $c = 11.05$ $\alpha = 90.0$ $\beta = 89.9$ $\gamma = 120.1$	$a = 8.34, b = 8.49$ $c = 10.92$ $\alpha = 88.51$ $\beta = 91.01$ $\gamma = 121.53$	
CH₃NH₃GeCl₃	Trigonal [*R3m*]	$a = b = 7.70$ $c = 10.80$ $\alpha = 90.7$ $\beta = 89.4$ $\gamma = 120.2$	$a = 8.07, b = 8.42$ $c = 10.42$ $\alpha = 88.44$ $\beta = 91.17$ $\gamma = 122.63$	

CHAPTER IV

EFFECTS OF THE VAN DER WAALS INTERACTIONS

ON STRUCTURAL AND ELECTRONIC PROPERTIES

OF CH₃NH₃(Pb,Sn)(I,Br,Cl)₃ HALIDE PEROVSKITES

4.1   Introduction

Perovskites are crystalline materials with an *ABX₃* structure similar to the CaTiO₃ mineral. The *A*-site cations are 12-fold coordinated and divalent *B*-site cations are 6-fold coordinated. In the class of organic-inorganic halide perovskite materials, the *A*-site is a monovalent organic cation, e.g. methylammonium ($CH_3NH_3^+$, MA^+), the *B*-site is a divalent metal, e.g. Pb^{2+}, Sn^{2+}, Ge^{2+} and the *X*-site is occupied by the halogen ions e.g. I^-, Br^-, Cl^-. Recently, hybrid halide perovskite materials have emerged as new promising materials in photovoltaic applications. This class of materials has been known for a long time and has been studied in relation to their very particular dielectric properties (Poglitsch and Weber, 1987). However, the first application of organo-halide perovskite materials in photovoltaics can be traced back to 2009, with the work of Kojima and co-workers (Kojima *et al.*, 2009). After the pioneering work, the number of applications of the hybrid perovskite in photovoltaics rapidly increased, especially in the case of lead-halide perovskite materials (Stoumpos *et al.*, 2013; Park *et al.*, 2015; Weller *et al.*, 2015). Notably, the solar cell efficiencies of halide perovskites have risen very quickly to about 20 % where they become competitive with Si solar cells

(Sahoo *et al.*, 2018; Tonui *et al.*, 2018; Shi and Jayatissa, 2018). However, numerous challenges remain about their stability and structural transformations.

The crystal structures of Pb- and Sn-based halide perovskite materials are temperature dependent. Their exact structures are still unclear because of an increasing degree of deformations introduced by the MA^+ cation group. The crystal structures and phase transitions upon the temperature of the studied ABX_3 perovskites were explained and summarized in Section 3.1. For the organic-inorganic halide perovskite materials, the MA-cation group resides within the network of corner-sharing BX_6 octahedra and are stabilized by vdW interactions. Some previous theoretical works (Egger and Kronik, 2014; Li and Rinke, 2016; Yin *et al.*, 2014; Brivio *et al.*, 2014) have already revealed the importance of the inclusion of the vdW interactions in these types of materials on structural properties, at least, by including dispersive forces description to exchange-correlation term. The effect of the MA orientations on the electronic structure is under debate. The MA is considered to cause little direct effect on the band edge states. This is due to the characteristic of the states near the band edges that are either Pb-s, I-p mixed at the VBM and Pb-p like at the CBM. Conversely, the MA orientations indirectly affect the crystal structure by lifting octahedral symmetry which leads to splitting of the states near the band edges.

In this work, we conducted a vdW-corrected density functional theory (DFT) calculations to examine the importance of vdW interactions on the MA-cation structural properties and consequently to the electronic properties of the $MABX_3$ (B = Pb, Sn; X = I, Br, Cl) halide perovskite materials. It is expected that the vdW interactions in DFT calculations impact the MA-cation orientation, which influences the structural properties of the inorganic network and consequently affects the electronic properties

of the materials. The PBE with vdW-corrected DFT is a widely accepted approach to obtain the structural properties that are in good agreement to the measurement but the main drawback is the underestimation of the band gap. To address this underestimation, the quasiparticle self-consistent GW method, more accurate and computational intensive method, is used to perform the electronic structure calculations for the structures obtained from PBE with vdW-corrected DFT. Additionally, spin-orbit coupling is known to be important in the Pb-based compounds. Therefore, we investigate the effect of both GW self-energy corrections and spin-orbit coupling on the electronic structure in relation to the orientation of the MA molecules and their corresponding induced structural distortions. The spin-orbit coupling in combination with the electric field induced symmetry breaking arising from the dipolar molecules leads to the Rashba effect, which can affect the conduction band minimum location in k-space. In order to investigate solely the effect of the orientations of the MA-cation on the electronic structures, the cubic primitive cell of the MABX_3 (12 atoms per unit cell) is used in all calculations. The orientations of the MA-cation have significantly affected to the BX_6 inorganic framework and consequently effect to the electronic properties of the materials. It has been found that the results are in good agreement with the other calculations which using the supercell approach.

4.2   Computational Methods

Throughout this work, the structural properties of studied materials are predicted using the first-principle DFT which is implemented in the Vienna *ab* initio simulation package (VASP) code (Kresse and Furthmüller, 1996; Kresse and Joubert, 1999). The semi-local generalized gradient approximations (GGA) combined with the

Perdew-Burke-Ernzerhof (PBE) (Perdew *et al.*, 1996) functional are used as the primary exchange-correlation functional. The vdW corrections were also employed to study their effects on the structural and electronic properties of the studied materials. The projected augmented wave (PAW) (Kresse and Joubert, 1999; Blöchl, 1994) method with plane-wave basis set energy cut-off of 520 eV is employed in all calculations (Kresse and Joubert, 1999). The conjugate gradient algorithm (Golub and Ye, 1999) is used in the structural optimization until the energy difference between the iterations is less than 10^{-4} eV. The Monkhorst-Pack scheme (Monkhorst and Pack, 1976) of k-points is used in the Brillouin-zone integrations. An 8×8×8 mesh is used in the structural optimization and electronic properties calculations. Recent studies (Egger and Kronik, 2014; Li and Rinke, 2016; Yin *et al.*, 2014) revealed that vdW force plays an important role in a range of materials with weak interaction, such as organic-inorganic halide perovskite compounds, especially in their geometry optimization. Therefore, to study the effects of internal interaction between the MA^+ cation and BX_6 inorganic framework, we performed the full structural relaxation (volume and atomic position are allowed to relax) including vdW-interactions using the zero damping DFT-D3 method described by Grimme *et. al*. (Grimme *et al.*, 2010) as described in section 2.5 and then we used the relaxed structures to calculate the corresponding electronic band structures both at the DFT and many-body perturbation theory GW level.

The cubic primitive cell of the $MABX_3$ (12 atoms per unit cell) has been used in this work. As a matter of fact, under working temperature, the MA molecules are nearly free to rotate inside the cuboctahedral BX_6. It is more important to investigate the range of the change in energy level near the band edge. In this work, various MA orientations

within the cubic unit cell have been studied in order to determine the range of variation of electronic structures as molecules rotating inside the perovskite cage.

It is well known that the GGA-PBE usually underestimates band gaps of semiconductors. Fortunately, for MAPbI$_3$ the GGA-PBE without spin-orbit coupling (SOC) gives unexpectedly good agreement of the calculated bandgap with the experimental value. This is due to a compensation of the errors of the GGA-PBE and the lack of spin-orbit coupling. For confirmation, the more accurate Heyd-Scuseria-Ernzerhof (HSE) screened hybrid functional (HSE06) (Heyd *et al.*, 2003) is also used to calculate the band structures without including SOC for the band gaps. It is well known that the DFT-method treats core electrons by effective pseudopotential. To study the effects of the core electrons, the all-electron full-potential methods is needed to properly explain the electronic properties of the materials. Subsequently, to compare the results with the DFT method we also calculated the band structures using the all-electron full-potential linearized muffin-tin orbital (FP-LMTO) method (Methfessel *et al.*, 2000; Kotani *et al.*, 2007) as implemented in Questaal Suite (https://www.questaal.org.). In this method, the band structures are calculated using the quasiparticle self-consistent GW method (Kotani *et al.*, 2007; van Schilfgaarde *et al.*, 2006). The GW method is a many-body perturbation theoretical method introduced by Hedin (Hedin, 1965; Hedin and Lundqvist, 1970) in which the self-energy is approximated in terms of the one-electron Green's function *G* and screened Coulomb interaction, *W*, schematically $\Sigma = iGW$. While the GW self-energy operator is energy-dependent and non-hermitian, in the quasiparticle self-consistent (QS) GW approach, we replace it by an energy–independent but still non-local operator, determined in a

self-consistent manner. With independent particle Hamiltonian H_0, and its eigenvalues and eigenfunctions at hand, both the Green's function G_0 and the polarization function P_0 could be obtained. The screened Coulomb interaction is then given by

$$W = \varepsilon^{-1}v, \tag{4.1}$$

where the dielectric function is derived by

$$\varepsilon = 1 - v\chi. \tag{4.2}$$

The irreducible polarizability (χ) is derived as

$$\chi = \frac{\delta p}{\delta V} = -iGG\Gamma. \tag{4.3}$$

The self-energy is obtained as $\Sigma = iG_0W_0$. This quantity is actually obtained from the basis set of the eigenstates of H_0. A correction to the exchange-correlation potential is then derived by

$$\left[\Delta v_{xc}\right]_{ij} = \frac{1}{2}\mathrm{Re}\left\{\Sigma_{ij}\left(\varepsilon_i\right) + \Sigma_{ij}\left(\varepsilon_j\right)\right\} - v_{xc}^0 \tag{4.4}$$

which is added to the previous H_0 to obtain a new H_0. The procedure is iteratively computed until $\Delta v_{xc} = 0$ and henceforth quasiparticle self-consistent. When the convergence condition is reached, the quasiparticle energies are the same as the Kohn-Sham eigenvalues. The energy dependence of the GW self-energy and its imaginary part or lifetime is thus ignored but the quasiparticle energies are correctly including the dynamical effects of the electron-electron interactions.

4.3 Results and Discussion

4.3.1 Structural Relaxation

The molecular orientations in the cubic phase of MAPbI$_3$ have been studied by Motta *et al.* (Motta *et al.*, 2015) and Bechtel *et al.* (Bechtel *et al.*, 2016). It is worth mentioning that both works are particularly relevant to our study.

I) Motta *et al.* (Motta *et al.*, 2015) performed a full structural optimization of MAPbI$_3$ within GGA and including vdW corrections. It has been found that the results are sensitive to the initial orientation of the molecule being along [100] or [111]. In the former case, it rotates toward a [110] or equivalent direction, while in the latter case, it remains in the [111] direction. Both the [110] and [111] orientation are reported to be energetically favorable orientations. It is interesting to extend that approach to other halogens and to the case of Sn instead of Pb.

II) More systematic approach to map out the energy landscape regarding the orientation of the inserted molecule has been done by Bechtel *et al.* (Bechtel *et al.*, 2016). All possible rotation degrees of freedom of the molecule have been comprehensively carried out in term of polar angle θ and azimuthal angle ϕ of the C-N axis of the molecule with respect to the [001] and [100] cubic axes, and the rotation angle α of the molecule about its own axis and the displacement of the molecule from its center along its own axis. The energy landscape of the molecule as a function of those mentioned variables has been mapped out while keeping the inorganic framework fixed. Their main finding is that the displacement of the molecule (translation along its own direction away from the nominal center of the dodecahedral site) is important to

the structural optimization. The optimum orientations found in their work are close to [100] and [111] directions.

Based on two mentioned works, the structures starting from either [100], [110] or [111] orientation of the molecule are fully relaxed by allowing a shift of the molecule and the distortions of the framework. Subsequently, the energy landscapes are mapped out by performing constrained calculations where the molecule is constrained at some angle (inspired by the energy landscape studies of Bechtel *et al.* (Bechtel *et al.*, 2016) but the molecule is free to rotate and displace relative to the inorganic framework). The calculations of all configurations are then performed with and without vdW corrections to ascertain their importance. The structural properties are discussed together with the effect of the vdW corrections on the electronic band structure, accordingly. Ferroelectric ordering was found to be slightly energetically preferable by Quarti *et al.* (Quarti *et al.*, 2014). On the other hand, Weller *et al.* (Weller *et al.*, 2015) reported the disordered alternating non-polar orientation of the MA molecules.

Let us start the discussion by presenting the relaxed crystal geometries. Initially, the structural optimizations have been performed at the level of the GGA-PBE calculations with and without including the vdW interaction for revealing the effects of internal interactions between the organic cation and the BX_6 inorganic framework. We perform a full structural relaxation without any symmetry constraints from the ideal cubic perovskite structure with staggered H-atoms arrangement adopted from Motta *et al.*'s calculation (Motta *et al.*, 2015), as depicted in Figure 4.1. The relaxations have been performed with various initial configurations of the MA-cation, namely oriented along the [100], [110], or [111] directions, as listed in Table 4.1. We note that the relaxation process is extremely sensitive to the initial MA-cation orientation. For

example, when we started the relaxation with the MA$^+$ cation oriented along the [111] direction, the relaxed structure preserves its original MA$^+$ cation orientation in both cases of with and without including vdW interaction, as depicted in Figure 4.2(c) and (d), respectively. This result is similar to that of Motta *et al*. (Motta *et al.*, 2015). The calculated change in angle ($\Delta\theta$) of the C-N axis with respect to its initial orientation direction is very small, as shown in Table 4.1. In contrast, if we start the structural relaxation with the MA$^+$ cation oriented along the [100] direction, the relaxed structure does not preserve its original MA$^+$ cation orientation, instead, it may end up with the MA$^+$ cation orientated along a [10-1] direction, as depicted in Figure 4.2(a) and (b). The reason why particularly the [10-1] direction is favoured as opposed to the in-principle equivalent [1±10] or [101] depends on the particular chosen orientation of the molecule about its own axis. As we will show later the H atoms are in such positions to favour rotating in this particular direction by optimizing the hydrogen bonds with the halogen. This is why the vdW interactions are important. In this case, the MA$^+$ cation shifts down along the *x-z* plane (see the inserted picture in Figure 4.3) with the calculated change in angle, ($\Delta\theta$) around 18° (in case of MAPbI$_3$) when including the vdW interaction, as shown in Table 4.1. But, if one does not include the vdW-interaction in the calculation, the calculated $\Delta\theta$ in this case is around 7.8° and the relaxed structure is less distorted as shown in Figure 2 (b). Including the vdW interaction, the calculated $\Delta\theta$ of the C-N axis with respect to the [100] direction increases when the halogen atom is changed from I$^-$ to Br$^-$ to Cl$^-$ in both Pb- and Sn-based cases, as shown in Figure 4.3. The increase of the angle indicates a stronger interaction between the organic MA$^+$ cation and the *BX$_6$* inorganic framework and causes the relaxed structure to become more distorted, as indicated by a *B-X-B* bond angle tabulated in Table 4.1. The calculated lattice

parameters, when including the vdW interaction, are in very good agreement with the experimental values, with an error less than 1%. If the calculation does not include the vdW interaction, the calculated lattice parameters are larger than the experimental values by an error more than 3% (comparing calculated results in Table 4.1 and experimental results in Table 3.1).
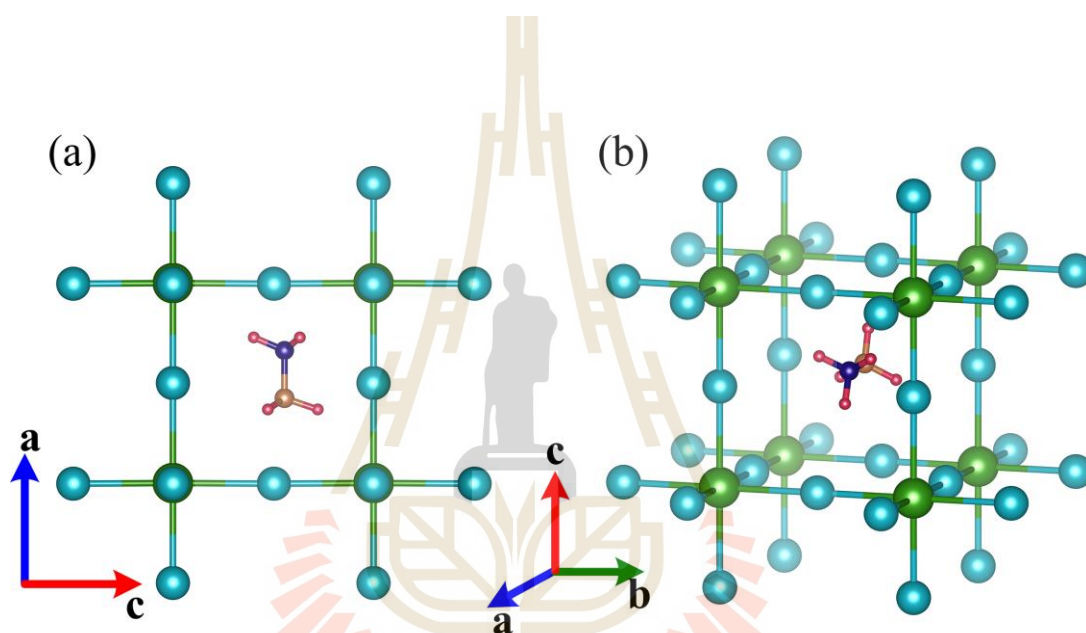
Figure 4.1 Illustration ideal cubic structure of $CH_3NH_3BX_3$ with staggered H-atoms arrangement in CH_3NH_3 molecule which is oriented along the [100] direction viewed along (a) a-crystallographic axis and (b) arbitrary crystallographic axis. Green, cyan, blue, orange, and red spheres represent the B-site atoms, X-site atoms, N-atom, C-atom, and H-atoms respectively.
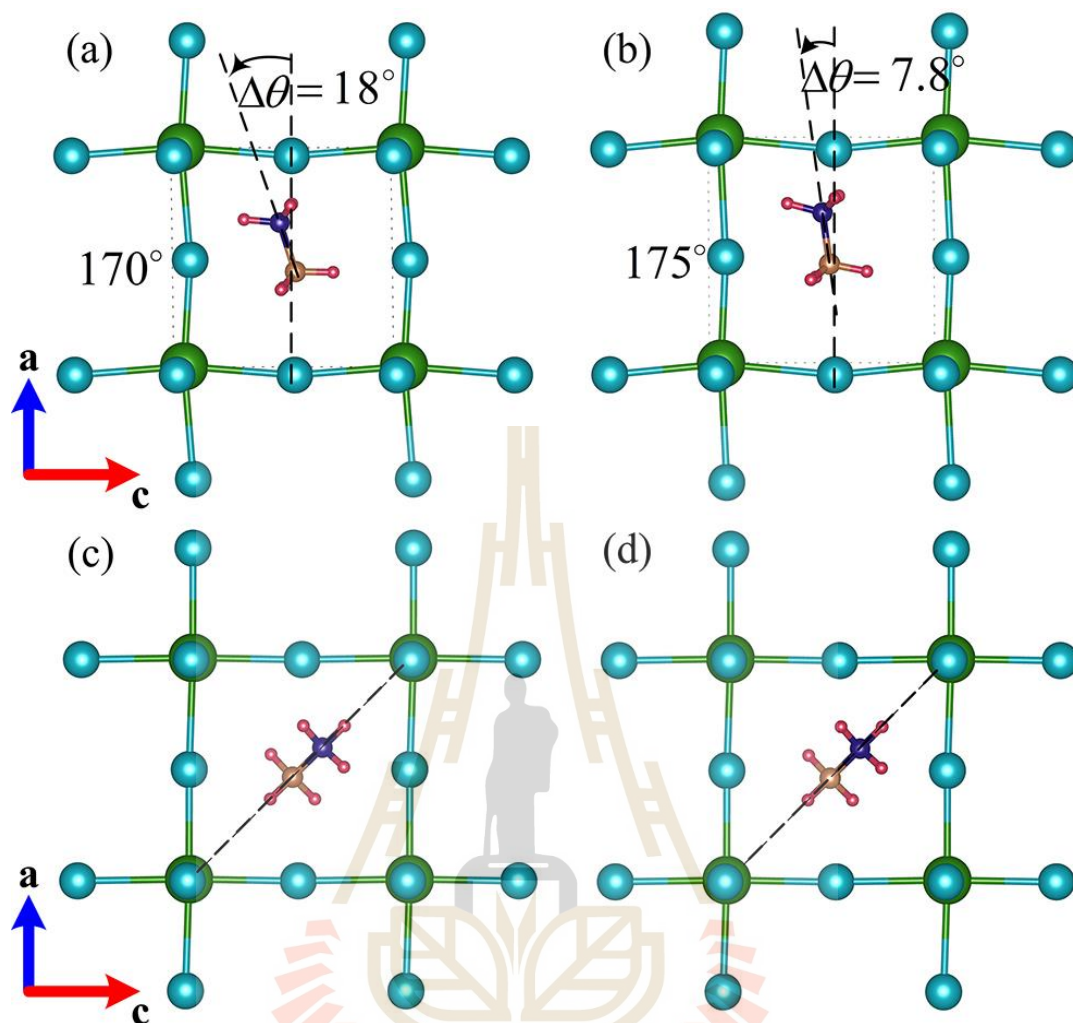
Figure 4.2 Illustration of relaxed structures of the cubic $CH_3NH_3PbI_3$ with and without vdW-interaction (Left and right panel) for different orientations of the MA^+ cation. (a) and (b) represent the relaxed structure of the MA-cation initially oriented along the [100] direction, (c) and (d) represent the relaxed structure of the MA-cation initially oriented along the [111] direction. The pictures are viewed along the y-axis or showing the x-z plane.

Table 4.1 Calculated lattice constants a, b, and c (Å), unit cell volume V (Å^3), deviate angle from the given initial MA-orientation, $\Delta\theta$ (degree), relative energy (meV), *B-X-B* bond angle (in degree) and hydrogen bond lengths (Å) of MA*BX*$_3$. The numbers in parenthesis are obtained without vdW interactions.

| Compounds | Int. MA orient. | Calculated structural parameters | | | | | | B-X-B bond angle | H-bonding | |
		Rel. E	$\Delta\theta$	a	b	c	V		H_N-X	H_C-X
MAPbI$_3$	[100]	0.00	18	6.34	6.30	6.38	254.7	169.5	2.72	3.36
			(7.8)	(6.48)	(6.43)	(6.49)	(270.2)	(174)	(2.8)	(3.6)
	[110]	14.4	9	6.34	6.40	6.27	252	175	2.75	3.40
			(5.6)	(6.48)	(6.57)	(6.32)	(270.4)	(175)	(2.8)	(3.6)
	[111]	21.0	0.9	6.34	6.34	6.34	255.3	178	2.71	3.38
			(0.5)	(6.47)	(6.47)	(6.47)	(270.4)	(178)	(2.7)	(3.6)
MAPbBr$_3$	[100]	0.00	23	5.94	5.89	6.03	211	169.1	2.45	3.31
			(12.7)	(6.03)	(6.03)	(6.13)	(222.8)	(172)	(2.5)	(3.4)
	[110]	18.6	6.8	5.98	5.98	5.89	209.8	174	2.55	3.50
			(4.6)	(6.08)	(6.08)	(6.03)	(221)	(173)	(2.5)	(3.5)
	[111]	35.4	0.9	5.97	5.97	5.97	212.7	177	2.41	3.10
			(1.2)	(6.08)	(6.08)	(6.08)	(223.4)	(177)	(2.5)	(3.5)
MAPbCl$_3$	[100]	0.00	26	5.67	5.63	5.79	184.7	168	2.3	3.17
			(17.5)	(5.74)	(5.73)	(5.90)	(193.8)	(171)	(2.4)	(3.2)
	[110]	23.1	6.6	5.73	5.73	5.63	184.2	174	2.3	3.3
			(4.6)	(5.83)	(5.83)	(5.73)	(193.9)	(175)	(2.4)	(3.2)
	[111]	46.4	0.8	5.73	5.73	5.73	187.6	175	2.3	2.9
			(1.3)	(5.83)	(5.83)	(5.83)	(197.2)	(176)	(2.4)	(3.2)
MASnI$_3$	[100]	0.00	20.1	6.26	6.19	2.27	243	172	2.7	3.3
	[110]	6.4	8.5	6.26	6.26	6.17	241.3	172	2.8	3.4
	[111]	20.3	0.01	6.24	6.24	6.24	243.4	177.4	2.7	3.3
MASnBr$_3$	[100]	0.00	26.5	5.89	5.80	5.95	202.9	170.6	2.43	3.2
	[110]	9.00	8.6	5.91	5.91	5.80	201.6	171	2.45	3.1
	[111]	34.6	0.03	5.88	5.79	5.95	204.5	176	2.47	3.05
MASnCl$_3$	[100]	0.00	28.4	5.72	5.55	5.75	182.6	171	2.25	2.89
	[110]	8.92	4.6	5.71	5.71	5.54	179.2	172	2.25	2.86
	[111]	33.17	0.03	5.70	5.70	5.70	185.4	176	2.26	2.85

If we focus on the relaxed structures, the significant difference between these structures is the deformation of the BX_6 octahedra. In the case of initially [100]-orientation, the relaxation of the MA^+ cation induces the deformation and a symmetry reduction of the inorganic BX_6 octahedra. Such distortion causes the *B-X-B* bonds to not lie parallel to the crystal directions but instead be slightly tilted by ~10° from the ideal cubic structure when vdW interaction is included (see Table 4.1). However, when excluding vdW interaction, they only tilted by ~5° from the ideal cubic structure. In the case of [111]-orientation, the *B-X-B* bond angles are very close to 180°, indicating that the relaxed structure preserves a high symmetry cubic structure. In this case, the relaxed structure of the [111]-orientation is still simple cubic (see Table 4.1). In contrast, the relaxed structure of the initially [100]-orientation becomes tetragonal (c/a ≠ 1).

Additionally, the calculated hydrogen bond lengths are listed in Table 4.1. The results show that the hydrogen atoms on the NH_3-side are closer to the BX_6 inorganic framework than those of the CH_3-side. It can be implied that the hydrogen atoms in NH_3-side dominate the strong interaction with the BX_6 inorganic framework. Although the relaxed structure is sensitive to the initial MA^+ cation configuration, it is worth to notice that the energy difference between these configurations is very small. The energy difference is calculated to be in the 21- 50 meV range in favour of a direction near the [100] direction, which is consistent to the previous studies of $MAPbI_3$ (Motta *et al.*, 2015; Bechtel *et al.*, 2016). The lowest energy structure we found ($MAPbI_3$ case) is consistent with lowest energy structure calculated by Qiaoling Xu *et al*. (Xu *et al.*, 2019) which using 2×2×2 supercell calculations, where the MA-cations are found in favoured oriented to [012] direction with the relative energy ~60 meV per formula unit

and experimental results done by Hutter *et. al.* (Hutter *et al.*, 2017). Indeed, it can be implied that these MA^+ cation configurations represent the local energy minima.
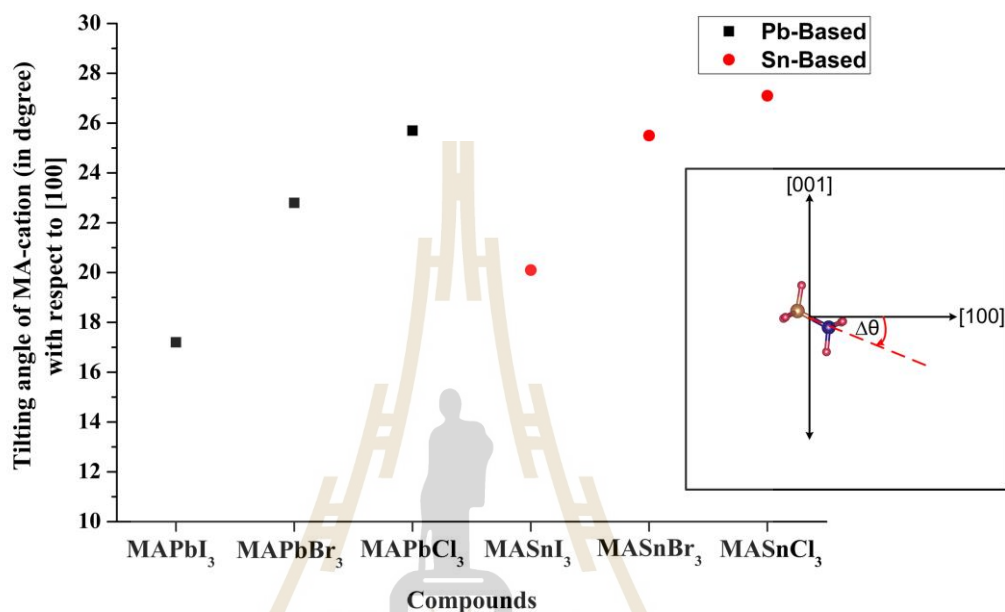
Figure 4.3 vdW-calculated tilting angle of the MA-cation with respect to the initially [100] orientation ($\Delta\theta$), as represented in an inserted picture.

After the full structural relaxation of the initially [100]-orientation has been done, it is still unclear why the MA^+ cation rotated downward in the *x-z* plane instead of other directions. Therefore, we have chosen the MAPbI$_3$ case as an example for further study. We performed the ground state energy calculation as a function of the rotational angle of C-N axis with respect to the [100] direction including the vdW interactions. Several pathways namely [100]→[10-1], [100]→[110], and [100]→[111] are considered. In the calculations, the staggered H-atoms arrangement is applied and C-N axis is fixed at each rotational angle while the other atoms and also cell volume

are allowed to relax. The calculated energies as a function of rotational angle in different pathways are depicted in Figure 4.4. From the plot, we can see that the calculated energies in [100]→[10-1] pathway decrease until the rotational angle is around 20° and then the energy increases. This is consistent with the full unconstrained minimization presented above. At the lowest energy structure, three hydrogen atoms in NH_3-side bond with I^- atoms almost equally, as depicted in Figure 4.4(a). The energy difference between [100]- and [10-1]-orientation is very small, 3.5 meV. On the other hand, the calculated energies in the [100]→[110] pathway slightly fluctuate with the rotational angle and end up with the energy 10 meV higher than that of the [100]-orientation. In this case at the lowest energy point, one of the hydrogen atom in NH_3-side bonds with the I^- atom stronger than other two hydrogen atoms, as depicted in Figure 4.4(b). In case of [100]→[111] pathway, the calculated energy slightly increases and then decreases until the rotational angle is around 22°, then increase and end up with the energy 9 meV higher than that of the [100]-orientation. In this case, at the lowest energy structure, two of hydrogen atoms on the NH_3-side show stronger bonds with the I^- atoms than the other hydrogen atom, as depicted in Figure 4.4(c). The lowest energies along the [100]→[110] and [100]→[111] pathways are ~7 meV higher than along the [100]→[10-1] pathway. In addition, we can see that the energy difference in 15°-25° range of the [100]→[10-1] pathway is very shallow, indicating several local minima around that point. The difference in these different pathways lies in the way the molecule's H is positioned relative to the halogen atoms along these paths. The more complex behaviour for other than the optimal rotation pathway (a) shows that there is some optimal orientation of the molecule about its own axis such that it best optimizes the H bonds with the halogens.
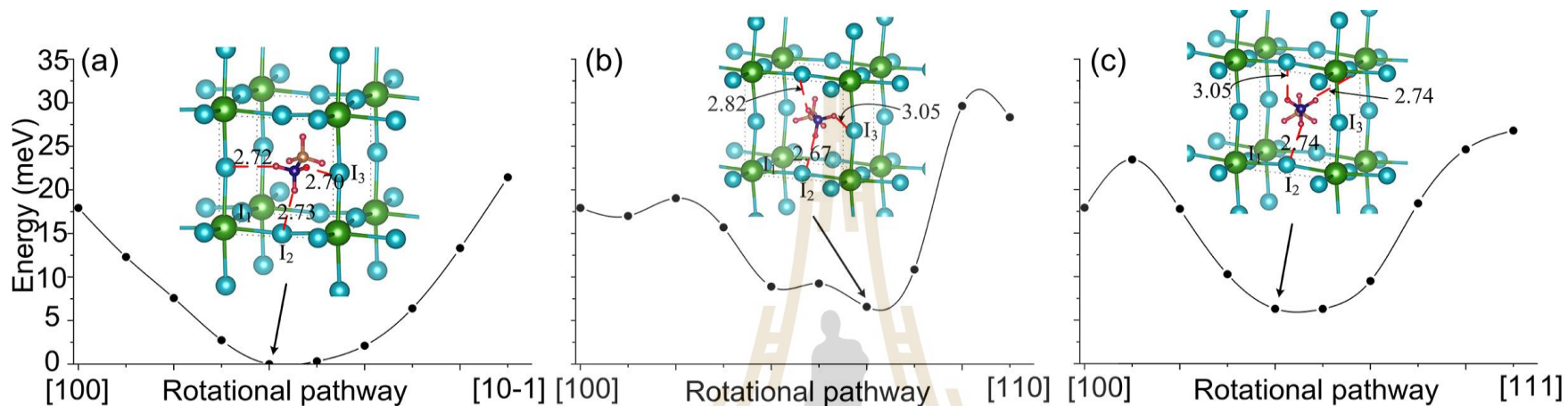
Figure 4.4: Calculated relative energy (for MAPbI$_3$ case) as a function of the rotational pathway of C-N axis with respect to [100] direction. (a) Represents [100]→[10-1], (b) represents [100]→[110], and (c) represents [100]→[111]. The C-N atoms are fixed at each rotational angle while the other atoms are allowed to relax. The inserts show the orientation and the hydrogen bond lengths (red dashed lines) that can form with the nearest halogen atoms near the minimum configuration.

From our calculated ground state energies in different pathways, we conclude that the fully structural relaxation process of the initially [100]-orientation with the given staggered H-atoms arrangement including the vdW interaction ends up with the MA^+ cation rotated downward in the *x-z* plane from [100] toward [10-1] in a local minimum energy near the [100] direction with the deviate angle, $\Delta\theta$ listed in Table 4.1.

4.3.2 Electronic Properties

The significant differences in the structural geometries are expected to impact on the electronic structure of the studied MA*BX*$_3$. First, let's pick MAPbI$_3$ as an example to explain the effect of the vdW interaction on the electronics properties of the studied materials. The electronic band structures along high-symmetry points of the Brillouin zone calculated by using the GGA-PBE without SOC with different MA^+ cation orientations of the MAPbI$_3$ are depicted in Figure 4.5. Our GGA-PBE calculated band structures reveal that the orientations of the MA^+ cation have a profound impact on the nature of the bandgap of MAPbI$_3$. In case of the [111]-orientation, the relaxed structure keeps the high symmetry of the cubic structure and gives the direct bandgap at the *R*-point (0.5, 0.5, 0.5) of the Brillouin zone both with and without vdW interaction, as depicted in Figure 4.5(b) and (c). On the other hand, in the case of the initially [100]-orientation, the relaxed structures are strongly distorted due to the cation rotation and consequently affect the band structure: the conduction band minimum (CMB) shifts along with the $R\rightarrow\Gamma$ line, the bandgap becomes indirect, as depicted in Figure 4.5(c). These results are in good agreement with Motta *et al* (Motta *et al.*, 2015). Please note that the Grimme DFT-D3 approach (Grimme *et al.*, 2010) changes the total energy and hence relaxation but not the exchange-correlation potential used for the

band structure calculations. In the case of exclusion of vdW interactions, the calculated bandgap remains direct for both [100]- and [111]-orientation, as depicted in Figure 4.5 (a) and (b), respectively. This indicates that the relaxed structures do not present enough distortion to modify the band structure significantly and the vdW-correction is necessary for the structural relaxation of the halide perovskites systems.

The vdW-calculated bandgap without SOC of $MAPbI_3$ lies in the 1.45-1.55 eV (see Table 2) range close to the experimental value of about 1.55 eV (Kojima *et al.*, 2009; Lee *et al.*, 2012), while the calculated bandgap without vdW-interaction lies in 1.6-1.7 eV, slightly larger than the experimental values. The GGA-PBE calculations usually underestimate the bandgap of semiconductors. However, as already shown in the case of $MAPbI_3$ (Mosconi *et al.*, 2013), the agreement here is due to a fortuitous cancellation of the errors of the GGA underestimated bandgap and the lack of spin-orbit interaction which would tend to overestimate the gap. To test the robustness of the indirect bandgap, we also used the HSE06 hybrid functional to calculate the electronic band structures of the $MAPbI_3$ by using the GGA-PBE+vdW-relaxed structures. The band structures of the $MAPbI_3$ calculated by the HSE-functional without SOC are also depicted in Figure 4.5(e) and (f) and we can see that the indirect bandgap persists when the screened hybrid functional is included. Although, the calculated bandgap of the $MAPbI_3$ by using the HSE06 lies in 1.90-1.95 (see Table 4.2) eV range, larger than that one from the experimental value, as expected.
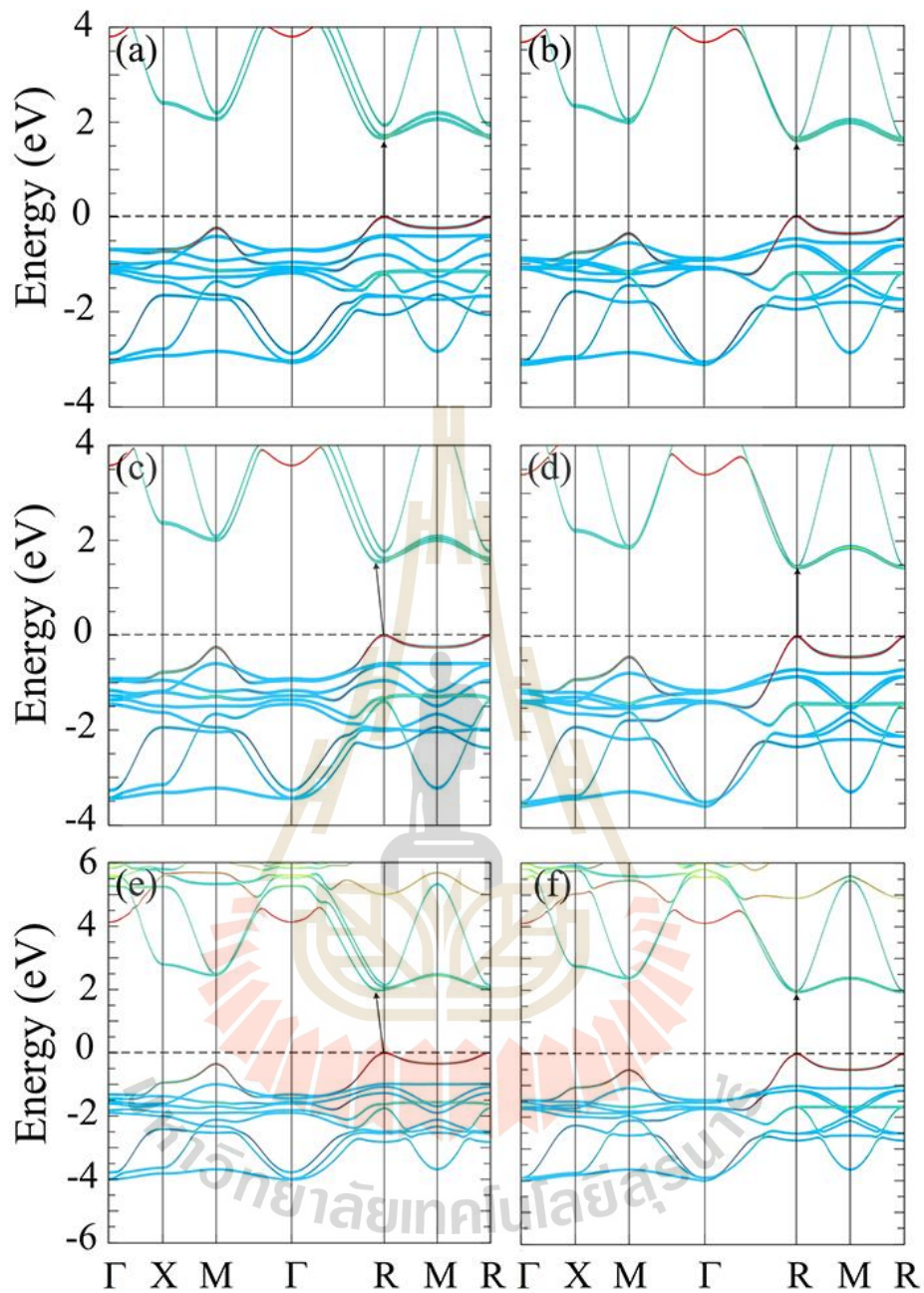
Figure 4.5 Calculated band structures without SOC of the CH₃NH₃PbI₃ for (a-b) PBE without including vdW, (c-d) PBE with including vdW and (e-f) HSE with including vdW. Left and right panels represented to the MA⁺ cation initially orientated along [100] and [111] directions. The red, skyblue and lime colours of each band represent *spd*-projected wavefunction character of *s*, *p*, and *d* orbitals, respectively. The calculated VBM were shifted to zero.

Table 4.2 Calculated band gaps (eV) of the studied MA*BX*₃ compounds for different MA orientations at varied levels of approximation in comparison with available experimental data.

Compounds	Int. MA orient.	Calculated bandgap					Expt.
		PBE	PBE+ SOC	HSE	QSGW	QSGW+ SOC	
MAPbI₃	[100]	1.55	0.47	1.99	2.47	1.79	
	[110]	1.50	0.48	-	-	-	1.55
	[111]	1.45	0.44	1.95	2.40	1.65	
MAPbBr₃	[100]	1.93	0.84	2.51	3.13	2.55	
	[110]	1.86	0.84	-	-	-	2.30
	[111]	1.80	0.70	2.43	3.01	2.28	
MAPbCl₃	[100]	2.41	1.30	3.10	3.91	3.49	
	[110]	2.30	1.33	-	-	-	2.90
	[111]	2.31	1.23	3.04	3.80	3.33	
MASnI₃	[100]	0.50	0.10	1.29			
	[110]	0.47	0.10	-	-	-	1.20
	[111]	0.49	0.10	1.26 (0.77)			
MASnBr₃	[100]	0.76	0.32	1.90			
	[110]	0.76	0.38	-	-	-	2.14
	[111]	0.75	0.30	1.88			
MASnCl₃	[100]	1.83	1.46	3.10			
	[110]	1.33	1.03	-	-	-	3.6
	[111]	1.49	1.06	2.94			

Note: the HSE band gaps of Pb-based are obtained with 25% exact exchange while the HSE band gaps of Sn-based are obtained with 55% exact exchange since based on the experimental band gap of MASnI₃ and a number in parenthesis is obtained with 25% exact exchange.

We note that indirect gaps or, more specifically, a displacement of the CBM away from the high-symmetry point have previously been obtained due to the Rashba (Brivio *et al.*, 2014) effect. However, the results here are obtained without SOC and thus have a different origin: namely the distortions of the inorganic framework in response to the orientation of the MA molecules. Because of the *B-6p* contributes to the CMB while the *X-5p* and *B-6s* contribute to the VMB of these materials. From our calculated results, it is clear that the molecular orientation can strongly influence to the electronic structure of the hybrid perovskites by affecting the *X-B-X* inorganic framework which take part in frontier orbital and a little bit change the bandgap of the materials, which will be discussed in next section.

For the other studied compounds, the direct bandgaps are also found in case of the [111]-orientation, while the indirect bandgaps are found in all cases of distorted BX_6 octahedral due to the cation rotation. However, the GGA-PBE calculations now underestimate the bandgap, as shown in Table 4.2, when compared with the experimental values. This shows that the good agreement for $MAPbI_3$ is really a coincidence and less perfect cancellation of errors occurs in the other cases. At any rate, the full band structures in GGA-PBE without SOC have significant errors even for MAPI. The electronic band structures of the other compounds are depicted in Figure 4.6. We can also see that the indirect bandgaps persist for all studied compounds in case of initial [100]-orientation when the screened hybrid functional is included. The HSE-calculated bandgap without SOC of $MAPbBr_3$ and $MAPbCl_3$ lies between 2.43-2.51 eV and 3.04-3.10 eV, respectively (see Table 4.2), which is slightly larger than the experimental values. The HSE-calculated bandgap without SOC of Sn-based compounds lies in the 1.26-1.29 eV range for $MASnI_3$, 1.88-1.90 for $MASnBr_3$, and

2.94-3.10 for MASnCl$_3$ which is slightly smaller than the experimental values (see Table 4.2).
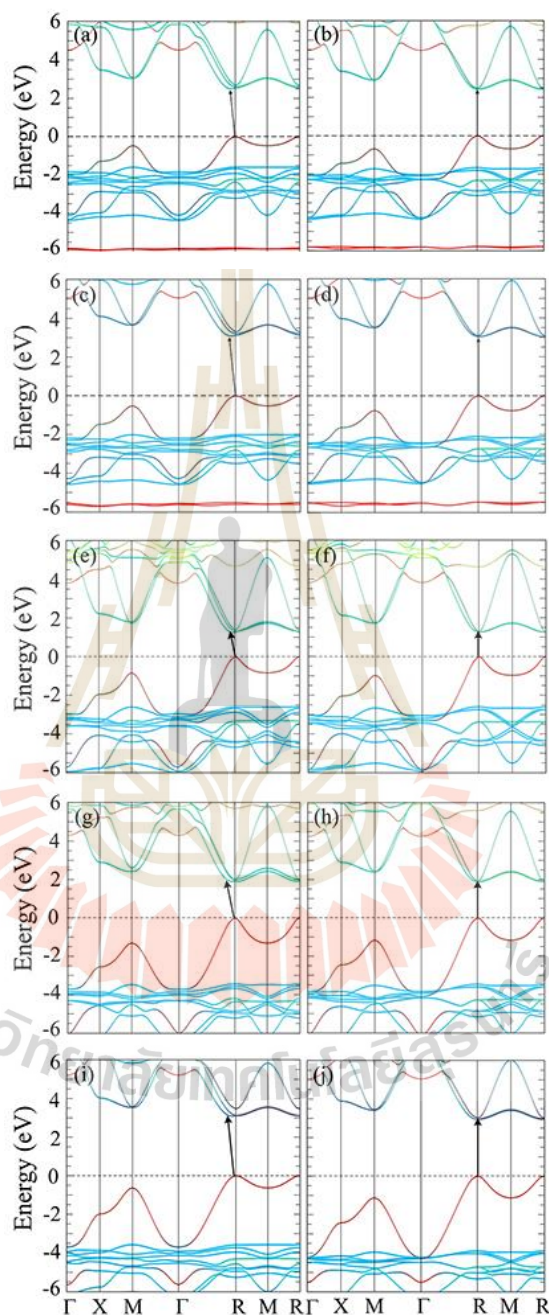
Figure 4.6 HSE-Calculated band structures without SOC of the other studied compounds. (a-b) for MAPbBr$_3$, (c-d) for MAPbCl$_3$, (e-f) for MASnI$_3$, (g-h) for MASnBr$_3$ and (i-j) for MASnCl$_3$. Left and right panels represented to the MA+ cation initially orientated along [100] and [111] directions, respectively.

While the above study indicates that the indirect gap found in the structures obtained from the initial [100] direction of the molecule is robust when considering different functionals, we need to further study the combined effect of spin-orbit coupling and the gap corrections beyond semilocal functionals. In fact, the distortion induced shift of the CBM may be related to the closeness of the bands which remain nearly degenerate at the R-point when SOC is neglected. One might expect that adding SOC could remove this effect. However, when we add spin-orbit coupling alone without using hybrid functionals to open the gap, the latter will be so strongly reduced that the CBM is then close to the VBM and this may then lead to other artifacts. Instead of combining HSE with SOC we decided here to use the QSGW+SO because it is in principle an even more accurate approach.

The band structures of the Pb-based compounds in QSGW approximation and at the GGA-PBE relaxed structures are shown in Figure 4.7. We can see from our calculated results that the QSGW band structures of the initially [111] MA orientation exhibit the direct bandgap at R point both with and without SOC. On the other hand, the QSGW band structures of the near [100] MA$^+$ orientation are different: the CBM is slightly shifted from $R \rightarrow \Gamma$ as found in our DFT band structures, without SOC. This indirect nature is already obtained in QSGW even without SOC. Nonetheless, the band structures are still substantially different when SOC is included, namely, they are spin-split and the origin of the indirect gap is now clearly affected by the Rashba effect.
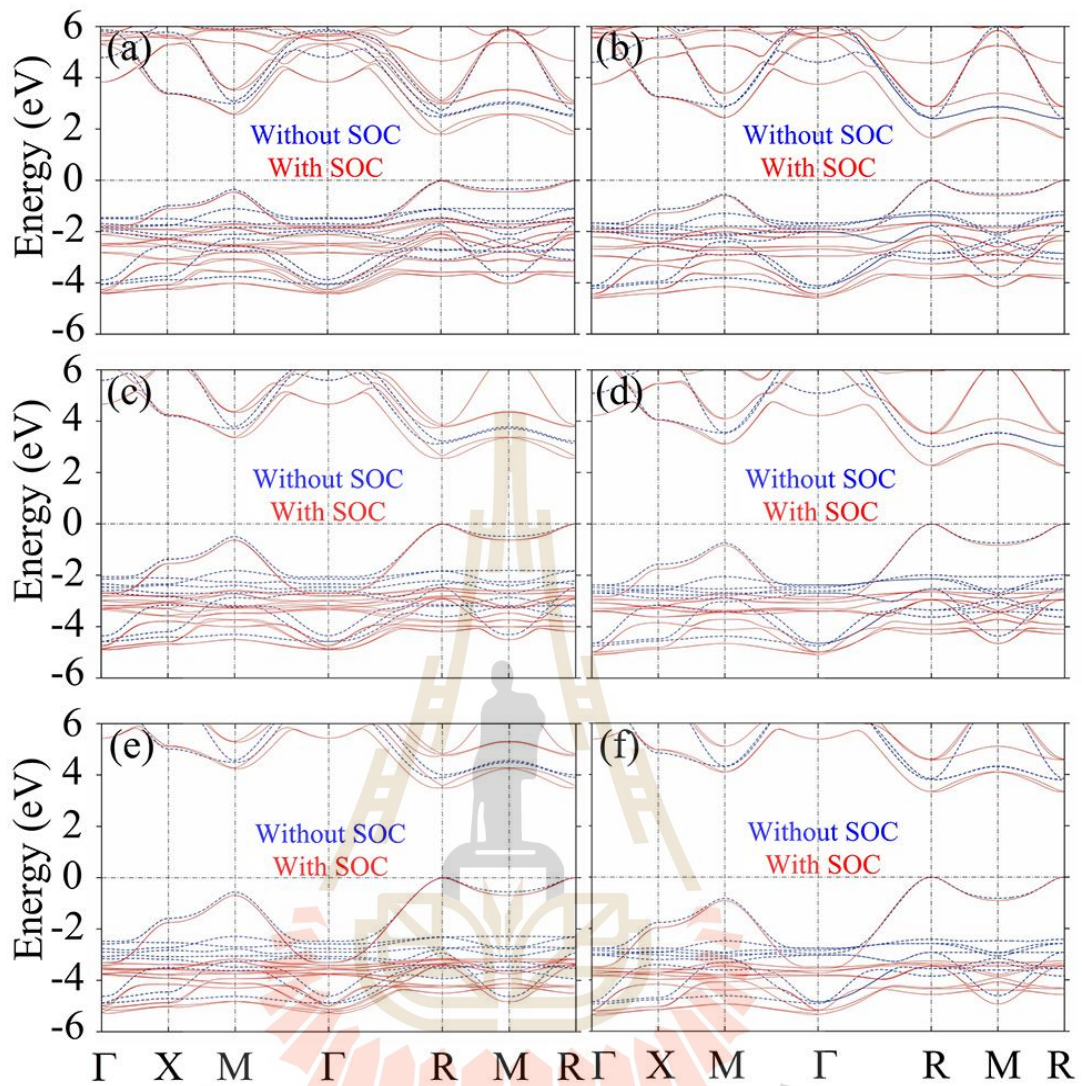
Figure 4.7 Calculated band structures in QSGW approximation with (red) and without (blue) SOC of the (a-b) $CH_3NH_3PbI_3$, (c-d) $CH_3NH_3PbBr_3$ and (e-f) $CH_3NH_3PbCl_3$. Left and right panels represented to the MA+ cation initially orientated along [100] and [111] directions, respectively.

Our calculated QSGW band structures in case of MAPbI$_3$ are qualitatively consistent with Brivio *et al*. (Brivio *et al.*, 2014) results in which the representative [100] configuration of the MA$^+$ cation was selected. In their work, a similar spin-splitting of the CBM and its shift away from the *R* point is found while for a smaller NH$_3$ molecule with less clear molecular dipole orientation instead of the MA this effect is not seen. In recent work, the size of this effect was studied as a function of local distortions obtained from molecular dynamics snapshots and found to be present even in CsPbI$_3$ due to the possibility of local Pb off-centering which like the MA molecules also can lead to the required symmetry breaking to have a Rashba effect (Brivio *et al.*, 2014). Their calculated QSGW bandgaps are 2.70 eV (SOC=0) and 1.67eV (added SOC). Our calculated band gaps in QSGW approximation are also listed in Table 4.2. We can see that the QSGW band gaps calculated without SOC are much larger than the experimental values and the gaps are reduced by approximately 0.7±0.1 eV when the SOC is considered. We note here that the orientations of the MA$^+$ cation are found to have an important impact on the nature of the bandgap also at the level of QSGW approximation.

To further describe the indirect bandgap, let's define the energy difference between the CBM and the conduction band at *R*-point of Brillouin zone, $\Delta E \equiv E^R - E^{CBM}$, as shown in an inserted picture of Figure 4.9. The PBE calculated ΔE of the studied compounds is depicted in Figure 4.9. From our calculated results, we can see that the energy difference, ΔE of the Pb-based compounds is larger than that of the Sn-based compounds. This is resulting from the more distorted structure of the Pb-based compounds compared to the Sn-based ones. We note that the bandgap shifting does not occur only with the [10-1]-orientation, the indirect bandgap does appear for the

equivalent orientations, for examples, [10±1], [01±1], [1±10]. As shown in Figure 4.8

below, in the case of the [101]-orientation, the CBM shifts along with the $R \rightarrow M$ line.
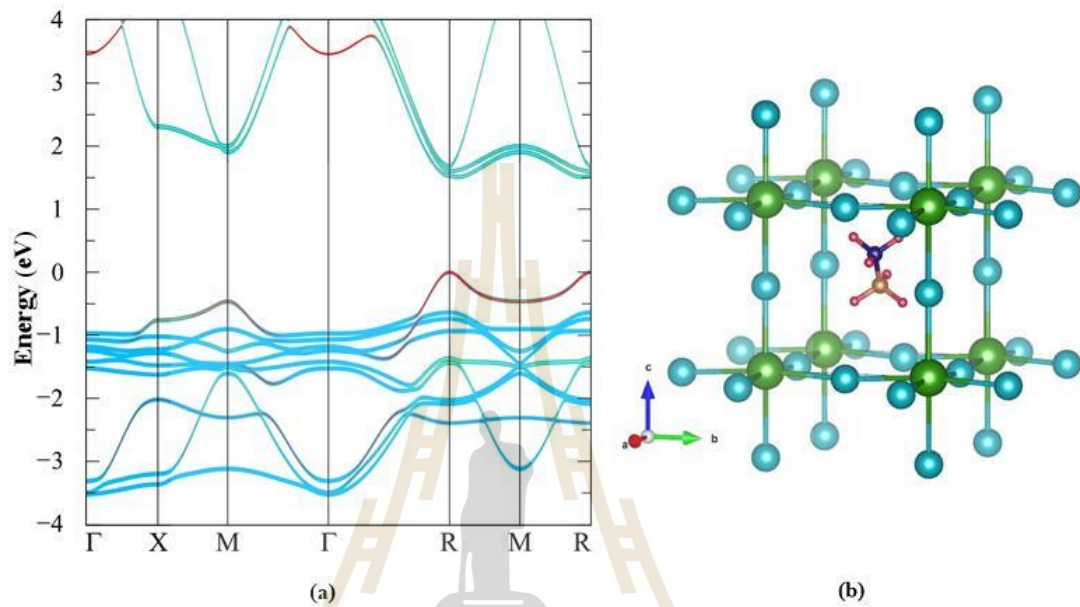
Figure 4.8 (a) The calculated band structures of the fully relaxed crystal structure

including of vdW interaction calculated using the GGA-PBE without SOC of MAPbI$_3$

for the MA-cation initially orientated along [101] direction shown as the structure (b).
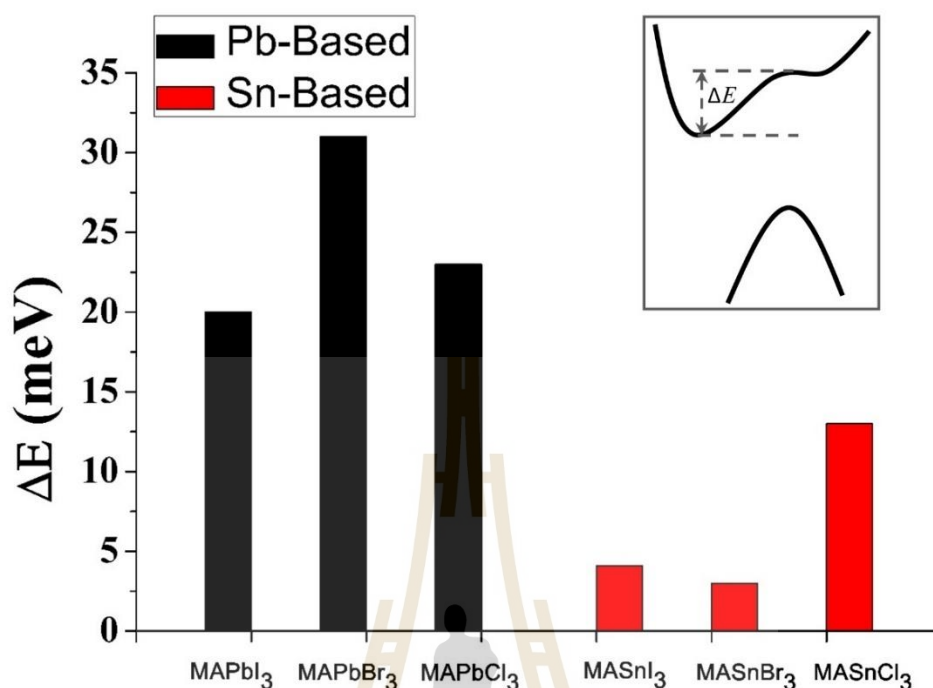
Figure 4.9 PBE-calculated energy difference, ΔE between the CBM and the conduction band at R-point of Brillouin zone in case of the indirect bandgap.

The MA^+ cation has often been assumed to not have any significant contribution to the electronic structure around the band edges. From our calculated density of states results of $MAPbI_3$, it is obviously seen that the bottom of the conduction band mainly consists of the p orbitals of the Pb-atom, while the top of the valence band is mainly derived from the p orbital of the I-atoms and the Pb-s orbital, as depicted in Figure 4.10(b). When considering the organic molecule, the highest occupied molecular orbital of the MA^+ cation is found deep below the valence band, ~5 eV below the valence band maximum (VBM). Thus one may argue that there is no effect of the MA^+ cation in the optical and electronic response of such materials, rather it does only contribute to their structural cohesion by donating its charge to the rest of the system. However, a closer

inspection of the density of states projected on the various atoms (Figure 4.10(a)) reveals that there is a small contribution of the MA-cation ~0.5 eV below the VBM. This indicates that indeed there is an interaction between the MA-cation and the inorganic PbI_6 octahedral framework, in the form of hydrogen bonding. To further understand the effect of the interactions between the MA-cation and the inorganic framework in electronics properties of these materials, we removed the MA-cation from the PBE+vdW relaxed structure of the initially [100]-orientation and calculated the electronic band structures. This is to check the interactions between the MA-cation and the framework. Note that, by removing the MA-cation one electron is missing from the band, therefore there is a hole in the valence band and the Fermi-level shifted down below the VBM. To do charge neutralizing, we added one electron to the system and then calculated the band structure. The calculated band structure, in this case, preserves the same feature of indirect bandgap as one obtained from the $MAPbI_3$-unit cell, as shown in Figure 4.11. This indicates that the MA-cation in the system just donates its electron to the inorganic framework, it does not affect the band structure near the band edge. But its orientation played a role in the relaxed structure of the inorganic framework and causes the structural distortion of the framework leading to the symmetry breaking and the CBM is a bit shifted away from high symmetry point. In our cases, the rotation of MA-cation can create a variation of the bandgap of $MAPbI_3$ ~0.2 eV (~13% wrt. experimental gap of 1.55eV), as shown in Figure 4.12. Therefore, in the real system the cation rotations can slightly change the bandgap (should less than 13%). The lowest band gap is found to 1.43 eV which corresponded to calculated absorption spectrum ~865 nm and the highest band gap is found to 1.64 eV which corresponded to calculated absorption spectrum ~756 nm, respectively. It is expected

that the variation of the bandgap for this material would be within 0.2 eV. The average band gap of MAPbI3 is found to 1.54 eV which corresponded to calculated absorption spectrum ~805 nm. From our calculated results, it has been revealed that the vdW-correction is important to obtain an accurate description of the interactions between the MA-cation and the inorganic framework for the structural relaxation of the halide perovskites system. This interaction induces the deformation of the PbI_6 octahedral framework leading to the distorted structure of PbI_6 framework; the band structure is changed from direct to the indirect bandgap.
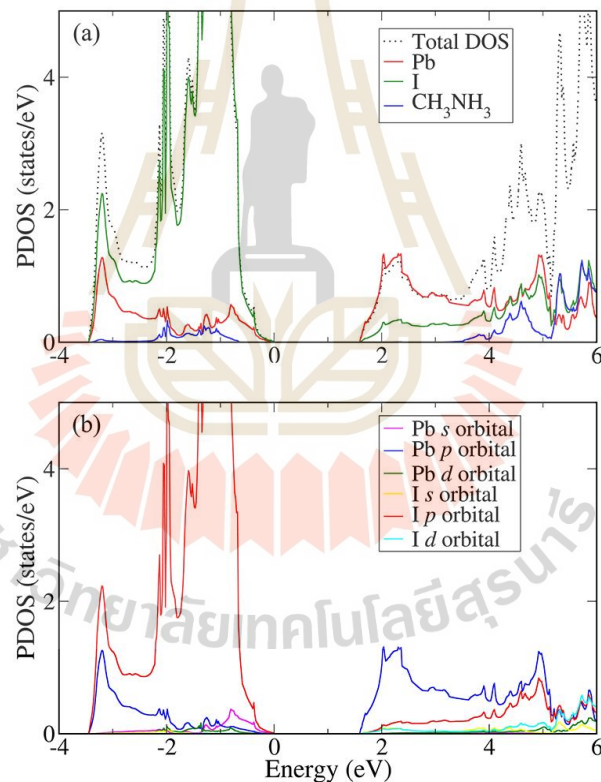
Figure 4.10 (a) The calculated total density of states (DOS) (dashed curve) of $CH_3NH_3PbI_3$ for the case of [111]-oriented molecule and projected density of states (PDOS) on the Pb-atom (red), I-atoms (green) and CH_3NH_3 (blue). **(b)** PDOS on orbitals of the Pb-atom and I-atoms.

(a)   (b)
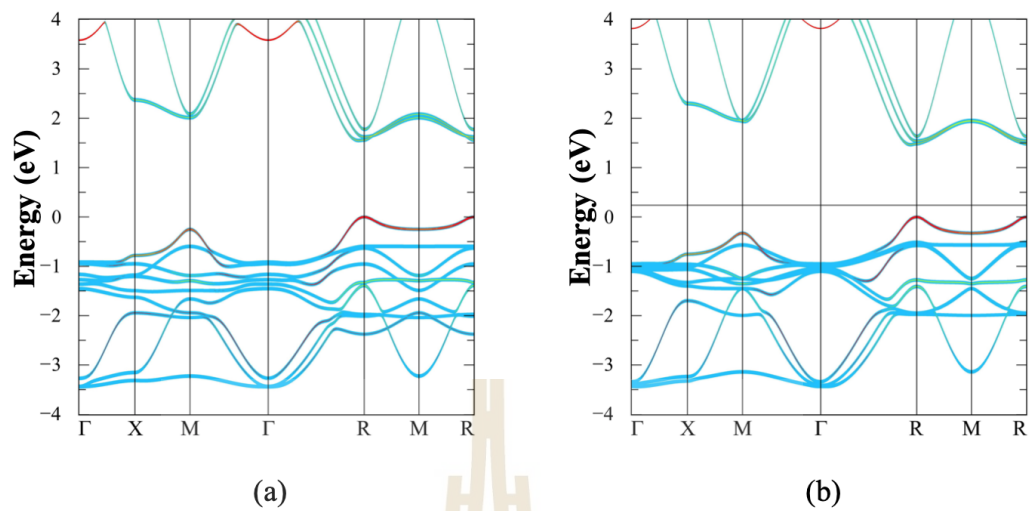
Figure 4.11 (a) The calculated band structures of the PBE+vdW relaxed structure of

the MAPbI$_3$ unit cell with the MA-cation initially orientated in [100] direction, and (b)

the calculated band structures of the PBE+vdW relaxed structure of Pb-I host without

MA-cation in the structure. The black horizontal line in (b) represents the Fermi-level.
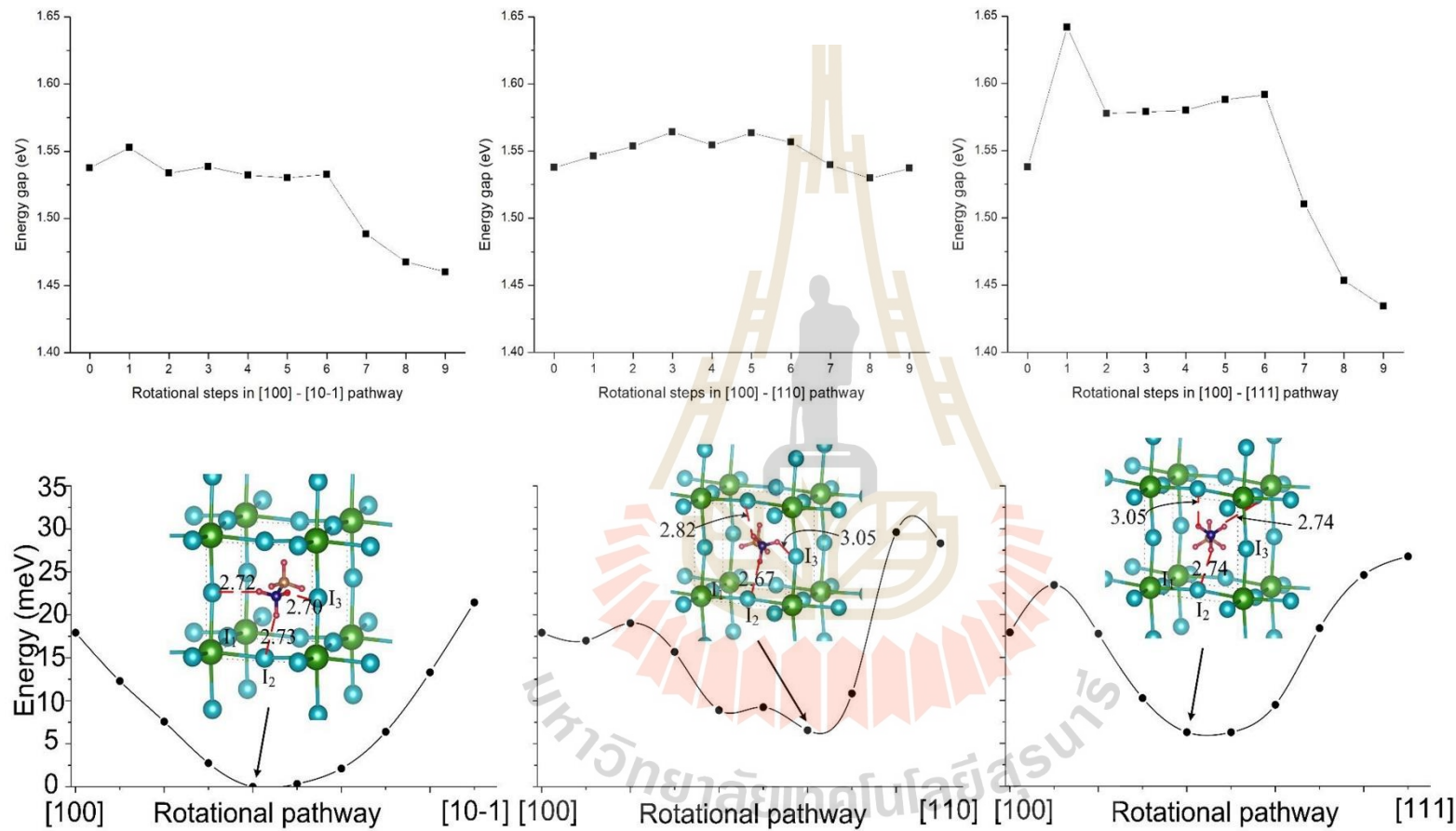
Figure 4.12 The calculated variation of the bandgap of MAPbI$_3$ (upper panel) as a function of the rotational pathway of C-N axis with respect to [100] direction, the calculated relative energy as a function of the rotational pathway (lower panel) are also illustrated.

88

4.4   Conclusion

In this work, we have performed DFT+vdW correction calculations with various initial MA$^+$ cation orientations, namely [100], [110], and [111] for revealing the effects of the internal interactions between the MA$^+$ cation and the BX_6 inorganic framework of the CH$_3$NH$_3BX_3$ (B = Pb, Sn; X = I, Br, Cl) halide perovskite materials. Our calculations reveal that the vdW-interactions between the MA$^+$ cation and the inorganic framework are critical for internal geometry optimization and electronic properties calculations. Full structural relaxations including vdW corrected DFT give the better agreement of the lattice parameters with the experimental values than obtained without them. More importantly, full relaxations including vdW interaction of the MA-cation initially oriented along [100] direction give a strongly distorted structure of BX_6 inorganic framework, which results from the MA$^+$ cation rotation and consequently affects the electronic band structure, which changes from direct to the indirect bandgap. On the other hand, the relaxations without vdW correction do not present enough distortion of the BX_6 inorganic framework, the electronic band structures remain direct bandgap.

This result is found to be robust when considering different halogens and occurs in both Sn and Pb based compounds. It is also robust when using a more accurate hybrid functional or the GW method. Finally, the indirect gap is maintained for this orientation when including both quasiparticle self-energy corrections at the GW level and spin-orbit coupling. The latter leads to a Rashba effect which spin-splits the bands but the indirect nature is already present before adding the SOC. This clearly demonstrates that the main origin of the indirect gap lies in the distortions resulting from the structural distortions of the organic ion with the inorganic framework.

CHAPTER V

CONCLUSIONS AND FUTURE WORK

5.1 Conclusion

In this thesis, first-principles density functional theory (DFT) as implemented within the Vienna *ab* initio simulation package (VASP) code is employed to study the structural and electronic properties of ABX_3 (A = CH$_3$NH$_3$, shortly MA$^+$, B= Pb, Sn, X = I, Br, Cl) halide perovskite materials. van der Waals (vdW) correction to DFT is considered for revealing the effects of the internal interactions between the MA$^+$ cation and the BX_6 inorganic framework of studied materials. The high-temperature α-phase (cubic structure) is the main analysis structure. Various rotational directions of MA$^+$ cation, for examples [100], [110], and [111] etc., have been studied.

From the results in Chapter V, the vdW-interactions between the MA$^+$ cation and the inorganic framework play an important role in internal geometry optimization and consequently affects to electronic properties of the studied materials. The calculated lattice parameters with full structural relaxation including vdW corrected DFT show a good agreement with experimental values. More importantly, full relaxations including vdW interaction of the MA-cation initially oriented along [100] direction give a strongly distorted structure of BX_6 inorganic framework, which results from the MA$^+$ cation rotation and consequently affects the electronic band structure, which changes from direct to the indirect bandgap. On the other hand, the relaxations

without vdW correction do not present enough distortion of the BX_6 inorganic framework, the electronic band structures remain direct bandgap.

This result is found to be robust when considering different halogens and occurs in both Sn and Pb based compounds. It is also robust when using a more accurate hybrid functional or the GW method. Finally, the indirect gap is maintained for this orientation when including both quasiparticle self-energy corrections at the GW level and spin-orbit coupling. The latter leads to a Rashba effect which spin-splits the bands but the indirect nature is already present before adding the SOC. This clearly demonstrates that the main origin of the indirect gap lies in the distortions resulting from the structural distortions of the organic ion with the inorganic framework.

5.2   Future Research Plan

In the past few years, research in the field of organic-inorganic perovskite materials has been growing rapidly because of their inexpensive raw materials, simple fabrication, and their unique optical and electronic properties in photovoltaic applications. The organic-inorganic halide perovskites were first used as a light absorber in dye-sensitized solar cells in 2009 (Kojima *et al.*, 2009), exhibiting an initial power conversion efficiency of ~4. Since then, an efficiency of over 20% was achieved in very short development time (Zhou *et al.*, 2014; Yang *et al.*, 2015). In this type of organic-inorganic perovskites, Pb-based halide perovskites such as methylammonium lead iodide (MA)PbI$_3$ (Feng and Xiao, 2014; Liu *et al.*, 2016; Huang *et al.*, 2018), formamidinium (FA)PbI$_3$, (Hu *et al.*, 2014) and mixed halides like MAPbI$_x$Cl$_{3-x}$, (Trifiletti *et al.*, 2015) and MAPbI$_x$Br$_{3-x}$ (x =0-3) have until now dominated the mainstream research. However, one of the major issues of Pb-based perovskite solar

cells is that lead can cause serious pollution of the environment. Thus, finding alternative new eco-friendly materials substituting for Pb is necessary. For the most similar element to lead (Pb), tin (Sn)-based halide perovskites has also already been extensively studied. $MASnI_3$ has a similar structure as $MAPbI_3$ (although in different temperature ranges) and is expected to be an excellent light absorber similar to $MAPbI_3$. Experimentally, it was found to have an excellent bandgap for single material absorbing layer solar cells of about 1.3 eV (Stoumpos *et al.*, 2013; Umari *et al.*, 2014). However, the main problem with Sn-based perovkites is their crystal structural stability. They are sensitive to the ambient atmosphere with regards to oxygen and moisture. Sn^{2+} is easily oxidized to Sn^{4+}, which may cause the structure transformation and then reduce their photovoltaic performance. Besides the valence transition, other re-arrangements of the structure are possible. For example, in $CsSnI_3$, a "yellow phase" in which octahedra are edge- instead of corner-sharing is known to occur and to be potentially the ground state at room temperature, and this phase does not have suitable properties for photovoltaics compared to the perovskite structure because of its much larger gap (Huang and Lambrecht, 2013; Huang and Lambrecht, 2014; Huang and Lambrecht, 2016; Chung *et al.*, 2012).

Another potential alternative element for replacing Pb is Ge, which belongs to the same group 14 (IVA) metals. One difference of Ge-based perovskites to Pb- and Sn-based ones is that the inorganic $CsGeX_3$ (X = I, Br, Cl) compounds crystallize in a polar space group at ambient temperature. Stoumpos and co-workers (Stoumpos *et al.*, 2015) reported the structural and electronic properties of various $AGeI_3$ (A = Cs, organic cations), including of $MAGeI_3$. Their experimental results revealed that $MAGeI_3$ forms a trigonal structure (with R3m space group) with energy bandgap of 1.9

eV, it should not be suitable for using as the absorber in the solar cell. The reported crystal structure of MAGeI$_3$ shows the off-centered displacement of Ge-atoms, thus ferroelectric properties MAGeX_3 (X = Cl, Br, and I) materials are interesting.

From the theoretical point of view, several computational works have been reported for Pb- and Sn-based perovskites, however, the theoretical research in Ge-based is still temporarily unclear (Huang and Lambrecht, 2016). Huang and Lambrecht studied the inorganic CsGeX$_3$ compounds using first-principles calculations at the GW level (Huang and Lambrecht, 2016) and also studied their vibrational modes (Huang and Lambrecht, 2016). Recently, they further compared the prevalent distortion modes of the cubic perovskite for Pb, Sn, Ge and Si-based perovskites and found both the Ge and Si-based perovskites to behave differently from the Pb and Sn-based ones (Radha *et al.*, 2018). In fact, instead of octahedral rotations, they showed a ferroelectric off-centering of the group-IV atom along the [111] direction, which leads to the R3m structure. For the studies of electronic properties, Ping-Ping Sun and co-workers (Sun *et al.*, 2016) used the density functional theory (DFT) method to study the electronic properties of MAGeX_3 (X = Cl, Br, and I) compared to MAPbI$_3$ and MASnI$_3$. Xiaoqing Lu and co-workers (Lu *et al.*, 2016) also used the DFT to study the electronic properties of AGeX_3 (A= Cs, and organic cations, X = Cl, Br, and I).

In this work, we plan to systematically study the structural and electronic properties of Ge-based perovskites in the trigonal phase (*R3m* space group) by using the hybrid functional DFT method. Two halogen elements Br, and Cl have been substituted on the basis of the R3m AGeI$_3$ (A= Cs, and MA) model constructing different Ge-based perovskite structure to study their intrinsic properties. According to

the off-centering of Ge-atom from the octahedral center, the spontaneous polarization of AGeX_3 (A= Cs, and MA, X = Cl, Br, and I). will be calculated.

The calculations of structural and electronic properties could be performed by using the same approaches described in Chapter III. However, the calculations of spontaneous polarization can be explained by the so-called "modern theory of polarization" (Spaldin, 2012; King-Smith and Vanderbilt, 1993; Resta, 1992; Resta, 1994). The details of the theory will be discussed in the manuscript prepared soon.

Empirically, the tolerance factor, t introduced by Goldschmit (Goldschmidt, 1926) could be used to predict the crystallographic stability of the perovskite structure for ABX$_3$ compounds. Based on the ionic radii of A, B, and X ions, tolerance factor, t can be calculated by Eq. 3.2. For the studied Ge-systems, the A-site is an organic cation, MA$^+$ with the effective ionic radii 2.17 Å (Shannon, 1976; Kieslich et $al.$, 2014). X is the halide anion, where we adopt r_I = 2.2 Å, r_{Br} = 1.96Å, and r_{Cl} = 1.87 Å. For B-site cation, (Ge cation) we adopt r_B = 0.73 Å. The calculated tolerance factors of the studies MAGeX$_3$ are 1.05 (MAGeI$_3$), 1.09 (MAGeBr$_3$) and 1.11 (MAGeCl$_3$). The tolerance factors of the studied Ge-based perovskites are close to the empirically ideal cubic perovskite structure. However, the MA organic ion itself has a threefold symmetry and thus even for an essentially cubic inorganic framework, one might expect a trigonal overall symmetry if the molecules align with the body diagonal of the cubic structure. A trigonal symmetry can also occur when the Ge atom has displaced the center of the surrounding octahedron along the cubic body diagonal. Thus, there are two reasons why the hybrid Ge compounds are expected to have trigonal structures. The important parameters are the Ge off-centring and the organic molecule orientation.

According to the experimental results by Stoumpos *et al*. (Stoumpos *et al.*, 2015), successfully several hybrid germanium iodide perovskite materials were successfully synthesized. In the case of $CH_3NH_3GeI_3$ ($MAGeI_3$), they reveal that the $MAGeI_3$ forms a 3D framework with the GeI_6 corner-sharing octahedra. The octahedra adopt a trigonal distortion in the polar R3m space group. In the observed crystal structure, the MA cation orients itself along the rhombohedral crystallographic *c*-axis. The measured lattice constants are a = b = 8.55, c = 11.16 A° and the crystallographic angles are $\alpha = \beta = 90°$, $\gamma = 120°$. In such octahedral distortion, the six Ge-I bonds are separated into three short ones and three long ones. The measured short bonds are 2.73-2.77 Å and the long bond is 3.45 Å.

The optimized trigonal structures of the $MAGeX_3$ (X = I, Br, Cl) obtained in our structural relaxation calculations are depicted in Figure 5.1. In the optimized structures, the distorted GeX_6 octahedra interconnect though a corner-sharing pattern, and the MA cations align along the *c*-axis to balance the GeX_3 framework. The calculated lattice parameters of the trigonal structures $MAGeX_3$ are reported in Table 5.1. Our calculated lattice parameters are in good agreement with the other available theoretical and experimental results. The bonding between Ge - X halide atoms represents the covalent interaction in the structure. The short ones represent a strong covalent interaction and other long ones represent a weak interaction. The calculated Ge-X bond distances of the $MAGeX_3$ are also listed in Table 5.1 and compared with the experimental (in $MAGeI_3$) and other theoretical results. Our calculated Ge-X bond distances are found to be consistent with other available studies. The results indicate the Ge-X bond distances decreases with decreasing X-anion size from I to Br and Cl, respectively.

By inspecting the relaxed structures of the MAGeX$_3$, we can see that the crystal structure becomes more distorted from I to Br to Cl. The Ge-X-Ge bond angle slightly decreases from 167.4 to 160.7 to 160.4 when the anion changes from I to Br to Cl, respectively (see Table 5.1). As it is known that the MA cation can be stabilized by van der Waals (vdW) interaction with the inorganic anions, our calculated hydrogen bonds are also reported in Table 5.1. The minimum bond length of H$_N$-X is smaller than that of H$_C$-X, which indicates that the H$_N$ ion shows a stronger attraction to the halogen atom by vdW force. The hydrogen bond between the MA cation and the inorganic framework has a significant effect on the geometry of the studied MAGeX_3 materials.

After structural analysis, the electronic properties of the materials were calculated. Figure 5.2 shows band structures of the studied MAGeX_3 (X = I, Br, Cl) materials calculated within the GGA-PBE functional with the valence band maximum (VBM) set at 0 eV. The band structures of the studied MAGeX_3) materials exhibit a direct bandgap located at the A (0, 0, 0.5) position in the Brillouin zone. This k-point in the rhombohedral structure corresponds to the R-point at the corner of the BZ in the cubic structure. The calculated bandgap of the studied MAGeX_3 materials increases from 1.14 eV (for MAGeI$_3$), to 1.90 eV (for MAGeBr$_3$), to 2.81 eV (for MAGeCl$_3$). The increase of the bandgap results from the higher iconicity of the Br and Cl which place the center of the valence band deeper on an absolute energy scale. The VBM is an antibonding combination of Ge-s with halogen X-p orbitals while the CBM is a Ge-p based state as typical in the halide perovskites (Huang and Lambrecht, 2013). Our results are consistent with the theoretical results from Xiaoqing Lu *et al.* (Lu *et al.*, 2016) Ping-Ping Sun *et al.* (Sun *et al.*, 2016) as reported in Table 5.2. However, when comparing our calculated bandgap from the GGA-PBE calculations with the

experimental one, ~1.9 eV. for MAGeI$_3$ (Stoumpos *et al.*, 2015). It is obviously seen that the PBE results underestimate the bandgap of these materials. The unavoidable underestimated bandgap is the common observable of the GGA-PBE calculations.

In order to obtain an accurate bandgap, we also studied the electronic properties of these materials using the HSE06 hybrid functional, which is found to improve the band gaps in most semiconductors. In the original HSE06 functional (Heyd *et al.*, 2003), the fraction of non-local exchange is set to 25 % and the exact exchange is screened by keeping only the short-range part of the exact exchange by means of a complementary error function cut-off using a screening parameter μ~0.2 Å^{-1}. To further improve the gaps, one may treat these parameters empirically. The percentage contribution of non-local Hartree-Fock (HF) exchange was determined hereby seeking a good agreement between the calculated values and experimental results while keeping the screening parameter fixed. In this work, to determine the HF exchange with the greatest potential to produce accurate results, we performed hybrid functional calculation for the MAGeI$_3$ (whose experimentally band gap is 1.9 eV) with the exact HF exchange contribution set to 0 (as a standard DFT calculation), 25, 30, 40 and 50% respectively as shown in Figure 5.3. By referencing with the experimental band gap of MAGeI$_3$, the ideal exact hybrid functional contribution was found around 37%. We then used the same optimized hybrid functional contribution to perform the hybrid functional calculation of the other two materials, MAGeBr$_3$ and MAGeCl$_3$. The calculated band gaps with hybrid functional are also listed in Table 5.2. The band structures of the studied MAGe*X*$_3$ materials calculated by using the hybrid functional HSE06 are shown in Figure 5.4. The band structures still exhibit the direct bandgap at the A (0, 0, 0.5) position in the Brillouin zone but the gaps are now significantly larger.

To further understand the electronic properties of the studied materials, the density of states (DOS) and partial density of states (PDOS) are analyzed. Figure 5.5 shows the DOS and PDOS calculated by using the GGA-PBE functional of the studied MAGeX_3 materials with the VBM set at 0 eV. As shown in Figure 5.5, one can see that the main contribution to the states near the valence band maximum (VBM) of the three Ge-based perovskites comes from the p orbitals of the halogen atoms with an overlap of the s orbital of Ge atoms, while the states near the conduction band minimum (CBM) is dominated by p orbital of Ge atoms partly overlap with the p orbital of halide atoms. It can also be seen that the states near the gap have no contribution from the methyl ammonium orbitals as there are no sizable C, N or H contributions here. The highest occupied states of the MA cations occurred around -5 to -6 eV below the VBM. However, by closer inspection, they also have a weak contribution around -1 to -2 eV below the VBM in the valence band region and around +3 to +4 eV above the VBM in the conduction band region. This indicates that there are interactions between the MA cations and the inorganic framework of GeX$_6$ in the form of hydrogen bonding.

Next, because of the off-centering of Ge atom, we plan to study the ferroelectric properties of the Ge-based halide perovskites AGeX_3 (A = Cs$^+$, MA$^+$, X = I, Br, Cl), for example, the spontaneous polarization (p_s) due to the displacement of the Ge-cations will be calculated and compared to the well-known ferroelectric materials such as BaTiO$_3$, PbTiO$_3$, etc. In addition, the relationship between the elastic constants and the polarization properties can be further investigated. This information may lead to deeper understanding of the structural distortion giving rise to the polarization in the halide perovskites.

(a)

(b)

(c)

(d)

(e)

(f)
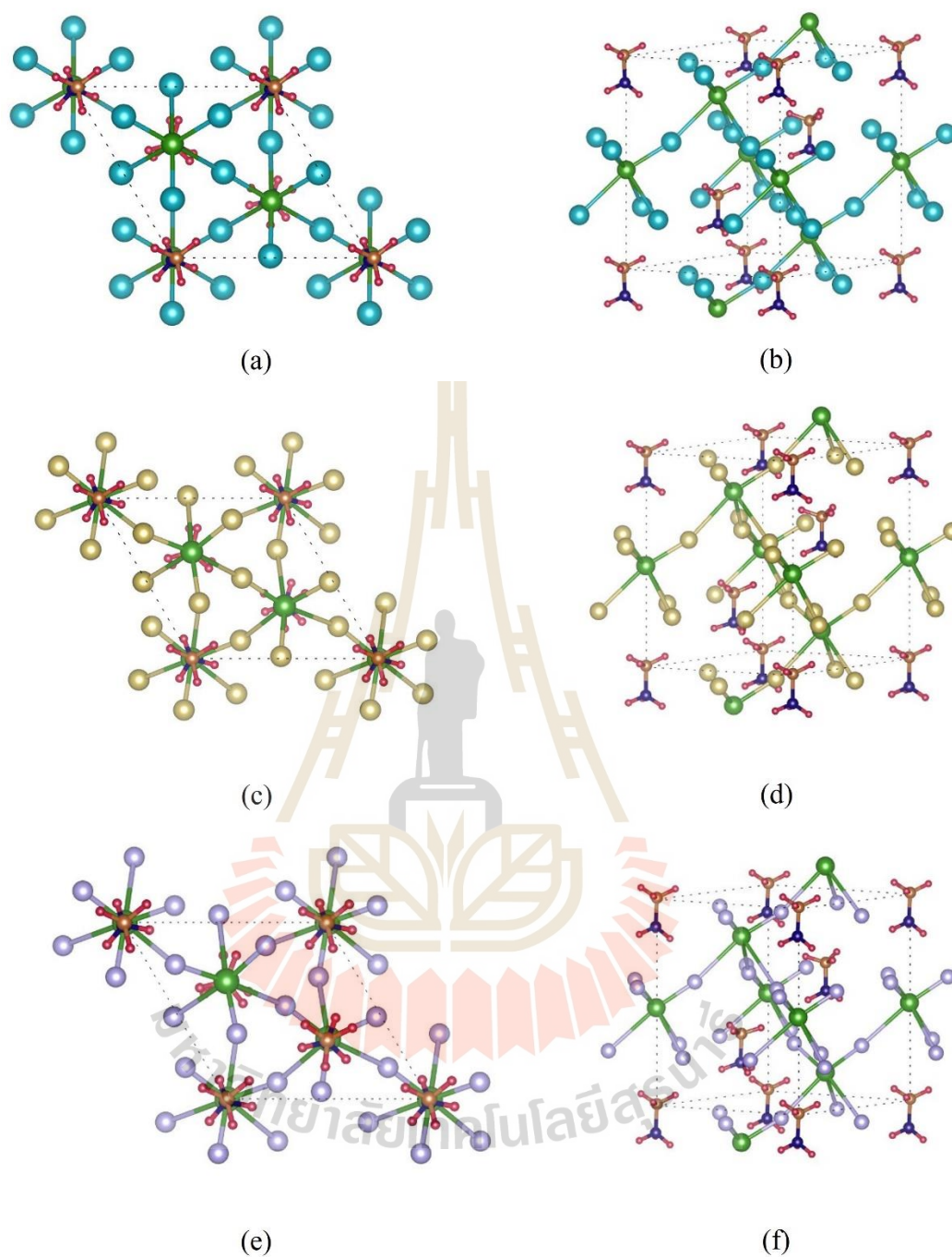
Figure 5.1 Optimized structures of (a-b) MAGeI$_3$, (c-d) MAGeBr$_3$, and (e-f) MAGeCl$_3$ halide perovskites in *R3m* crystal structure. The left panel is viewed along *ab*-plane, the right panel is viewed in an arbitrary axis. The I, Br, and Cl atoms are in soft-blue, soft-yellow, and grey respectively.

Table 5.1 Calculated lattice constants (Å), unit cell volume (Å^3), Ge-X bond length (Å), Ge-X–Ge bond angle (degree), and hydrogen bond distance (Å) of the MAGeX3 in *R3m* structure compared with available theoretical and experimental results.

Materials	Lattice parameters				Ge-X bond length		Ge-X-Ge bond angle		Hydrogen bonding	
	Present	Another cal.[a]	Another cal.[b]	Expt.[c]	Short	Long	Ap.	Eq.	H$_N$-X	H$_C$-X
CH₃NH₃GeI₃	$a = b = 8.42$ $c = 11.24$ V = 689.84 $\alpha = 90.1$ $\beta = 90.8$ $\gamma = 120.1$	$a = 8.69, b = 8.87$ $c = 11.53$ V = 757.65 $\alpha = 88.27$ $\beta = 91.71$ $\gamma = 121.55$	$a = b = 8.20$ $c = 11.34$ $V = 660.12$ $\alpha = 90$ $\beta = 98$ $\gamma = 120$	$a = 8.55, b = 8.55$ $c = 11.16$ V = 707.2(2) $\alpha = 90.0$ $\beta = 90.0$ $\gamma = 120.0$	2.74-2.78 2.77[d] (2.73-2.77[c]) 2.80[b]	3.42-3.47 3.45[d] (3.45[c]) 3.45[b]	166.4 167.7[d]	167.4 167.7[d]	3.2-3.4	3.3-3.6
CH₃NH₃GeBr₃	$a =$ b $=7.90$ $c = 11.05$ V = 594.84 $\alpha = 90.0$ $\beta = 89.9$ $\gamma = 120.1$	$a = 8.34, b = 8.49$ $c = 10.92$ V = 659.26 $\alpha = 88.51$ $\beta = 91.01$ $\gamma = 121.53$	$a = b = 7.64$ $c = 10.91$ $V = 552.01$ $\alpha = 90$ $\beta = 98$ $\gamma = 120$		2.54-2.56 2.60[b]	3.35-3.38 3.16[b]	160.5	160.7	2.9-3.0	3.1-3.3
CH₃NH₃GeCl₃	$a =$ b $=7.70$ $c = 10.80$ V = 551.81 $\alpha = 90.7$ $\beta = 89.4$ $\gamma = 120.2$	$a = 8.07, b = 8.42$ $c = 10.42$ V = 596.06 $\alpha = 88.44$ $\beta = 91.17$ $\gamma = 122.63$	$a = b = 7.28$ $c = 10.61$ $V = 487.54$ $\alpha = 90$ $\beta = 98$ $\gamma = 120$		2.38-2.39 2.44[b]	3.39-3.45 3.09[b]	166.7	160.4	2.8-3.1	3.0-3.2

[a] DFT calculation by Ping-Ping Sun *et. al.* (Sun *et al.*, 2016)
[b] DFT calculation by Xiaoqing Lu *et. al.* (Lu *et al.*, 2016)
[c] Experimental by Stoumpos *et al.* (Stoumpos *et al.*, 2015)
[d] Experimental by Zhang *et. al.* (Zhang *et al.*, 2015)

Table 5.2 Calculated energy bandgap of MAGeX3 halide perovskites in *R3m* structure, compared with available theoretical and experimental results.

Materials	Bandgap (eV)				
	Present Cal. PBE	Present Cal. HSE06	Another Cal. [a]	Another Cal [b]	Expt.
CH₃NH₃GeI₃	1.14	1.97	1.61	1.20	1.90[c]
CH₃NH₃GeBr₃	1.90	3.05	2.81	1.60	
CH₃NH₃GeCl₃	2.81	4.20	3.76	1.91	

[a] DFT calculation by Ping-Ping Sun *et. al*. (Sun *et al.*, 2016)
[b] DFT calculation by Xiaoqing Lu *et. al.* (Lu et al., 2016)
[c] Experimental by Stoumpos *et al*. (Stoumpos *et al.*, 2015)
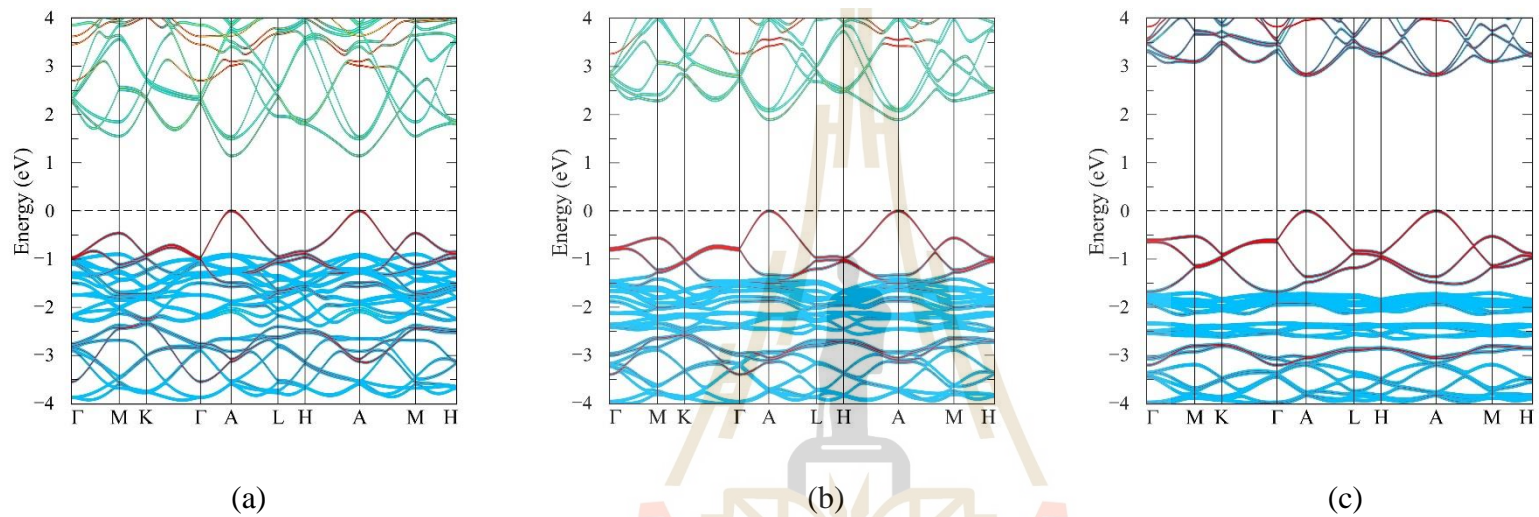
Figure 5.2 Band structure calculated by GGA-PBE without including SOC of (a) MAGeI₃, (b) MAGeBr₃, and (c) MAGeCl₃ halide perovskites in *R3m* crystal structure.
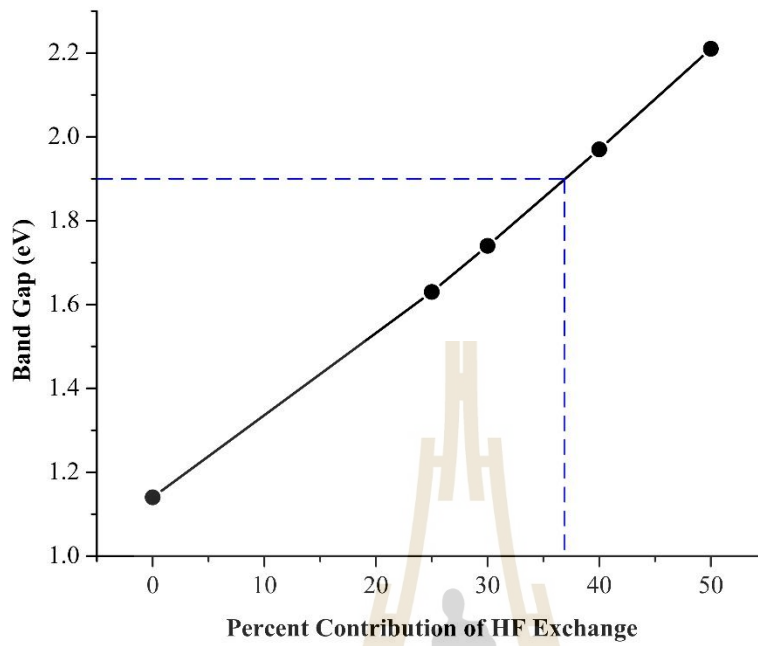
Figure 5.3 Calculated band gap values as a function of variation of Hatree-Fock (HF) contribution. The dashed blue lines indicate the point at which the exchange tuning theoretically reproduces the experimental band gap.
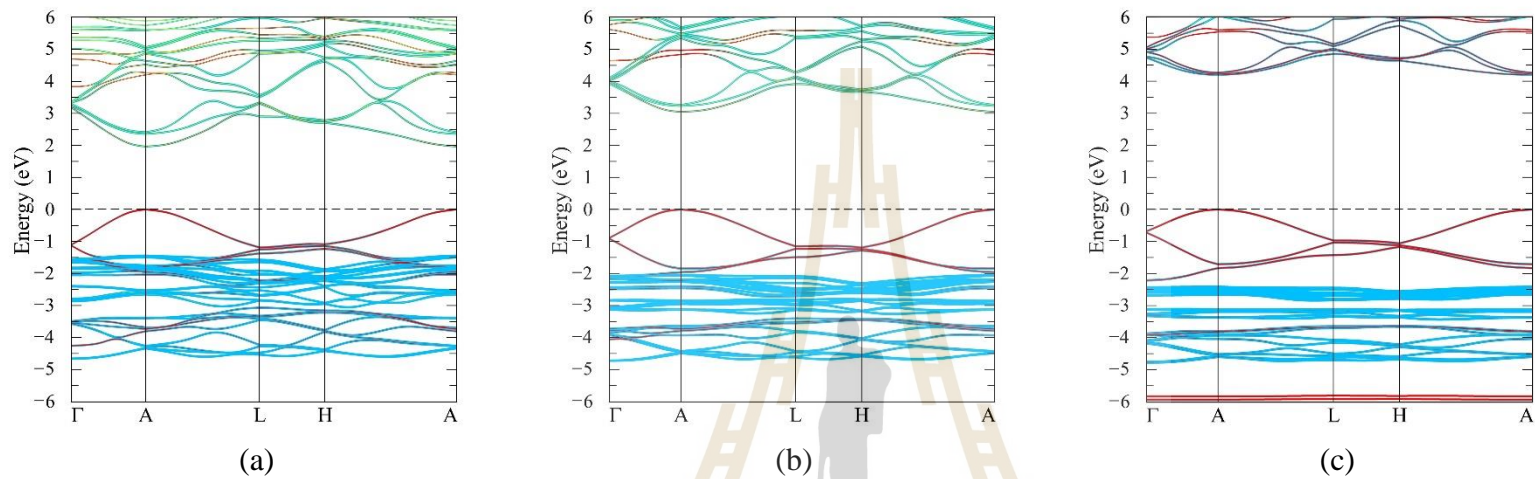
Figure 5.4 Band structure calculated by hybrid functional HSE06 without including SOC of (a) MAGeI$_3$, (b) MAGeBr$_3$, and (c) MAGeCl$_3$ halide perovskites in *R3m* crystal structure.
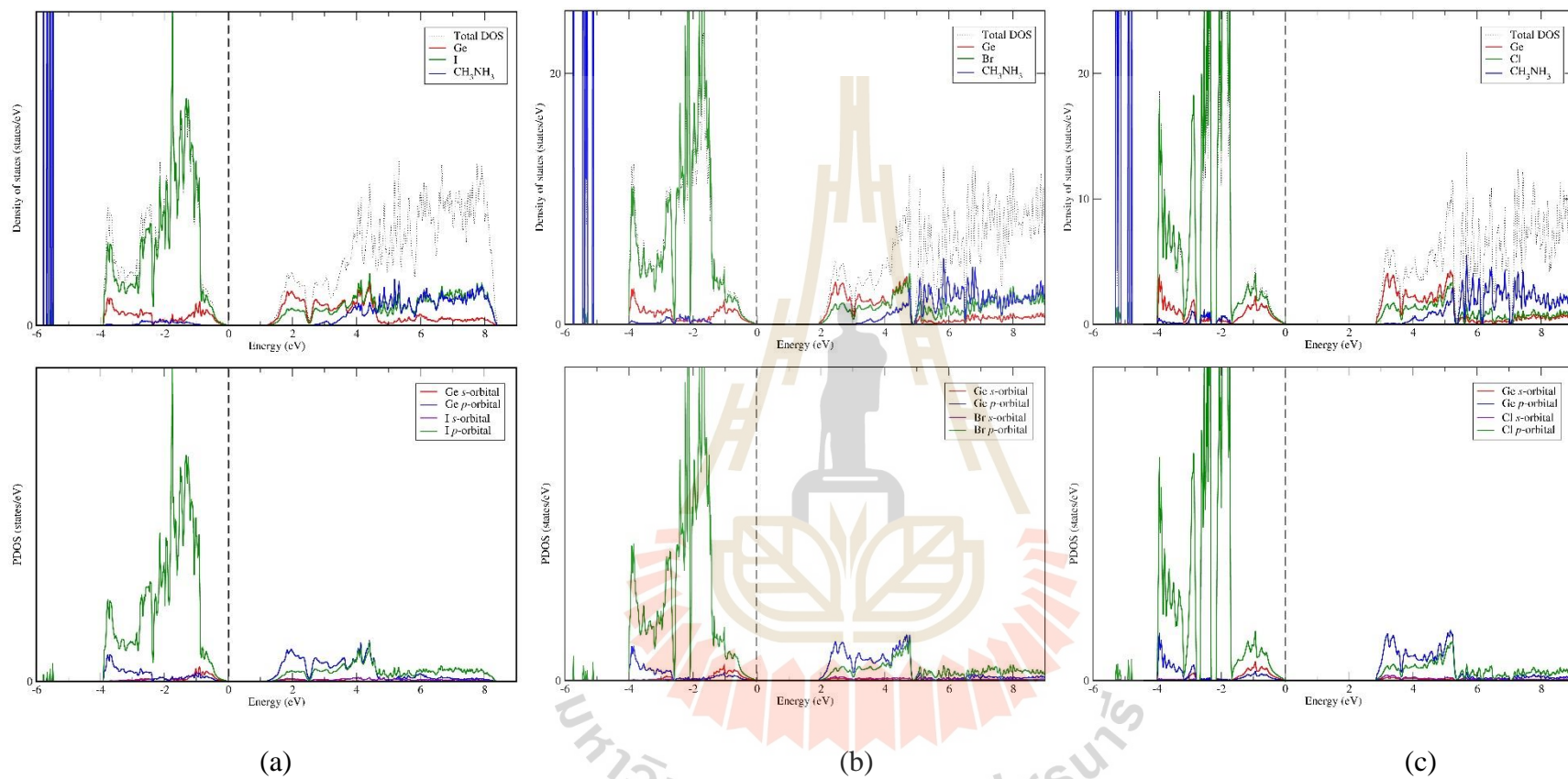
Figure 5.5 Calculated density of state (DOS) and partial density of states (PDOS) of (a) MAGeI$_3$, (b) MAGeBr$_3$, and (c) MAGeCl$_3$ halide perovskites in *R3m* crystal structure.
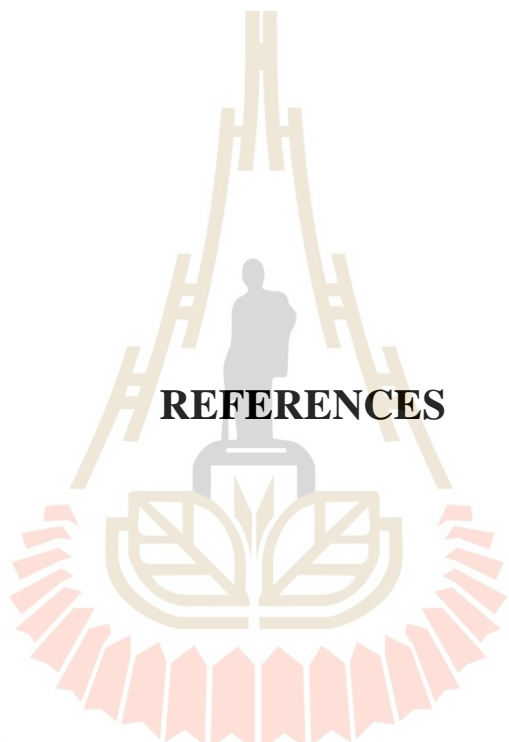
REFERENCES

REFERENCES

Adamo, C. and Barone, V. (1999). Toward reliable density functional methods without adjustable parameters: The PBE0 model. **The Journal of Chemical Physics.** 110(13): 6158-6170.

Ashcroft, N. W. and Mermin, N. D. (1976). Solid State Physics. **Saunders College, Philadelphia.** 116.

Bechtel, J. S., Seshadri, R. and Van der Ven, A. (2016). Energy Landscape of Molecular Motion in Cubic Methylammonium Lead Iodide from First-Principles. **The Journal of Physical Chemistry C.** 120(23): 12403-12410.

Bernal, C. and Yang, K. (2014). First-principles hybrid functional study of the organic-inorganic perovskites $CH_3NH_3SnBr_3$ and $CH_3NH_3SnI_3$. **The Journal of Physical Chemistry C.** 118: 24383–24388.

Birch, F. (1947). Finite Elastic Strain of Cubic Crystals. **Physical Review.** 71(11): 809-824.

Blöchl, P. E. (1994). Projector augmented-wave method. **Physical Review B.** 50(24): 17953-17979.

Born, M. and Oppenheimer, R. (1927). Zur Quantentheorie der Molekeln. **Annalen der Physik.** 389(20): 457-484.

Brivio, F., Butler, K. T., Walsh, A. and van Schilfgaarde, M. (2014). Relativistic quasiparticle self-consistent electronic structure of hybrid halide perovskite photovoltaic absorbers. **Physical Review B.** 89(15): 155204.

Burke, K., Perdew, J. P. and Ernzerhof, M. (1998). Why semilocal functionals work: Accuracy of the on-top pair density and importance of system averaging. **The Journal of Chemical Physics.** 109(10): 3760-3771.

Burschka, J., Pellet, N., Moon, S.-J., Humphry-Baker, R., Gao, P., Nazeeruddin, M. K. and Grätzel, M. (2013). Sequential deposition as a route to high-performance perovskite-sensitized solar cells. **Nature.** 499: 316.

Bylander, D. M., Kleinman, L. and Lee, S. (1990) Self-consistent calculations of the energy bands and bonding properties of $B_{12}C_3$. In **Physical Review B,** (Vol. 42, pp. 1394-1403)American Physical Society.

Carrasco, J., Klimeš, J. and Michaelides, A. (2013). The role of van der Waals forces in water adsorption on metals. **The Journal of Chemical Physics.** 138(2): 024708.

Carrasco, J., Liu, W., Michaelides, A. and Tkatchenko, A. (2014). Insight into the description of van der Waals forces for benzene adsorption on transition metal (111) surfaces. **The Journal of Chemical Physics.** 140(8): 084704.

Carrasco, J., Santra, B., Klimeš, J. and Michaelides, A. (2011). To Wet or Not to Wet? Dispersion Forces Tip the Balance for Water Ice on Metals. **Physical Review Letters.** 106(2): 026101.

Ceperley, D. M. and Alder, B. J. (1980). Ground State of the Electron Gas by a Stochastic Method. **Physical Review Letters.** 45(7): 566-569.

Cheng, J.-R., Zhu, W., Li, N. and Cross, L. E. (2003). Fabrication and characterization of $xBiGaO_3$–$(1−x)PbTiO_3$: a high temperature reduced Pb-content piezoelectric ceramic. **Materials Letters.** 57(13): 2090-2094.

Chiarella, F., Zappettini, A., Licci, F., Borriello, I., Cantele, G., Ninno, D., Cassinese, A. and Vaglio, R. (2008). Combined experimental and theoretical investigation of optical, structural, and electronic properties of $CH_3NH_3SnX_3$ thin films (X=Cl, Br). **Physical Review B.** 77(4): 045129.

Christian Wagner, Jörg Schuster and Gessner, h. (2012). DFT investigations of the piezoresistive effect of carbon nanotubes for sensor application. **physica status solidi (b).** 249(12): 2450-2453.

Chung, I., Lee, B., He, J., Chang, R. P. H. and Kanatzidis, M. G. (2012). All-solid-state dye-sensitized solar cells with high efficiency. **Nature.** 485: 486.

Chung, I., Song, J.-H., Im, J., Androulakis, J., Malliakas, C. D., Li, H., Freeman, A. J., Kenney, J. T. and Kanatzidis, M. G. (2012). $CsSnI_3$: Semiconductor or Metal? High Electrical Conductivity and Strong Near-Infrared Photoluminescence from a Single Material. High Hole Mobility and Phase-Transitions. **Journal of the American Chemical Society.** 134(20): 8579-8587.

Culbertson, C. M., Flak, A. T., Yatskin, M., Cheong, P. H. Y., Cann, D. P. and Dolgos, M. R. (2020). Neutron Total Scattering Studies of Group II Titanates ($ATiO_3$, A^{2+} = Mg, Ca, Sr, Ba). **Scientific Reports.** 10(1): 3729.

Davidson, E. R. (1983). Methods in Computational Moleular Physis edited by Dierksen, G. H. F. and Wilson. **New York: Plenum.**

De Graef, M. and McHenry, M. E. (2012). **Structure of Materials: An Introduction to Crystallography, Diffraction and Symmetry.** Cambridge: Cambridge University Press.

Dirac, P. A. M. (1930). Note on Exchange Phenomena in the Thomas Atom. **Mathematical Proceedings of the Cambridge Philosophical Society.** 26(3): 376-385.

Docampo, P., Ball, J. M., Darwich, M., Eperon, G. E. and Snaith, H. J. (2013). Efficient organometal trihalide perovskite planar-heterojunction solar cells on flexible polymer substrates. **Nature Communications.** 4: 2761.

Dreizler, R. M. and Gross, E. K. U. (1990). Density Functional Theory : An Approach to the Quantum Many-Body Problem. **Springer, Berlin.**

Egger, D. A. and Kronik, L. (2014). Role of Dispersive Interactions in Determining Structural Properties of Organic–Inorganic Halide Perovskites: Insights from First-Principles Calculations. **The Journal of Physical Chemistry Letters.** 5(15): 2728-2733.

Feng, J. and Xiao, B. (2014). Crystal Structures, Optical Properties, and Effective Mass Tensors of $CH_3NH_3PbX_3$ (X = I and Br) Phases Predicted from HSE06. **The Journal of Physical Chemistry Letters.** 5(7): 1278-1282.

Fermi, E. (1927). Un Metodo Statistico per la Determinazione di alcune Prioprietà dell'Atomo. Endiconti. **Accademia Nazionale dei Lincei.** 6: 602-607.

Fox, S. J., Dziedzic, J., Fox, T., Tautermann, C. S. and Skylaris, C.-K. (2014). Density functional theory calculations on entire proteins for free energies of binding: Application to a model polar binding site. **Proteins: Structure, Function, and Bioinformatics.** 82(12): 3335-3346.

Geerlings, P., De Proft, F. and Langenaeker, W. (2003). Conceptual Density Functional Theory. **Chemical Reviews.** 103(5): 1793-1874.

Gell-Mann, M. and Brueckner, K. A. (1957). Correlation Energy of an Electron Gas at High Density. **Physical Review.** 106(2): 364-368.

Goldschmidt, V. M. (1926). Die Gesetze der Krystallochemie. **Naturwissenschaften.** 14(21): 477-485.

Golub, G. and Ye, Q. (1999). Inexact Preconditioned Conjugate Gradient Method with Inner-Outer Iteration. **SIAM Journal on Scientific Computing.** 21(4): 1305-1320.

Graziano, G., Klimeš, J., Fernandez-Alonso, F. and Michaelides, A. (2012). Improved description of soft layered materials with van der Waals density functional theory. **Journal of Physics: Condensed Matter.** 24(42): 424216.

Grimme, S. (2004). Accurate description of van der Waals complexes by density functional theory including empirical corrections. **Journal of Computational Chemistry.** 25(12): 1463-1473.

Grimme, S. (2006). Semiempirical GGA-type density functional constructed with a long-range dispersion correction. **Journal of Computational Chemistry.** 27(15): 1787-1799.

Grimme, S., Antony, J., Ehrlich, S. and Krieg, H. (2010). A consistent and accurate ab initio parametrization of density functional dispersion correction (DFT-D) for the 94 elements H-Pu. **The Journal of Chemical Physics.** 132(15): 154104.

Grimme, S., Hansen, A., Brandenburg, J. G. and Bannwarth, C. (2016). Dispersion-Corrected Mean-Field Electronic Structure Methods. **Chemical Reviews.** 116(9): 5105-5154.

Gunnarsson, O., Jonson, M. and Lundqvist, B. I. (1976). Exchange and correlation in atoms, molecules and solids. **Physics Letters A.** 59(3): 177-179.

Gunnarsson, O. and Lundqvist, B. I. (1976). Exchange and correlation in atoms, molecules, and solids by the spin-density-functional formalism. **Physical Review B.** 13(10): 4274-4298.

Hamann, D. R., Schlüter, M. and Chiang, C. (1979). Norm-Conserving Pseudopotentials. **Physical Review Letters.** 43(20): 1494-1497.

Han, W., Zhu, J., Zhang, S., Zhang, H., Wang, X., Wang, Q., Gao, C. and Jin, C. (2013). Phase transitions in nanoparticles of $BaTiO_3$ as functions of temperature and pressure. **Journal of Applied Physics.** 113(19): 193513.

Hartree, D. R. (1928). The Wave Mechanics of an Atom with a Non-Coulomb Central Field. Part I. Theory and Methods. **Mathematical Proceedings of the Cambridge Philosophical Society.** 24(1): 89-110.

Hedin, L. (1965). New Method for Calculating the One-Particle Green's Function with Application to the Electron-Gas Problem. **Physical Review.** 139(3A): A796-A823.

Hedin, L. and Lundqvist, S. (1970) **Effects of Electron-Electron and Electron-Phonon Interactions on the One-Electron States of Solids.** In Solid State Physics, Vol. 23 (Eds, Seitz, F., Turnbull, D. and Ehrenreich, H.) Academic Press, pp. 1-181.

Heine, V. (1980) **Electronic Structure from the Point of View of the Local Atomic Environment.** In Solid State Physics, Vol. 35 (Eds, Ehrenreich, H., Seitz, F. and Turnbull, D.) Academic Press, pp. 1-127.

Hellmann, H. (1937). Einführung in die Quantumchemie. **Leipzig: Deütsche.**

Heyd, J., Scuseria, G. E. and Ernzerhof, M. (2003). Hybrid functionals based on a screened Coulomb potential. **The Journal of Chemical Physics.** 118(18): 8207-8215.

Hohenberg, P. and Kohn, W. (1964). Inhomogeneous Electron Gas. **Physical Review.** 136(3B): B864-B871.

Pashov D., Swagata A., Lambrecht W.R.L., Jackson J., Belashchenko K.D., Chantis A., Jamet F., Schilfgaarde M. V. (2019). *Questaal: a package of electronic structure methods based on the linear muffin-tin orbital technique.* Retrived from https://www.questaal.org.

Hu, M., Liu, L., Mei, A., Yang, Y., Liu, T. and Han, H. (2014). Efficient hole-conductor-free, fully printable mesoscopic perovskite solar cells with a broad light harvester $NH_2CHNH_2PbI_3$. **Journal of Materials Chemistry A.** 2(40): 17115-17121.

Huang, L.-y. and Lambrecht, W. R. L. (2013). Electronic band structure, phonons, and exciton binding energies of halide perovskites $CsSnCl_3$, $CsSnBr_3$, and $CsSnI_3$. **Physical Review B.** 88(16): 165203.

Huang, L.-y. and Lambrecht, W. R. L. (2014). Lattice dynamics in perovskite halides $CsSnX_3$ with X=I, Br, Cl. **Physical Review B.** 90(19): 195201.

Huang, L.-y. and Lambrecht, W. R. L. (2016). Electronic band structure trends of perovskite halides: Beyond Pb and Sn to Ge and Si. **Physical Review B.** 93(19): 195211.

Huang, L.-y. and Lambrecht, W. R. L. (2016). Vibrational spectra and nonlinear optical coefficients of rhombohedral $CsGeX_3$ halide compounds with X=I, Br, Cl. **Physical Review B.** 94(11): 115202.

Huang, Z., Wang, D., Wang, S. and Zhang, T. (2018). Highly Efficient and Stable MAPbI₃ Perovskite Solar Cell Induced by Regulated Nucleation and Ostwald Recrystallization. **Materials (Basel, Switzerland).** 11(5): 778.

Hutter, E. M., Gélvez-Rueda, M. C., Osherov, A., Bulović, V., Grozema, F. C., Stranks, S. D. and Savenije, T. J. (2017). Direct–indirect character of the bandgap in methylammonium lead iodide perovskite. **Nature Materials.** 16(1): 115-120.

Im, J.-H., Lee, C.-R., Lee, J.-W., Park, S.-W. and Park, N.-G. (2011). 6.5% efficient perovskite quantum-dot-sensitized solar cell. **Nanoscale.** 3(10): 4088-4093.

Johnson, D. D. (1988). Modified Broyden's method for accelerating convergence in self-consistent calculations. **Physical Review B.** 38(18): 12807-12813.

Jones, R. O. and Gunnarsson, O. (1989). The density functional formalism, its applications and prospects. **Reviews of Modern Physics.** 61(3): 689-746.

Jung, H. S. and Park, N.-G. (2015). Perovskite Solar Cells: From Materials to Devices. **Small.** 11(1): 10-25.

Kaloni, T. P., Cheng, Y. C. and Schwingenschlögl, U. (2012). Electronic structure of superlattices of graphene and hexagonal boron nitride. **Journal of Materials Chemistry.** 22(3): 919-922.

Kaloni, T. P., Schreckenbach, G. and Freund, M. S. (2014). Large Enhancement and Tunable Band Gap in Silicene by Small Organic Molecule Adsorption. **The Journal of Physical Chemistry C.** 118(40): 23361-23367.

Kaloni, T. P., Schreckenbach, G. and Freund, M. S. (2016). Band gap modulation in polythiophene and polypyrrole-based systems. **Scientific Reports.** 6: 36554.

Kieslich, G., Sun, S. and Cheetham, A. K. (2014). Solid-state principles applied to organic–inorganic perovskites: new tricks for an old dog. **Chemical Science.** 5(12): 4712-4715.

Kieslich, G., Sun, S. and Cheetham, A. K. (2015). An extended Tolerance Factor approach for organic–inorganic perovskites. **Chemical Science.** 6(6): 3430-3433.

Kim, H.-S., Lee, C.-R., Im, J.-H., Lee, K.-B., Moehl, T., Marchioro, A., Moon, S.-J., Humphry-Baker, R., Yum, J.-H., Moser, J. E., Grätzel, M. and Park, N.-G. (2012). Lead Iodide Perovskite Sensitized All-Solid-State Submicron Thin Film Mesoscopic Solar Cell with Efficiency Exceeding 9%. **Scientific Reports.** 2: 591.

Kim, K. and Jordan, K. D. (1994). Comparison of Density Functional and MP2 Calculations on the Water Monomer and Dimer. **The Journal of Physical Chemistry.** 98(40): 10089-10094.

King-Smith, R. D. and Vanderbilt, D. (1993). Theory of polarization of crystalline solids. **Physical Review B.** 47(3): 1651-1654.

Kittle, C. (1996). Introduction to Solid State Physics. **United State of America: Cambridge University. John Wiley & Sons, Inc.**

Kleinman, L. and Bylander, D. M. (1982). Efficacious Form for Model Pseudopotentials. **Physical Review Letters.** 48(20): 1425-1428.

Knop, O., Wasylishen, R. E., White, M. A., Cameron, T. S. and Oort, M. J. M. V. (1990). Alkylammonium lead halides. Part 2. $CH_3NH_3PbX_3$ (X=Cl, Br, I) perovskites: cuboctahedral halide cages with isotropic cation reorientation. **Canadian Journal of Chemistry.** 68(3): 412-422.

Kohn, W. (1999). Nobel Lecture: Electronic structure of matter---wave functions and density functionals. **Reviews of Modern Physics.** 71(5): 1253-1266.

Kohn, W. and Sham, L. J. (1965). Self-Consistent Equations Including Exchange and Correlation Effects. **Physical Review.** 140(4A): A1133-A1138.

Kojima, A., Teshima, K., Shirai, Y. and Miyasaka, T. (2009). Organometal Halide Perovskites as Visible-Light Sensitizers for Photovoltaic Cells. **Journal of the American Chemical Society.** 131(17): 6050-6051.

Kotani, T., van Schilfgaarde, M. and Faleev, S. V. (2007). Quasiparticle self-consistent GW method: A basis for the independent-particle approximation. **Physical Review B.** 76(16): 165106.

Kresse, G. and Furthmüller, J. (1996). Efficient iterative schemes for ab initio total-energy calculations using a plane-wave basis set. **Physical Review B.** 54(16): 11169-11186.

Kresse, G. and Furthmüller, J. (1996a). Efficiency of ab-initio total energy calculations for metals and semiconductors using a plane-wave basis set. **Computational Materials Science.** 6(1): 15-50.

Kresse, G. and Furthmüller, J. (1996b). Efficient iterative schemes for ab initio total-energy calculations using a plane-wave basis set. **Physical Review B.** 54(16): 11169-11186.

Kresse, G. and Furthmüller, J. (2012). Vienna ab-initio simulation package: VASP the GUIDE. . **Wien: Institut fur Materialphysik, Universitat Wien.**

Kresse, G. and Hafner, J. (1994). Norm-conserving and ultrasoft pseudopotentials for first-row and transition elements. **Journal of Physics: Condensed Matter.** 6(40): 8245-8257.

Kresse, G. and Joubert, D. (1999). From ultrasoft pseudopotentials to the projector augmented-wave method. **Physical Review B.** 59(3): 1758-1775.

Ksepko, E. and Ratuszna, A. (2018). Crystal structure and temperature dependent structural phase transitions in $(Ba_{1-x}Sr_x)PbO_3$ (x = 0, 0.2, 0.6) perovskite ceramics. **Ceramics International.** 44(15): 18294-18302.

Lan, R., Cowin, P. I., Sengodan, S. and Tao, S. (2016). A perovskite oxide with high conductivities in both air and reducing atmosphere for use as electrode for solid oxide fuel cells. **Scientific Reports.** 6: 31839.

Lee, J.-H., Bristowe, N. C., Bristowe, P. D. and Cheetham, A. K. (2015). Role of hydrogen-bonding and its interplay with octahedral tilting in CH3NH3PbI3. **Chemical Communications.** 51(29): 6434-6437.

Lee, M. M., Teuscher, J., Miyasaka, T., Murakami, T. N. and Snaith, H. J. (2012). Efficient Hybrid Solar Cells Based on Meso-Superstructured Organometal Halide Perovskites. **Science.** 338(6107): 643.

Lee, S., Patton, P. and Radermacher, W. (2002) A successful DFT tester: what will it look like? Is DFT tester a logical next step in ATE evolution? In **Proceedings 20th IEEE VLSI Test Symposium (VTS 2002),** (pp. 129-129).

Li, C., Lu, X., Ding, W., Feng, L., Gao, Y. and Guo, Z. (2008). Formability of ABX_3 (X = F, Cl, Br, I) halide perovskites. **Acta Crystallographica Section B.** 64(6): 702-707.

Li, J. and Rinke, P. (2016). Atomic structure of metal-halide perovskites from first principles: The chicken-and-egg paradox of the organic-inorganic interaction. **Physical Review B.** 94(4): 045201.

Liu, J., Xue, Y., Wang, Z., Xu, Z.-Q., Zheng, C., Weber, B., Song, J., Wang, Y., Lu, Y., Zhang, Y. and Bao, Q. (2016). Two-Dimensional $CH_3NH_3PbI_3$ Perovskite: Synthesis and Optoelectronic Application. **ACS Nano.** 10(3): 3536-3542.

Liu, Z.-J., Zhang, C.-R., Sun, X.-W., Wang, L. U., Song, T. and Qi, J.-H. (2011). Structural, electronic and optical properties of the tetragonal phase of $CaSiO_3$ perovskite under pressure: first-principles calculations. **Modern Physics Letters B.** 25(01): 41-52.

Lu, J., Luo, W., Feng, J. and Xiang, H. (2018). Unusual Ferroelectricity in Two-Dimensional Perovskite Oxide Thin Films. **Nano Letters.** 18(1): 595-601.

Lu, X., Zhao, Z., Li, K., Han, Z., Wei, S., Guo, C., Zhou, S., Wu, Z., Guo, W. and Wu, C.-m. L. (2016). First-principles insight into the photoelectronic properties of Ge-based perovskites. **RSC Advances.** 6(90): 86976-86981.

Marom, N., Bernstein, J., Garel, J., Tkatchenko, A., Joselevich, E., Kronik, L. and Hod, O. (2010). Stacking and Registry Effects in Layered Materials: The Case of Hexagonal Boron Nitride. **Physical Review Letters.** 105(4): 046801.

Martin, R. M. (2004). Electronic Structure: Basic Theory and Practical Methods. **United Kingdom: Cambridge University Press.**

Martin, R. M. (2004) **Theoretical background.** In Electronic Structure: Basic Theory and Practical Methods(Ed), Martin, R. M.) Cambridge University Press, Cambridge, pp. 52-72.

Methfessel, M., Rodriguez, C. O. and Andersen, O. K. (1989). Fast full-potential calculations with a converged basis of atom-centered linear muffin-tin orbitals: Structural and dynamic properties of silicon. **Physical Review B.** 40(3): 2009-2012.

Methfessel, M., van Schilfgaarde, M. and Casali, R. (2000). A full-potential LMTO method based on smooth Hankel functions. **Electronic Structure and Physical Properties of Solids: the Uses of the LMTO Method.** edited by H. Dreysse, lecture notes in physics.: 535.

Methfessel, M., van Schilfgaarde, M. and Casali, R. A. (2000) A Full-Potential LMTO Method Based on Smooth Hankel Functions. In **Electronic Structure and Physical Properies of Solids,** (pp. 114-147)(Ed), Dreyssé, H.) Springer Berlin Heidelberg, Berlin, Heidelberg.

Meyer, B. (2006). The pseudo plane wave approach. **John von Neumann Institute for Computing.** 31: 71.

Monkhorst, H. J. and Pack, J. D. (1976). Special points for Brillouin-zone integrations. **Physical Review B.** 13(12): 5188-5192.

Mosconi, E., Amat, A., Nazeeruddin, M. K., Grätzel, M. and De Angelis, F. (2013). First-Principles Modeling of Mixed Halide Organometal Perovskites for Photovoltaic Applications. **The Journal of Physical Chemistry C.** 117(27): 13902-13913.

Motta, C., El-Mellouhi, F., Kais, S., Tabet, N., Alharbi, F. and Sanvito, S. (2015). Revealing the role of organic cations in hybrid halide perovskite CH3NH3PbI3. **Nature Communications.** 6: 7026.

Murnaghan, F. D. (1944). The Compressibility of Media under Extreme Pressures. **Proceedings of the National Academy of Sciences.** 30(9): 244-247.

National Renewable Energy Laboratory, N. (2016). Research cell efficiency records.

O'Regan, B. and Grätzel, M. (1991). A low-cost, high-efficiency solar cell based on dye-sensitized colloidal TiO_2 films. **Nature.** 353(6346): 737-740.

Pandech, N., Sarasamak, K. and Limpijumnong, S. (2013). Sound velocities and elastic properties of $PbTiO_3$ and $PbZrO_3$ under pressure: First principles study. **Ceramics International.** 39: S277-S281.

Pandech, N., Sarasamak, K. and Limpijumnong, S. (2015). Elastic properties of perovskite ATiO$_3$ (A = Be, Mg, Ca, Sr, and Ba) and PbBO$_3$ (B = Ti, Zr, and Hf): First principles calculations. **Journal of Applied Physics.** 117(17): 174108.

Pandech, N., Sarasamak, K. and Limpijumnong, S. (2016). First Principles Calculations of Structural and Elastic Properties of Perovskite Crystals: The Case of $SrTiO_3$. **Journal of the Chinese Chemical Society.** 63(6): 521-525.

Park, J.-S., Choi, S., Yan, Y., Yang, Y., Luther, J. M., Wei, S.-H., Parilla, P. and Zhu, K. (2015). Electronic Structure and Optical Properties of α-$CH_3NH_3PbBr_3$ Perovskite Single Crystal. **The Journal of Physical Chemistry Letters.** 6(21): 4304-4308.

Parr, R. G. (1983). Density Functional Theory. **Annual Review of Physical Chemistry.** 34(1): 631-656.

Parr, R. G. and Yang, W. (1989). Density-Functional theory of atoms and molecules. **The United States of America: Oxford University Press.**

Pauling, L. (1929). The Principles Determining the Structure of Complex Ionic Crystals. **Journal of the American Chemical Society.** 51(4): 1010-1026.

Perdew, J. P., Burke, K. and Ernzerhof, M. (1996). Generalized Gradient Approximation Made Simple. **Physical Review Letters.** 77(18): 3865-3868.

Perdew, J. P. and Wang, Y. (1992). Accurate and simple analytic representation of the electron-gas correlation energy. **Physical Review B.** 45(23): 13244-13249.

Perdew, J. P. and Zunger, A. (1981). Self-interaction correction to density-functional approximations for many-electron systems. **Physical Review B.** 23(10): 5048-5079.

Pérez-Tomas, A., Xie, H., Wang, Z., Kim, H.-S., Shirley, I., Turren-Cruz, S.-H., Morales-Melgares, A., Saliba, B., Tanenbaum, D., Saliba, M., Zakeeruddin, S. M., Gratzel, M., Hagfeldt, A. and Lira-Cantu, M. (2019). PbZrTiO$_3$ ferroelectric oxide as an electron extraction material for stable halide perovskite solar cells. **Sustainable Energy & Fuels.** 3(2): 382-389.

Poglitsch, A. and Weber, D. (1987). Dynamic disorder in methylammoniumtrihalogenoplumbates (II) observed by millimeter-wave spectroscopy. **The Journal of Chemical Physics.** 87(11): 6373-6378.

Polman, A., Knight, M., Garnett, E. C., Ehrler, B. and Sinke, W. C. (2016). Photovoltaic materials: Present efficiencies and future challenges. **Science.** 352(6283): aad4424.

Pulay, P. (1980). Convergence acceleration of iterative sequences. the case of scf iteration. **Chemical Physics Letters.** 73(2): 393-398.

Quarti, C., Mosconi, E. and De Angelis, F. (2014). Interplay of Orientational Order and Electronic Structure in Methylammonium Lead Iodide: Implications for Solar Cell Operation. **Chemistry of Materials.** 26(22): 6557-6569.

Radha, S. K., Bhandari, C. and Lambrecht, W. R. L. (2018). Distortion modes in halide perovskites: To twist or to stretch, a matter of tolerance and lone pairs. **Physical Review Materials.** 2(6): 063605.

Ravel, B., Stern, E. A., Vedrinskii, R. I. and Kraizman, V. (1998). Local structure and the phase transitions of BaTiO$_3$. **Ferroelectrics.** 206(1): 407-430.

Resta, R. (1992). Theory of the electric polarization in crystals. **Ferroelectrics.** 136(1): 51-55.

Resta, R. (1994). Macroscopic polarization in crystalline dielectrics: the geometric phase approach. **Reviews of Modern Physics.** 66(3): 899-915.

Sahoo, S. K., Manoharan, B. and Sivakumar, N. (2018) **Chapter 1 - Introduction: Why Perovskite and Perovskite Solar Cells?** In Perovskite Photovoltaics(Eds, Thomas, S. and Thankappan, A.) Academic Press, pp. 1-24.

Scott, J. F., Palai, R., Kumar, A., Singh, M. K., Murari, N. M., Karan, N. K. and Katiyar, R. S. (2008). New Phase Transitions in Perovskite Oxides: $BiFeO_3$, $SrSnO_3$, and $Pb(Fe_{2/3}W_{1/3})_{1/2}Ti_{1/2}O_3$. **Journal of the American Ceramic Society.** 91(6): 1762-1768.

Shannon, R. (1976). Revised effective ionic radii and systematic studies of interatomic distances in halides and chalcogenides. **Acta Crystallographica Section A.** 32(5): 751-767.

Shi, Z. and Jayatissa, A. H. (2018). Perovskites-Based Solar Cells: A Review of Recent Progress, Materials and Processing Methods. **Materials (Basel, Switzerland).** 11(5): 729.

Snyder, G. J., Badding, M. E. and DiSalvo, F. J. (1992). Synthesis, structure, and properties of barium cobalt sulfide ($Ba_6Co_{25}S_{27}$) a perovskite-like superstructure of Co_8S_6 and Ba_6S clusters. **Inorganic Chemistry.** 31(11): 2107-2110.

Spaldin, N. A. (2012). A beginner's guide to the modern theory of polarization. **Journal of Solid State Chemistry.** 195: 2-10.

Stephens, P. J., Devlin, F. J., Chabalowski, C. F. and Frisch, M. J. (1994). Ab Initio Calculation of Vibrational Absorption and Circular Dichroism Spectra Using

Density Functional Force Fields. **The Journal of Physical Chemistry.** 98(45): 11623-11627.

Stoumpos, C. C., Frazer, L., Clark, D. J., Kim, Y. S., Rhim, S. H., Freeman, A. J., Ketterson, J. B., Jang, J. I. and Kanatzidis, M. G. (2015). Hybrid Germanium Iodide Perovskite Semiconductors: Active Lone Pairs, Structural Distortions, Direct and Indirect Energy Gaps, and Strong Nonlinear Optical Properties. **Journal of the American Chemical Society.** 137(21): 6804-6819.

Stoumpos, C. C., Malliakas, C. D. and Kanatzidis, M. G. (2013). Semiconducting Tin and Lead Iodide Perovskites with Organic Cations: Phase Transitions, High Mobilities, and Near-Infrared Photoluminescent Properties. **Inorganic Chemistry.** 52(15): 9019-9038.

Sun, P.-P., Li, Q.-S., Yang, L.-N. and Li, Z.-S. (2016). Theoretical insights into a potential lead-free hybrid perovskite: substituting Pb2+ with Ge2+. **Nanoscale.** 8(3): 1503-1512.

Tang, C. W. (1986). Two-layer organic photovoltaic cell. **Applied Physics Letters.** 48(2): 183-185.

Tao, Canales-Vázquez, J. and Irvine, J. T. S. (2004). Structural and Electrical Properties of the Perovskite Oxide Sr_2FeNbO_6. **Chemistry of Materials.** 16(11): 2309-2316.

Tao, S. and Irvine, J. T. S. (2006). Phase Transition in Perovskite Oxide $La_{0.75}Sr_{0.25}Cr_{0.5}Mn_{0.5}O_3$-$\delta$ Observed by in Situ High-Temperature Neutron Powder Diffraction. **Chemistry of Materials.** 18(23): 5453-5460.

Tariq, S., Ahmed, A., Saad, S. and Tariq, S. (2015). Structural, electronic and elastic properties of the cubic CaTiO$_3$ under pressure: A DFT study. **AIP Advances.** 5(7): 077111.

Teter, M. P., Payne, M. C. and Allan, D. C. (1989). Solution of Schrodinger's equation for large systems. **Physical Review B.** 40(18): 12255-12263.

Thomas, L. H. (1927). The calculation of atomic fields. **Mathematical Proceedings of the Cambridge Philosophical Society.** 23(5): 542-548.

Tkatchenko, A., Alfè, D. and Kim, K. S. (2012). First-Principles Modeling of Non-Covalent Interactions in Supramolecular Systems: The Role of Many-Body Effects. **Journal of Chemical Theory and Computation.** 8(11): 4317-4322.

Tonui, P., Oseni, S. O., Sharma, G., Yan, Q. and Tessema Mola, G. (2018). Perovskites photovoltaic solar cells: An overview of current status. **Renewable and Sustainable Energy Reviews, Elsevier.** 91: 1025-1044.

Travis, W., Glover, E. N. K., Bronstein, H., Scanlon, D. O. and Palgrave, R. G. (2016). On the application of the tolerance factor to inorganic and hybrid halide perovskites: a revised system. **Chemical Science.** 7(7): 4548-4556.

Trifiletti, V., Roiati, V., Colella, S., Giannuzzi, R., De Marco, L., Rizzo, A., Manca, M., Listorti, A. and Gigli, G. (2015). NiO/MAPbI$_{3-x}$Cl$_x$/PCBM: A Model Case for an Improved Understanding of Inverted Mesoscopic Solar Cells. **ACS Applied Materials & Interfaces.** 7(7): 4283-4289.

Umari, P., Mosconi, E. and De Angelis, F. (2014). Relativistic GW calculations on CH$_3$NH$_3$PbI$_3$ and CH$_3$NH$_3$SnI$_3$ Perovskites for Solar Cell Applications. **Scientific Reports.** 4: 4467.

van Schilfgaarde, M., Kotani, T. and Faleev, S. (2006). Quasiparticle Self-Consistent GW Theory. **Physical Review Letters.** 96(22): 226402.

Vanderbilt, D. (1990). Soft self-consistent pseudopotentials in a generalized eigenvalue formalism. **Physical Review B.** 41(11): 7892-7895.

Vosko, S. H., Wilk, L. and Nusair, M. (1980). Accurate spin-dependent electron liquid correlation energies for local spin density calculations: a critical analysis. **Canadian Journal of Physics.** 58(8): 1200-1211.

Weber, D. (1978). $CH_3NH_3PbX_3$, ein Pb(II)-System mit kubischer Perowskitstruktur / $CH_3NH_3PbX_3$, a Pb(II)-System with Cubic Perovskite Structure. . **Zeitschrift für Naturforschung B.** 33: 1443-1445.

Weller, M. T., Weber, O. J., Henry, P. F., Di Pumpo, A. M. and Hansen, T. C. (2015). Complete structure and cation orientation in the perovskite photovoltaic methylammonium lead iodide between 100 and 352 K. **Chemical Communications.** 51(20): 4180-4183.

Whitfield, P. S., Herron, N., Guise, W. E., Page, K., Cheng, Y. Q., Milas, I. and Crawford, M. K. (2016). Structures, Phase Transitions and Tricritical Behavior of the Hybrid Perovskite Methyl Ammonium Lead Iodide. **Scientific Reports.** 6: 35685.

Xu, Q., Eguchi, T., Nakayama, H., Nakamura, N. and Kishita, M. (1991) Molecular Motions and Phase Transitions in Solid $CH_3NH_3PbX_3$ (X = C1, Br, I) as Studied by NMR and NQR. In **Zeitschrift für Naturforschung A,** (Vol. 46, pp. 240).

Xu, Q., Stroppa, A., Lv, J., Zhao, X., Yang, D., Biswas, K. and Zhang, L. (2019). Impact of organic molecule rotation on the optoelectronic properties of hybrid halide perovskites. **Physical Review Materials.** 3(12): 125401.

Yang, W. S., Noh, J. H., Jeon, N. J., Kim, Y. C., Ryu, S., Seo, J. and Seok, S. I. (2015). High-performance photovoltaic perovskite layers fabricated through intramolecular exchange. **Science.** 348(6240): 1234.

Yin, W.-J., Shi, T. and Yan, Y. (2014). Unusual defect physics in $CH_3NH_3PbI_3$ perovskite solar cell absorber. **Applied Physics Letters.** 104(6): 063903.

Yoshiasa, A., Nakatani, T., Nakatsuka, A., Okube, M., Sugiyama, K. and Mashimo, T. (2016). High-temperature single-crystal X-ray diffraction study of tetragonal and cubic perovskite-type $PbTiO_3$ phases. **Acta Crystallographica Section B.** 72(3): 381-388.

Yu, G., Gao, J., Hummelen, J. C., Wudl, F. and Heeger, A. J. (1995). Polymer Photovoltaic Cells: Enhanced Efficiencies via a Network of Internal Donor-Acceptor Heterojunctions. **Science.** 270(5243): 1789.

Yuan, Y., Xu, R., Xu, H.-T., Hong, F., Xu, F. and Wang, L.-J. (2015). Nature of the band gap of halide perovskites ABX_3 (A = CH_3NH_3 , Cs; B = Sn, Pb; X = Cl, Br, I): First-principles calculations. **Chinese Physics B.** 24(11): 116302.

Zhang, L. Q., Zhang, X. W., Yin, Z. G., Jiang, Q., Liu, X., Meng, J. H., Zhao, Y. J. and Wang, H. L. (2015). Highly efficient and stable planar heterojunction perovskite solar cells via a low temperature solution process. **Journal of Materials Chemistry A.** 3(23): 12133-12138.

Zhou, H., Chen, Q., Li, G., Luo, S., Song, T.-b., Duan, H.-S., Hong, Z., You, J., Liu, Y. and Yang, Y. (2014). Interface engineering of highly efficient perovskite solar cells. **Science.** 345(6196): 542.

Ziegler, T. (1991). Approximate density functional theory as a practical tool in molecular energetics and dynamics. **Chemical Reviews.** 91(5): 651-667.

Ziegler, T., Rauk, A. and Baerends, E. J. (1977). On the calculation of multiplet energies by the hartree-fock-slater method. **Theoretica chimica acta.** 43(3): 261-271.
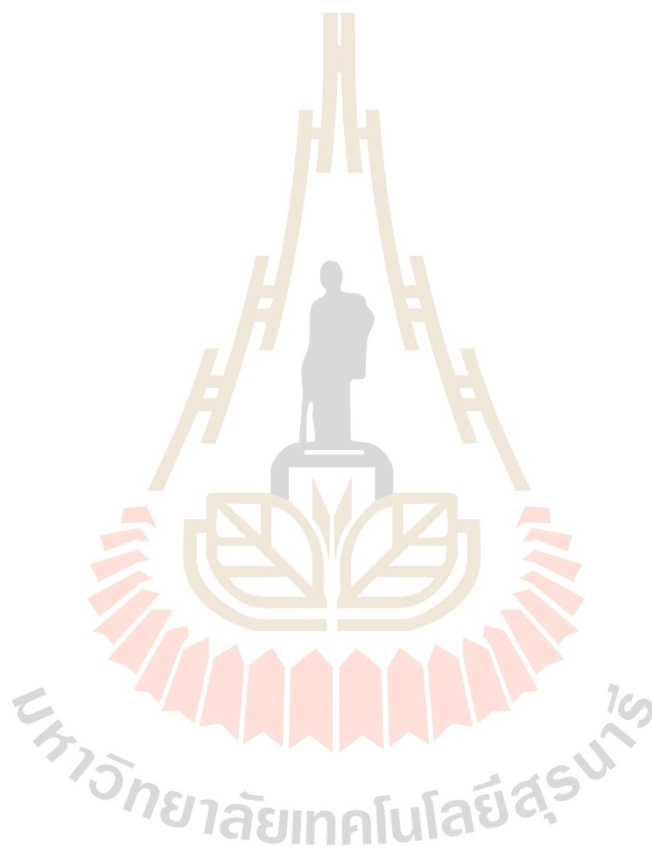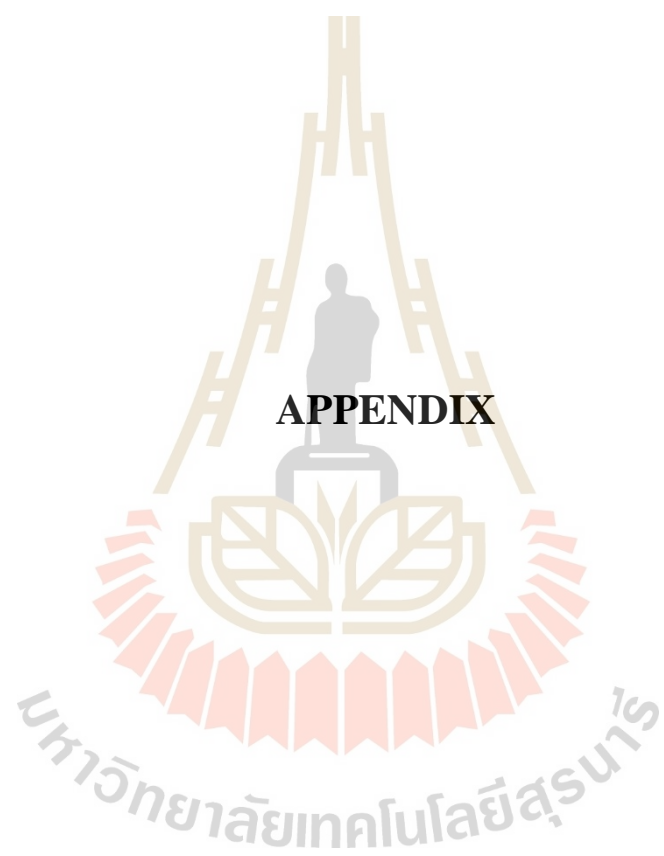
APPENDIX

APPENDIX

PUBLICATIONS AND PRESENTATIONS

1.   List of publications

Pandech, N., Sarasamak, K. and Limpijumnong, S. (2013). Sound velocities and elastic properties of $PbTiO_3$ and $PbZrO_3$ under pressure: First principles study. **Ceramics International** 39, Supplement 1: S277.

Pandech, N., Sarasamak, K. and Limpijumnong, S.(2015). Elastic properties of perovskite $ATiO_3$ (A = Be, Mg, Ca, Sr, and Ba) and $PbBO_3$ (B = Ti, Zr, and Hf): First principles calculations. **Journal of Applied Physics** 117. 174108.

Pandech, N., Sarasamak, K. and Limpijumnong, S. (2016). First Principles Calculations of Structural and Elastic Properties of Perovskite Crystals: The Case of $SrTiO_3$. **Journal of the Chinese Chemical Society** 63 521-525.

Schwertfager N., Pandech N., Suewattana M., T-thienprasert T and Limpijumnong S. (2016) Calculated XANES Spectra of Cation Off-Centering in $Bi(Mg_{0.5}Ti_{0.5})O_3$, **Ferroelectrics**, 490:1, 159-166.

Pandech, N., Kongnok, T., Palakawong, N., Limpijumnong, S., Lambrecht, W.R.L. and Jungthawan, S. (2020). Effects of the van der Waals Interactions on Structural and Electronic Properties of $CH_3NH_3(Pb,Sn)(I,Br,Cl)_3$ Halide Perovskites. **ACS Omega** 5, 40, 25723-25732.

2.   List of oral presentations

 Narasak Pandech, Thanundon Kongnok, Sukit Limpijumnong, Walter Lambrecht (March 2018) First-principles Investigation of The Role of Organic Molecules Inside The α-phase of Hybrid Halide Perovskite $CH_3NH_3BX_3$ (B= Pb, Sn; X= I, Br, Cl) In **American Physical Society Meeting (APS March Meeting 2018)** Los Angeles, California.

 Narasak Pandech, Thanundon Kongnok, Sukit Limpijumnong, Walter Lambrecht (August 2018). First-principles study on structural and electronic properties of Ge-based hybrid perovskites. In **International Union of Materials Research Society – International Conference on Electronic Materials 2018 (IUMRS-ICEM 2018).** Daejeon Convention Center in Daejeon, Korea.

3.   List of poster presentations

 Narasak Pandech, Thanundon Kongnok, Sukit Limpijumnong, Walter Lambrecht (November 2018). First-principles study on structural and electronic properties of hybrid perovskites. (MA = $CH_3NH_3^+$; B = Pb, Sn, Ge; X = I, Br, Cl) In **The 9th International Conference on Multiscale Materials Modeling (MMM 2018).** Osaka, Japan.

 Narasak Pandech, Thanundon Kongnok, Sukit Limpijumnong, Walter Lambrecht (November 2019). First-principles study on structural and electronic properties of Ge-based hybrid perovskites. In **The ICTP Asian Network School and Workshop on Complex Condensed Matter System 2019**. Samahang Pisika ng Pilipinas, Philippines.

Manuscript published in Journal of Applied Physics

Elastic properties of perovskite ATiO$_3$ (A = Be, Mg, Ca, Sr, and Ba) and PbBO$_3$ (B = Ti, Zr, and Hf): First principles calculations

Narasak Pandech,[1,2,3] Kanoknan Sarasamak,[4] and Sukit Limpijumnong[1,2,3,a]

[1]School of Physics and NANOTEC-SUT Center of Excellence on Advanced Functional Nanomaterials, Suranaree University of Technology, Nakhon Ratchasima 30000, Thailand
[2]Synchrotron Light Research Institute, Nakhon Ratchasima 30000, Thailand
[3]Thailand Center of Excellence in Physics (ThEP Center), Commission on Higher Education, Bangkok 10400, Thailand
[4]College of Nanotechnology, King Mongkut's Institute of Technology Ladkrabang, Bangkok 10520, Thailand

The mechanical properties of perovskite oxides depend on two metal oxide lattices that are intercalated. This provides an opportunity for separate tuning of hardness, Poisson's ratio (transverse expansion in response to the compression), and shear strength. The elastic constants of series of perovskite oxides were studied by first principles approach. Both A-site and B-site cations were systematically varied in order to see their effects on the elastic parameters. To study the effects of A-site cations, we studied the elastic properties of perovskite ATiO$_3$ for A being Be, Mg, Ca, Sr, or Ba, one at a time. Similarly, for B-site cations, we studied the elastic properties of PbBO$_3$ for B being Ti, Zr, or Hf, one at a time. The density functional first principles calculations with local density approximation (LDA) and generalized gradient approximation (GGA) were employed. It is found that the maximum C_{11} elastic constant is achieved when the atomic size of the cations at A-site and B-site are comparable. We also found that C_{12} elastic constant is sensitive to B-site cations while C_{44} elastic constant is more sensitive to A-site cations. Details and explanations for such dependencies are discussed. © 2015 AIP Publishing LLC. [http://dx.doi.org/10.1063/1.4919837]

I. INTRODUCTION

The elastic properties of materials provide detailed information on their mechanical properties. Because the elastic properties can be used to describe and predict the mechanical behaviors of materials in different situations, they have been studied both theoretically and experimentally for various classes of materials, including ABO_3-type perovskite crystals. It is known that first principles calculations can be reliably used to study these mechanical properties. Our research group has previously employed first principles calculations to study the elastic properties of IV-IV, III-V, and II-V semiconductors and obtained results[1–3] that are in good agreement with experimental values.

For perovskite oxides, there are several literatures on the calculations of elastic properties of ABO_3-type perovskite crystals; following are some examples. Wang and co-workers[4] used density functional theory (DFT) to study several properties of perovskite BaTiO$_3$, including the elastic properties. In their works, the elastic constants of four different crystal structures (cubic, tetragonal, orthorhombic, and rhombohedral) of BaTiO$_3$ have been reported. Meng and co-workers[5] also used DFT to study the elastic and piezoelectric properties of BaTiO$_3$ in the tetragonal structure. Liu and co-workers[6] used DFT to study the elastic properties of perovskite PbTiO$_3$ in both cubic and tetragonal structures. They reported the calculated elastic constants of both structures as well as the equilibrium tetragonal-to-cubic phase transition pressure. The elastic properties of natural cubic perovskite SrTiO$_3$ have

been studied by Boudali and co-workers.[7] They used DFT to calculate its elastic constants. The elastic properties of less-known perovskite materials, SnTiO$_3$, have also been calculated based on DFT by Taib and co-workers.[8] Their results showed the elastic properties of SnTiO$_3$ in the cubic perovskite phase.

On the experimental side, several perovskite oxides have also been studied. Li and co-workers[9] used the Brillouin scattering and ultrasound techniques to measure the velocity of the ultrasound in a single tetragonal BaTiO$_3$ crystal. The sound velocities can be used to calculate the elastic and piezoelectric constants. SrTiO$_3$ has also been widely studied using different techniques.[10–12] For example, Lheureux and co-worker[10] used the ultrasonic measurement technique to study the elastic constants and their pressure dependence of cubic SrTiO$_3$. Works on SrTiO$_3$ is quite extensive, because it has a simple crystal structure (cubic phase at room temperature) and high quality crystals are available.

Although the elastic properties of some ABO_3 perovskite materials have been previously studied, the trend of how the elastic constants depend on the cation species has not been investigated. This work reports such trend by systematically varying A-site and B-site cations and calculating their elastic properties. In our work, the B-site is fixed to be Ti when we vary the A-site among different Group II elements and the A-site is fixed to be Pb when we vary the B-site among different Group IV transition elements. Note that these choices of compounds are based partly on their technologically important and partly on past experience of the research team. There are also other interesting sets of compounds such as SrBO_3 and BaBO_3 that are worth investigation in the future.

a)Author to whom correspondence should be addressed. Electronic mail: sukit@sut.ac.th

Manuscript publised in Journal of Applied Physics
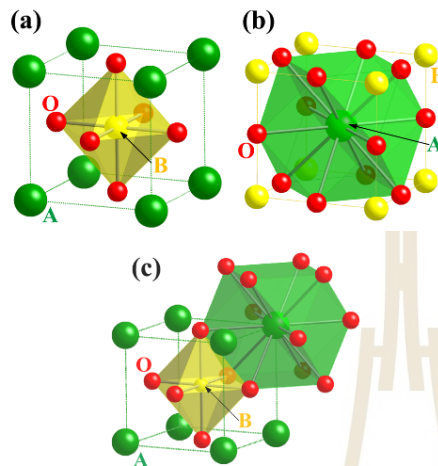
FIG. 1. Illustration of the ideal cubic perovskite crystal: (a) the six-atom oxygen cage surrounding the B cation, (b) the twelve-atom oxygen cage surrounding the A cation, and (c) both types of oxygen cages. The large green spheres represent A cations, medium-size yellow spheres are B cation, and small red spheres are oxygen anions.

II. COMPUTATIONAL METHOD

The computational approach employed is based on first principles density functional theory (DFT)[13,14] with the plane wave pseudo-potential method as implemented in Vienna *Ab-initio* Simulation Package (VASP).[15] Both local density approximation (LDA)[16,17] and generalized gradient approximation (GGA)[18] were used for the exchange-correlation terms. The ultrasoft version of the pseudo-potential implemented in the VASP code allows a low cut off energy for the plane wave expansion of only 500 eV. We used a $8 \times 8 \times 8$ Monkhrost-Pack scheme[19] for k-point sampling integrations.

Although the natural phases of some compounds contain symmetry lowering distortions, for, e.g., orthorhombic and tetragonal perovskite phases, for simplicity and systematic comparison, the ideal cubic structure (space group $Pm\bar{3}m$) as illustrated in Fig. 1 with the atomistic positions following Wychoff positions as tabulated in Table I were used to study all selected perovskite oxides in this work. For the cubic crystal systems, there are only three independent elastic constants (C_{11}, C_{12}, and C_{44}).[20] The longitudinal distortion, C_{11}, is based on the longitudinal compression, describing the hardness. The transverse distortion, C_{12}, is based on the transverse expansion; related to the Poisson's ratio. The shear elastic parameter, C_{44}, is based on the shear modulus.[20,21] The

TABLE I. Atomic positions in cubic perovskite crystal.

Site	Location	Coordination
A-cation	(2a)	(0, 0, 0)
B-cation	(2a)	(0.5, 0.5, 0.5)
O-anion	(6b)	(0.5, 0.5, 0) (0.5, 0, 0.5) (0, 0.5, 0.5)
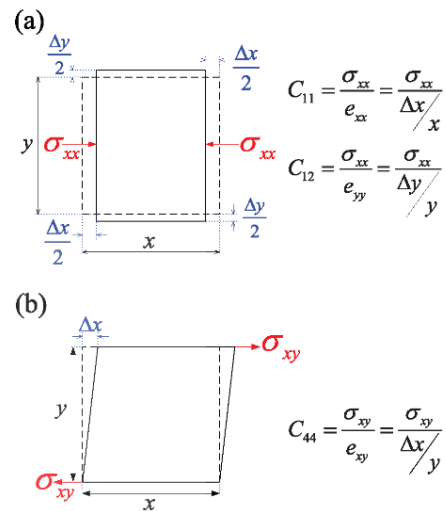
FIG. 2. Representation of (a) longitudinal compression (C_{11}) and transverse expansion (C_{12}), and (b) shear modulus (C_{44}). The figure is reproduced based on the work of Elliott.[21]

schematic representations of the three elastic constants of materials with the cubic symmetries are represented in Fig. 2.

For the elastic constants calculations, the "energy-strain relation" approach[22] was employed. In this approach, the elastic energy density (U) can be expressed as a quadratic function of the strains as[20]

$$U = \frac{1}{2}\sum_{i=1}^{6}\sum_{j=1}^{6} C_{ij}e_i e_j, \qquad (1)$$

where the elastic constants C_{ij} can be obtained from the derivative of U with respect to the associated strain components.[20] To calculate C_{11} elastic constants, a strain configuration $D_1 = (e, 0, 0, 0, 0, 0)$ was used. The elastic energy density in Eq. (1) for this specific strain configuration can be written in the matrix form as

$$U_1 = \frac{1}{2}(e,0,0,0,0,0)\begin{pmatrix} C_{11} & C_{12} & C_{12} & 0 & 0 & 0 \\ C_{12} & C_{11} & C_{12} & 0 & 0 & 0 \\ C_{12} & C_{12} & C_{11} & 0 & 0 & 0 \\ 0 & 0 & 0 & C_{44} & 0 & 0 \\ 0 & 0 & 0 & 0 & C_{44} & 0 \\ 0 & 0 & 0 & 0 & 0 & C_{44} \end{pmatrix}\begin{pmatrix} e \\ 0 \\ 0 \\ 0 \\ 0 \\ 0 \end{pmatrix}. \qquad (2)$$

The multiplication product of Eq. (2) gives the energy of this strain configuration as $U_1 = \frac{1}{2}C_{11}e^2$. In practice, the elastic energy was calculated using first principles DFT calculations with the several values of the strain (e), and then the energy–strain curve was fitted to the third–degree polynomials. The second derivative of the energy with respect to the strain gives C_{11}. Following the similar steps, C_{12} elastic constant

Manuscript publised in Journal of Applied Physics

TABLE II. Calculated elastic constants (in GPa) for selected cubic perovskite materials. Values in parentheses are from the literature.

Materials	LDA			GGA		
	C_{11}	C_{12}	C_{44}	C_{11}	C_{12}	C_{44}
BeTiO$_3$	363	121	48	307	112	48
MgTiO$_3$	380	110	73	339	102	72
CaTiO$_3$	405	110	100	356	103	98
SrTiO$_3$	385	113	119	326	103	112
	(421,[a] 317[d])	(121,[a] 102[d])	(133,[a] 123[d])	(313,[a] 311[c])	(98,[a] 99[c])	(113,[a] 104[c])
BaTiO$_3$	357	123	137	303	111	125
	(358,[a] 305[e])	(115,[a] 106[e])	(150,[a] 128[e])	(301[a])	(104[a])	(132[a])
PbTiO$_3$	328	127	102	280	116	97
	(450,[a] 383[b])	(261,[a] 151[b])	(113,[a] 120[b])	(325[a])	(158[a])	(107[a])
PbZrO$_3$	363	93	64	317	88	64
PbHfO$_3$	379	96	76	338	93	75

[a]Calculations by Piskunov et al.[23]
[b]Calculations by Liu et al.[6]
[c]Calculations by Boudali et al.[7]
[d]Experiments by Bell and Rupprecht.[24]
[e]Calculations by Wang et al.[4]

can be calculated by using a strain configuration $D_2 = (e, e, 0, 0, 0, 0)$. The elastic energy for this strain configuration is $U_2 = (C_{11} + C_{12})e^2$. The second derivative with respect to the strain gives $C_{11} + C_{12}$. Since C_{11} is already known from the first step, C_{12} can be extracted. For C_{44} elastic constant, a strain configuration $D_3 = (0, 0, 0, e, 0, 0)$ can be used to get an elastic energy $U_3 = \frac{1}{2}C_{44}e^2$. The second derivative with respect to the strain directly gives C_{44}.

III. RESULTS AND DISCUSSION

As described in Sec. II, there are three independent elastic constants (C_{11}, C_{12}, and C_{44}) for cubic crystal. Each of them represents the directional mechanical responses of the crystal for different directions of applied forces (Fig. 2). The details can be found in several standard text books, for example, the book by Kittel.[20] The calculated elastic constants of some perovskite materials, selecting based on previously described criteria, are tabulated in Table II. For each constant, the energy-strain curve is calculated based on the first principles total energy calculations using LDA exchange correlation functional and is repeated again using GGA. Therefore, there are two sets of calculated results, one labeled LDA and another labeled GGA. LDA consistently gives slightly larger elastic constants than GGA. Our values are in good agreement with available calculated and experimental results by other groups.

To understand the trend of the elastic constants with respect to cation species, the elastic constants for materials with different A-site cations and B-site cations are plotted with respect to the atomic numbers of the varying cations in Fig. 3.

The longitudinal elastic constant, C_{11}, directly represent the stiffness of the crystal. It is based on the longitudinal compression as shown in Fig. 2. In Fig. 3(a), we can see that as the A-site cation is varied from Be to Ba, C_{11} increases until it reaches the maximum point, when Ca is used as the A-site cation, then decreases. As the B-site cation is varied from Ti to

Hf, C_{11} monotonically increases as shown in Fig. 3(b). Although the behavior of C_{11} with respect to A-site and B-site cations seems to be complicated, it can be explained using a simple explanation as following. The perovskite structure can be considered to be a network of two intercalating cage
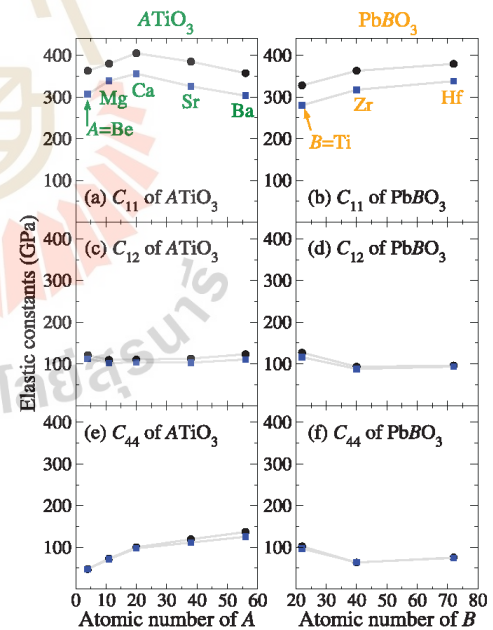

FIG. 3. Elastic constants (C_{ij}) of perovskite ATiO$_3$ (left) and PbBO$_3$ (right) as a function of atomic number of A-site and B-site cations, respectively. The blue-square symbols represent elastic constants based on GGA calculations while the black-circle symbols represent those based on LDA calculations.

Manuscript publised in Journal of Applied Physics

structures: a twelve-atom oxygen cage surrounding the A-site and a six-atom oxygen cage surrounding the B-site as illustrated in Figs. 1(b) and 1(a), respectively. Because the two networks share the same set of oxygen atoms, the volumes of the two types of cages are not independent but tied to each other. The volumes of the two cage types are not necessarily optimized at the same time. Therefore, the overall lattice constant of the crystal is optimized at the interplay point that compromises the volumes of the two types of cages. Both networks of cages contributed into the strength (C_{11}) of the crystal. When the atomic species that occupies the A-site is too small compared to that occupying the B-site, the strength of the crystal is dominated by the network of the B-site cages. On the other hand, when the atomic species that occupies the A-site is larger than that occupying the B-site, the strength of the crystal is dominated by the network of the A-site cages. The crystal becomes the most stiff (C_{11} reaches its maximum value) when the size of atomic species that occupies the A-site is comparable to that occupies the B-site; the point where both types of cages contributed to the stiffness of the crystal. As we varied the A-site cation and fixed the B-site cation to be Ti, the maximum C_{11} takes place when an A-site atom is Ca, which has the size most comparable to Ti among all Group-II elements used for this study. At other points, only one type of the cages is dominating the stiffness, resulting in a lower C_{11}. By the same logic, the behavior of C_{11} with respect to the changes of the B-site cation can also be explained. When we change the B-site cation, the A-site cation is fixed to be Pb. We would expect C_{11} to be the largest when the B-site cation is comparable to Pb, in this case Hf. Therefore, it is not surprising that C_{11} monotonically increases as we varied the B-site cation from Ti to Hf. C_{11} is expected to shift lower for $PbRfO_3$ (not studied here).

The transverse elastic constant, C_{12}, is based on the transverse expansion as shown in Fig. 2. In Fig. 3(c), we can see that C_{12} is not very sensitive to the changing of A-site cations, when the B-site cation is kept fixed as Ti. This is because C_{12} is mainly dominated by the distortion of the six-atom oxygen cage surrounding B-site, i.e., as the cage is squeezed on the side, it is expected to heavily expand in the transverse direction. As we change A-site cations, the center of the oxygen cages remains to be Ti. As a result, C_{12} remains almost constant. On the other hand, in Fig. 3(d), C_{12} is slightly decreased as the B-site cation was changed from Ti to Zr and remained almost unchanged, as it is changed further to a larger Hf cation. Changing B-site cations directly affect the six-atom oxygen cages. As the B-site cations (Ti) were replaced by larger cations (Zr or Hf) the cages are expanded and the polyhedral shape turns weaker, leading to a smaller C_{12}.

The shear elastic constant, C_{44}, is based on the distortion shown in Fig. 2. In Fig. 3(e), we can see that C_{44} is increased with the size of A-site cations. This indicates that C_{44} is directly dominated by the A-site cage. Because the overall lattice constant is partly controlled by the oxygen cage, for small A-site cations, the A-site cages are expanded, resulting in the weak bonds (between A-cation and its neighboring O atoms) and small C_{44}. As the A-site cations turn larger and become comparable to or even larger than the B-site cations,

their bonds with O become stronger making the A-site cage more difficult to shear. Hence, C_{44} increases. On the other hand, C_{44} is decreased as the B-site cation was changed from Ti to Zr and remained almost unchanged, as it is changed further to a larger Hf cation as shown in Fig. 3(f). This can be explained using the same logic; C_{44} is dominated by the A-site cage (in this case the twelve-atom oxygen cage surrounding Pb). As the B-site cations are changed from Ti to Zr, the size of the six-atom oxygen cages increases, pushing the Pb-O bonds to a value larger than their optimum length leading to smaller C_{44}.

IV. CONCLUSION

Elastic properties of perovskite $ATiO_3$ (A = Be, Mg, Ca, Sr, and Ba) and $PbBO_3$ (B = Ti, Zr, and Hf) were systematically studied by first principles calculations. Both LDA and GGA exchange and correlations were used in the calculations. The calculated elastic constants are in good agreement with available literatures. The elastic constants obtained using LDA are consistently larger than those obtained using GGA. For $ATiO_3$, C_{11} was found to increase with the atomic size of A until it reaches the maximum point when the atomic size of A-site and B-site atoms is comparable. As the atomic size of A further increased, C_{11} was found to decrease. For $PbBO_3$, C_{11} was found to monotonically increase with the atomic size of B, because B is always smaller than Pb in this study. C_{12} was found to be almost constant for the entire series of $ATiO_3$. However, for $PbBO_3$, C_{12} was found to slightly decrease as the size of B-site cations increases. C_{44} elastic constant was found to monotonically increase with the size of A-site cations for the $ATiO_3$ system and slightly decrease with the size of B-site cations for the $PbBO_3$. The discussions of the changes of the elastic constants with respect to the cation sizes were given based on the nature of the crystal structure.

ACKNOWLEDGMENTS

[1]K. Sarasamak, S. Limpijumnong, and W. R. L. Lambrecht, Phys. Rev. B **82**(3), 035201 (2010).
[2]K. Sarasamak, A. J. Kulkarni, M. Zhou, and S. Limpijumnong, Phys. Rev. B **77**(2), 024104 (2008).
[3]K. Sarasamak, S. Limpijumnong, and W. R. L. Lambrecht, Comput. Mater. Sci. **49**(1, Supplement), S43–S46 (2010).
[4]J. J. Wang, F. Y. Meng, X. Q. Ma, M. X. Xu, and L. Q. Chen, J. Appl. Phys. **108**(3), 034107 (2010).
[5]X. Meng, X. Wen, and G. Qin, Comput. Mater. Sci. **49**(4, Supplement), S372–S377 (2010).
[6]Y. Liu, G. Xu, C. Song, Z. Ren, G. Han, and Y. Zheng, Mater. Sci. Eng.: A **472**(1–2), 269–272 (2008).
[7]A. Boudali, M. D. Khodja, B. Amrani, D. Bourbie, K. Amara, and A. Abada, Phys. Lett. A **373**(8–9), 879–884 (2009).
[8]M. F. M. Taib, M. K. Yaakob, A. Chandra, A. K. Arof, and M. Z. A. Yahya, Adv. Mater. Res. **501**(7), 342–346 (2012).

Manuscript published in Journal of Applied Physics

[9]Z. Li, S. K. Chan, M. H. Grimsditch, and E. S. Zouboulis, J. Appl. Phys. **70**(12), 7327–7332 (1991).

[10]D. Lheureux, M. Fischer, A. Polian, J. P. Itie, M. Gauthier, and G. Syfosse, in *1999 IEEE Ultrasonics Symposium Proceedings, Caesars Tahoe, NV, USA, 17–20 Oct 1999*, edited by S. C. Schneider, M. Levy, and B. R. McAvoy (IEEE, 1999), pp. 533–536.

[11]E. Poindexter and A. A. Giardini, Phys. Rev. **110**(5), 1069–1069 (1958).

[12]W. Schranz, P. Sondergeld, A. V. Kityk, and E. K. H. Salje, Phase Transitions **69**(1), 61–76 (1999).

[13]P. Hohenberg and W. Kohn, Phys. Rev. **136**(3B), B864–B871 (1964).

[14]W. Kohn and L. J. Sham, Phys. Rev. **140**(4A), A1133–A1138 (1965).

[15]G. Kresse and J. Furthmüller, Phys. Rev. B **54**(16), 11169–11186 (1996).

[16]D. M. Ceperley and B. J. Alder, Phys. Rev. Lett. **45**(7), 566–569 (1980).

[17]J. P. Perdew and A. Zunger, Phys. Rev. B **23**(10), 5048–5079 (1981).

[18]J. P. Perdew, K. Burke, and M. Ernzerhof, Phys. Rev. Lett. **77**(18), 3865–3868 (1996).

[19]H. J. Monkhorst and J. D. Pack, Phys. Rev. B **13**(12), 5188–5192 (1976).

[20]C. Kittel, *Introduction to Solid State Physics* (John Wiley & Sons, Inc., USA, 1996).

[21]S. R. Elliott, *The Physics and Chemistry of Solids* (John Wiley & Sons, Ltd., Chichester, England, 1998).

[22]Y. Le Page and P. Saxe, Phys. Rev. B **63**(17), 174103 (2001).

[23]S. Piskunov, E. Heifets, R. I. Eglitis, and G. Borstel, Comput. Mater. Sci. **29**(2), 165–178 (2004).

[24]R. O. Bell and G. Rupprecht, Phys. Rev. **129**(1), 90–94 (1963).
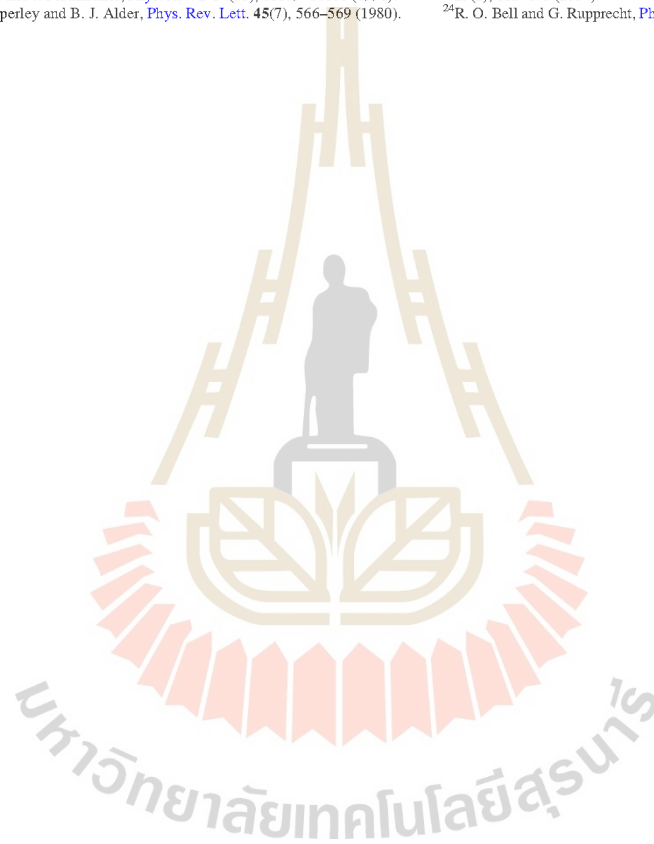
Manuscript publised in Journal of Chinese of Chemical Society

Article

First Principles Calculations of Structural and Elastic Properties of Perovskite Crystals: The Case of SrTiO$_3$

Narasak Pandech,[a,b,c] Kanoknan Sarasamak[a,d]* and Sukit Limpijumnong[a,b,c]

[a]School of Physics and NANOTEC-SUT Center of Excellence on Advanced Functional Nanomaterials, Suranaree University of Technology, Nakhon Ratchasima 30000, Thailand
[b]Synchrotron Light Research Institute, Nakhon Ratchasima 30000, Thailand
[c]Thailand Center of Excellence in Physics (ThEP Center), Commission on Higher Education, Bangkok 10400, Thailand
[d]College of Nanotechnology, King Mongkut's Institute of Technology Ladkrabang, Bangkok 10520, Thailand

The structural and elastic properties of perovskite crystals can be independently calculated by using first principles calculations without bias. The detailed calculation of cubic perovskite ($Pm\overline{3}m$) crystal by first-principles calculations both LDA and GGA approaches was shown, using SrTiO$_3$ as an illustration case. The equilibrium volumes and bulk modulus of SrTiO$_3$ were evaluated by fitting to Birch - Murnaghan equation of states. The C_{11}, C_{12}, and C_{44} elastic constants were obtained from a polynomial fit to the calculated energy-strain relations. For SrTiO$_3$, the calculated lattice constants, bulk modulus, and all three elastic constants by both LDA and GGA calculations are in good agreement with experimental values. Because LDA gives a slightly smaller lattice constant compared to that obtained from GGA, the bulk modulus and all three elastic constants obtained from LDA are slightly larger than those values obtained from GGA. The calculation steps illustrated here can be used as a guideline to study elastic properties of other novel materials.

Keywords: First principles; Elastic properties; Perovskite; SrTiO$_3$

Narasak Pandech is currently a PhD student in the group of Prof. Sukit Limpijumnong at Suranaree University of Technology. His research interest is on first principles study of crystal properties; focusing on metal oxides. He graduated with a MSc degree in Physics in 2013 from Suranaree University of Technology under Prof. Sukit Limpijumnong's supervision and a BSc degree in Physics in 2008 from Khon Kaen University.

Kanoknan Sarasamak is currently an assistant professor at the College of Nanotechnology, King Mongkut's Institute of Technology Ladkrabang and on sabbatical leave to visit Prof. Sukit Limpijumnong's group at Suranaree University of Technology. Her main research is on first principles study of metal oxides and nano materials. She completed her PhD degree in Physics from Suranaree University of Technology in 2008 under the supervision of Prof. Sukit Limpijumnong followed by a postdoc training at Asia Pacific Center for Theoretical Physics (South Korea) in 2011.

Sukit Limpijumnong is currently a full professor of Physics and a Vice Rector for Academic Affairs and Innovation at Suranaree University of Technology. He is also the president of the Thai Physics Society. In 2000, he completed his PhD degree in Physics from Case Western Reserve University, Cleveland, OH, under the supervision of Prof. Walter R.L. Lambrecht. This was followed by a postdoctoral research at Xerox Palo Alto Research Center with Dr. Chris G. Van de Walle. His main research is on first principles study of defects and alloys in semiconductors, oxides and nano materials.

WILEY ONLINE LIBRARY
1

Manuscript publshed in Journal of Chinese of Chemical Society

Article

Pandech et al.

INTRODUCTION

Elastic properties of materials are very important for describing and predicting their mechanical behaviors in different practical situations. Because first principles approach is known to be reliable for studying materials behaviors without bias, it has been extensively used on a wide range of properties and classes of materials; including elastic properties of perovskite oxides. Recently, we employed first principles calculations to study series of perovskite oxides.[1] In that work, both A-site and B-site cations of ABO_3 perovskite oxides were systematically varied in order to see their effects on the elastic parameters. The density functional first principles calculations with local density approximation (LDA) and generalized gradient approximation (GGA) were employed. Earlier, our group also employed first principles calculations to study various wurtzite compounds.[2] However, in our earlier works, calculation details were not illustrated in a step-by-step manner. Here, we provide such computational details by using $SrTiO_3$ as an illustration case so that one can follow and repeat the same steps to calculate elastic properties of other novel materials.

Strontium Titanate, $SrTiO_3$, is one of the perovskite-type crystals that commonly studied both theoretically and experimentally since it has a high symmetry structure and high quality crystals are available.[3-7] Therefore, we chose it for the illustration here. The crystal structure of $SrTiO_3$ is illustrated in Figure 1. Sr^{2+} and O^{2-} form a face center cubic structure with Sr^{2+} ions at the corners and O^{2-} ions at the face center sites. Ti^{4+} ions occupy the octahedral holes created by the oxygen (in another words, at the center of the cube). The structure has a three-dimensional net of corner sharing [Ti-O] octahedral with Sr^{2+} ions in the twelve fold cavities in between the polyhedral. This gives it a high symmetry structure as a cubic crystal structure in the nature. The lattice parameters of $SrTiO_3$ were obtained by X-ray powder diffraction in many experimental works.[4,6,8] The elastic properties of $SrTiO_3$ have also been widely studied both theoretically and experimentally.[3,5,7,9,10] Here, we will illustrate the computational procedure employed to obtain the three independent elastic constants of the cubic perovskite $SrTiO_3$ from first principles calculations.

The computational method will be explained in Section 2. The calculated results of structural and elastic properties of the $SrTiO_3$ compared with the values from the available literatures will be discussed in Section 3. Finally, in Section 4, we conclude.

COMPUTATIONAL METHOD

The computational approach employed is based on first principles density functional theory (DFT)[11,12] with the plane wave pseudo-potential method as implemented in Vienna *Ab-initio* Simulation Package (VASP).[13] Both local density approximation (LDA)[14,15] and generalized gradient approximation (GGA)[16] were used for the exchange-correlation terms. The ultrasoft version of the pseudo-potential implemented in the VASP code allows a low cut off energy for the plane wave expansion of only 500 eV. We used a $8\times8\times8$ Monkhrost-Pack scheme[17] for k-point sampling integrations.

A cubic perovskite structure used in this work is shown in Figure 1. It has the space group $Pm\bar{3}m$(#221) with the Wychoff positions: Sr 1a (0, 0, 0), Ti 1b (0.5, 0.5, 0.5) and O 3c (0, 0.5, 0.5), (0.5, 0.5, 0), and (0.5, 0, 0.5).

The total energies as a function of volume, $E(V)$, of a unit cell of cubic perovskite $SrTiO_3$ were calculated and fitted to the Birch - Murnaghan's equation of state[18,19] to obtain the equilibrium volume (V_0), the bulk modulus (B_0), and its pressure derivative (B').

There are three independent elastic constants for the cubic structures, denoted by C_{11}, C_{12}, and C_{44}.[20] Their values can be determined from the crystal total energy calculations for three different strain configurations in the form $D = [e_1, e_2, e_3, e_4, e_5, e_6]$. The strain parameters, e, are
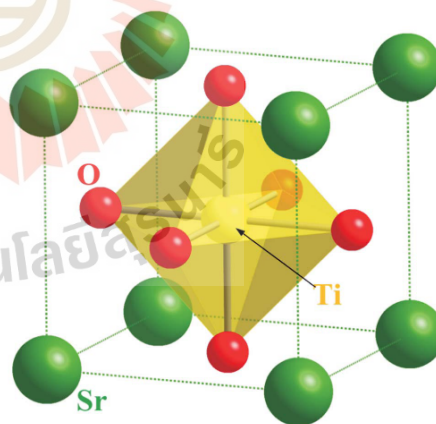
Fig. 1. Illustration of a cubic perovskite structure. The green spheres represent the Sr atoms, the yellow sphere represents the Ti atom, and the red spheres represent the O atoms.

Manuscript publised in Journal of Chinese of Chemical Society

related to the usual strain components, ε, via $e_1 = \varepsilon_{xx}$, $e_2 = \varepsilon_{yy}$, $e_3 = \varepsilon_{zz}$, $e_4 = (\varepsilon_{zx} + \varepsilon_{xz})/2$, $e_5 = (\varepsilon_{zy} + \varepsilon_{yz})/2$ and $e_6 = (\varepsilon_{yx} + \varepsilon_{xy})/2$. For the elastic constants calculations, the "energy-strain relation" approach[21] was employed. In this approach, the elastic energy density (U) can be expressed as a quadratic function of the strains as,[20]

$$U = \frac{1}{2}\sum_{i=1}^{6}\sum_{j=1}^{6} C_{ij} e_i e_j \qquad (1)$$

where the elastic constants C_{ij} can be obtained from the derivative of U with respect to the associated strain components.[20]

In this work, we used a first principles calculations method to calculate the elastic energy for various strains (e) configurations. Then the C_{ij} elastic constants are obtained from the fit of the second-degree polynomial to the calculated data. The three strain configurations with the corresponding elastic energy density (U) used in this work can be written as,

$$D_1 = (e,0,0,0,0,0) \rightarrow U_1 = \frac{1}{2}C_{11}e^2 \qquad (2)$$

$$D_2 = (e,e,0,0,0,0) \rightarrow U_2 = (C_{11} + C_{12})e^2 \qquad (3)$$

$$D_3 = (0,0,0,e,0,0) \rightarrow U_3 = \frac{1}{2}C_{44}e^2 \qquad (4)$$

RESULTS AND DISCUSSION

The calculated total energies as a function of the unit cell volumes (in the unit of Å^3) are shown as dots in Figure 2. The fit according to Birch - Murnaghan equation of states is shown as a solid curve. The best fit gives parameters $V_0 = 57.93\ \text{Å}^3$, $B = 1.67\ \text{eV/Å}^3$, and $B' = 4.09$ (unitless). To convert from eV/Å^3 to GPa, simply multiply by a conversion factor 1.602×10^2. The bulk modulus and its pressure derivative obtained are tabulated in Table 1.

To determine the elastic constants, we calculated the elastic energy density U for several (seven) strains (e) between -0.04 and 0.04, and fitted the results to the third-degree polynomials. Figure 3 shows the calculated energy-strain plots with the third-degree polynomials fitting lines for the three sets of strain configurations used for calculating the elastic constants (C_{ij}) in both LDA (left) and GGA (right) functional. The second-derivative of the energy with respect to the strain gives us the elastic constants. For example, to calculate C_{11} elastic constant, a strain configu-

ration $D_1 = (e, 0, 0, 0, 0, 0)$ was used. The elastic energy for this strain configuration is $U_1 = (1/2)C_{11}e^2$. The best-fit third-degree polynomial (for the case of LDA) shown in the upper left panel of Figure 3 is $U_1 = 6.215e^3 + 1.0215e^2 - (4.59 \times 10^{-3})e + (1.83 \times 10^{-6})\ \text{eV/Å}^3$. The second derivative of this elastic energy with respect to the strain gives C_{11}. This gives $C_{11} = 2 \times 1.0215\ \text{eV/Å}^3 = 2.403 \times 1.602 \times 10^2\ \text{GPa} = 385$ GPa (tabulated in Table 1). Similarly, C_{12} elastic constant can be obtained by using a strain configuration $D_2 = (e, e, 0, 0, 0, 0)$. The best-fit third-degree polynomial (for the case of LDA) shown in Figure 3 is $U_2 = 19.221e^3 + 3.109e^2 - (9.27 \times 10^{-3})e + (1.24 \times 10^{-5})\ \text{eV/Å}^3$. The elastic energy for
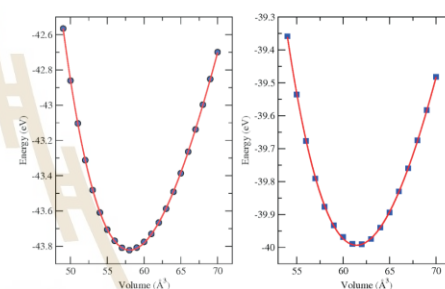
Fig. 2. The energy of cubic perovskite SrTiO₃ as a function of unit cell volumes (V) obtained from LDA (left) and GGA (right). The equilibrium volume (V_0), the bulk modulus (B_0), and its pressure derivative (B') can be obtained by fitting the calculated results to the equation of states.

Table 1. Calculated lattice constants (a), volumes (V_0), bulk modulus (B), its pressure derivative (B'), and elastic constants of SrTiO₃ in cubic perovskite structure compare with the literatures

	This work		Other calculations		Exp.
	LDA	GGA	LDA	GGA	
a (Å)	3.87	3.94	3.86[a]	3.95[a]	3.90[d]
V_0(Å³)	57.97	61.48	57.3[a]	61.2[b]	59.3[d]
B (GPa)	227	224.1	214[a]	169.7[b]	174[c]
B'	4.09	4.00	-	4.43[b]	-
C_{11} (GPa)	385	326	421[a]	313[a],3[b]	317.2[c]
C_{12} (GPa)	113	103	121[a]	98[a],99[b]	102.5[c]
C_{44} (GPa)	119	112	133[a]	113[a]104[b]	123.5[c]

[a] Calculations by Piskunov *et al.*[22]
[b] Calculations by Bouadali *et al.*[7]
[c] Experiments by Bell and Rupprecht.[23]
[d] Experiments by Abramov and Tsirelson.[24]

Manuscript publised in Journal of Chinese of Chemical Society

Article

Pandech et al.
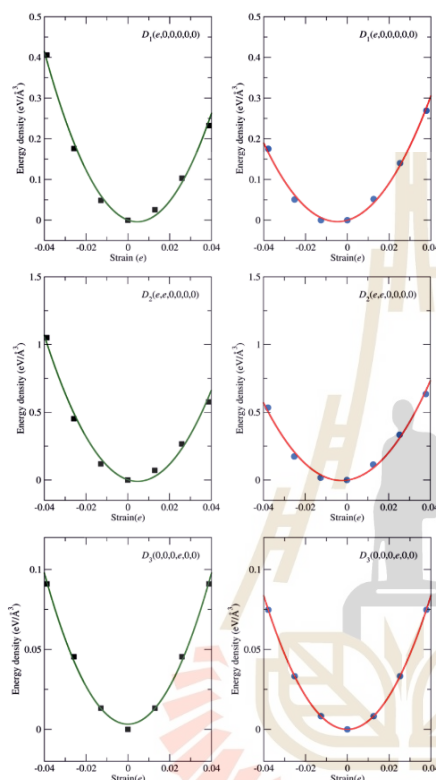
Fig. 3. The elastic energy as a function of strain for three strain configurations of cubic perovskite SrTiO$_3$ obtained from LDA (left) and GGA (right) calculations.

this strain configuration is $U_3 = (1/2)C_{44}e^2$ and the second derivative of this elastic energy with respect to the strain gives $C_{11}+C_{12}$. Because C_{11} is already obtained from the previous step, C_{12} can be easily extracted. For C_{44} elastic constant, a strain configuration $D_3 = (0, 0, 0, e, 0, 0)$ was used. The best-fit second-degree polynomial (for the case of LDA) shown in Figure 3 is $U_3 = 0.371e^2 - (1.72\times10^{-6})e + (2\times10^{-5})$ eV/Å^3. Note that, for C_{44}, the function is an even function by symmetry. Therefore, the third degree coefficient is vanished. The elastic energy for this strain configuration is $U_3 = (1/2)C_{44}e^2$ and the second derivative of this elastic energy with respect to the strain gives C_{44}.

The calculated lattice constants, volumes, bulk modulus (B), its pressure derivative (B') and elastic constants (C_{11}, C_{12}, and C_{44}) of SrTiO$_3$ in both LDA and GGA calculations are tabulated in Table 1. Our calculated results are in good agreement with other calculations and experimental data. It can be clearly seen that the LDA calculation gives slightly smaller value of lattice constant compared to the measured value. On the other hand, the value obtained from GGA calculation is slightly larger than the measured one. However, the disagreement between the calculated lattice constants and experimental values is less than 2%. Since LDA calculation gives smaller lattice constant when compared with GGA calculation, the bulk modulus and all elastic constants (C_{11}, C_{12}, and C_{44}) obtained from LDA calculation are slightly larger than those obtained from GGA calculation. These behaviors are commonly observed in the calculations of other materials as well. Our calculated results indicate that LDA calculation overestimates both bulk modulus and elastic constants when compared to experimental data. For SrTiO$_3$, the calculated bulk modulus and elastic constants from the GGA calculations are in better agreement with the experimental values than those from LDA calculations.

CONCLUSIONS

The first-principles calculations of structural and elastic properties of the cubic perovskite crystal have been illustrated by using SrTiO$_3$ as a test case. Both LDA and GGA exchange-correlation functional were used. The calculated lattice parameters and elastic constants are in good agreement with previous studies with similar exchange-correlation functional. LDA calculation gives slightly smaller lattice constant and larger bulk modulus and all three elastic constants than those obtained from GGA calculation. In comparison with experimental results, GGA exchange-correlation functional provides better agreement for the case of SrTiO$_3$.

ACKNOWLEDGEMENTS

Manuscript published in Journal of Chinese of Chemical Society

Structural and Elastic Properties of SrTiO₃

Synchrotron Light Research Institute (Public Organization), Thailand.

REFERENCES

1. Pandech, N.; Sarasamak, K.; Limpijumnong, S. *J. Appl. Phys.* **2015**, *117*(17), 174108.
2. Sarasamak, K.; Limpijumnong, S.; Lambrecht, W. R. L. *Phys. Rev. B* **2010**, *82*(3), 035201.
3. Hachemi, A.; Hachemi, H.; Ferhat-Hamida, A.; Louail, L. *Phys. Scripta* **2010**, *82*(2), 025602.
4. Müller, K. A.; Berlinger, W.; Waldner, F. *Phys. Rev. Lett.* **1968**, *21*(12), 814-817.
5. Schranz, W.; Sondergeld, P.; Kityk, A. V.; Salje, E. K. H. *Phase Trans.* **1999**, *69*(1), 61-76.
6. van Benthem, K.; Elsässer, C.; French, R. H. *J. Appl. Phys.* **2001**, *90*(12), 6156-6164.
7. Boudali, A.; Khodja, M. D.; Amrani, B.; Bourbie, D.; Amara, K.; Abada, A. *Phys. Lett. A* **2009**, *373*(8 9), 879-884.
8. Mats, J.; Peter, L. *J. Phys: Condens. Mat.* **2008**, *20*(26), 264001.
9. Poindexter, E.; Giardini, A. A. *Phys. Rev.* **1958**, *110*(5), 1069-1069.
10. Lebedev, A. I. *J. Adv. Dielectr.* **2012**, *02*(01), 1250003.
11. Hohenberg, P.; Kohn, W. *Phys. Rev.* **1964**, *136*(3B), B864-B871.
12. Kohn, W.; Sham, L. J. *Phys. Rev.* **1965**, *140*(4A), A1133-A1138.
13. Kresse, G.; Furthmüller, J. *Phys. Rev. B* **1996**, *54*(16), 11169-11186.
14. Ceperley, D. M.; Alder, B. J. *Phys. Rev. Lett.* **1980**, *45*(7), 566-569.
15. Perdew, J. P.; Zunger, A. *Phys. Rev. B* **1981**, *23*(10), 5048-5079.
16. Perdew, J. P.; Burke, K.; Ernzerhof, M. *Phys. Rev. Lett.* **1996**, *77*(18), 3865-3868.
17. Monkhorst, H. J.; Pack, J. D. *Phys. Rev. B* **1976**, *13*(12), 5188-5192.
18. Birch, F. *Phys. Rev.* **1947**, *71*(11), 809-824.
19. Murnaghan, F. D. *Am. J. Math* **1944**, *49*(2), 235.
20. Kittel, C. *Introduction to Solid State Physics*, 7th ed.; John Wiley & Sons, Inc.: New York, 1996; pp 80-90.
21. Le Page, Y.; Saxe, P. *Phys. Rev. B* **2001**, *63*(17), 174103.
22. Piskunov, S.; Heifets, E.; Eglitis, R. I.; Borstel, G. *Comp. Mater. Sci.* **2004**, *29*(2), 165-178.
23. Bell, R. O.; Rupprecht, G. *Phys. Rev.* **1963**, *129*(1), 90-94.
24. Abramov, Y. A.; Tsirelson, V. G. *Acta Cryst. B* **1995**, *51*(6), 942.

Manuscript published in ACS Omega

ACS OMEGA

http://pubs.acs.org/journal/acsodf

Article

Effects of the van der Waals Interactions on Structural and Electronic Properties of CH₃NH₃(Pb,Sn)(I,Br,Cl)₃ Halide Perovskites

Narasak Pandech, Thanundon Kongnok, Nirawith Palakawong, Sukit Limpijumnong,
Walter R. L. Lambrecht, and Sirichok Jungthawan*

Read Online

ACCESS | Metrics & More | Article Recommendations | Supporting Information

ABSTRACT: In hybrid perovskite materials like $CH_3NH_3PbI_3$, methylammonium (MA) lead iodide (MAPI), the orientation of the MA⁺ cations and their ordering can significantly affect the structure of the inorganic framework. Although the states near the band edges are known to be primarily derived from the Pb and halogen orbitals rather than from the organic ion, the latter may have an indirect effect through their impact on the structural relaxation. In this work, we investigate both the structural relaxation effects of the inorganic framework in response to the MA⁺ orientation and their impact on the electronic structure near the band edges. Calculations are performed for $MA(Pb,Sn)X_3$ with (X = I, Br, and Cl) materials for both Pb- and Sn-based compounds. The work focuses on the high-temperature α-phase, which is nominally cubic if averaged over all possible MA orientations and in which no alternating rotations of the octahedral occur, so that the unit cell is the smallest possible. The effects of van der Waals (vdW) corrections to density functional theory on the structural relaxation are investigated. Our results reveal that the vdW interactions between the MA⁺ cation and the inorganic framework can strongly affect the optimized orientation and position of the molecule and the resulting distortion of the inorganic framework. Consequently, it also affects the electronic properties of the materials and specifically can change the band structure from direct to indirect band gaps. The robustness of this result is studied by comparing hybrid functional calculations and quasiparticle self-consistent GW calculations as well as spin−orbit coupling.
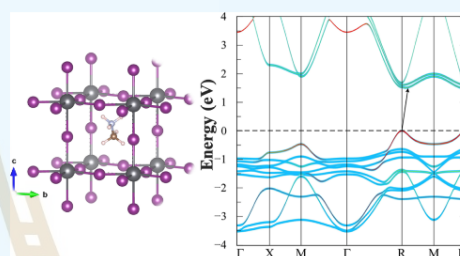
INTRODUCTION

Perovskites are crystalline materials with an ABX_3 structure similar to the $CaTiO_3$ mineral. The A-site cations are 12-fold coordinated, and divalent B-site cations are 6-fold coordinated. In the class of organic−inorganic halide perovskite materials, the A-site is a monovalent organic cation, for example, methylammonium ($CH_3NH_3^+$, MA⁺), the B-site is a divalent metal, for example, Pb^{2+}, Sn^{2+}, Ge^{2+}, and the X-site is occupied by the halogen ions, for example, I⁻, Br⁻, and Cl⁻. Recently, hybrid halide perovskite materials have emerged as new promising materials in photovoltaic applications. This class of materials has been known for a long time and has been studied in relation to their very particular dielectric properties.[1] However, the first application of organo-halide perovskite materials in photovoltaics can be traced back to 2009, with the work of Kojima and co-workers.[2] After the pioneering work, the number of applications of the hybrid perovskite in photovoltaics rapidly increased, especially in the case of lead-halide perovskite materials.[3−5] Notably, the solar cell efficiencies of halide perovskites have remarkably risen to about 20% such that they are a good alternative to Si solar

cells.[6−8] However, their stability and structural transformations remain a challenge.

The crystal structures of Pb- and Sn-based halide perovskite materials are temperature-dependent. Their exact structures are still under dispute because of the complexity introduced by the MA⁺ cation group. Experimentally, many research groups have attempted to identify the structures of the materials using neutron powder diffraction and also synchrotron X-ray powder diffraction.[5,9] At high temperature, the α-structure is cubic (with the space group $Pm\bar{3}m$ if the molecular orientations are ignored or MA is replaced by a symmetric Cs ion). However, the Pb or Sn ferroelectric displacement in its octahedron or the MA in-phase orientation can lead to a non-centrosymmetric tetragonal $P4mm$ space group.[3] The β-phase occurs by alternatingly tilting the octahedra clock and counterclockwise

about a single axis, thereby doubling the unit cell to a $\sqrt{2} \times \sqrt{2} \times 1$ cell and making the system tetragonal. In CsSnI$_3$, this leads to the $P4/mbm$ group because the tilts are in phase in the c-direction. However, with the additional ferroelectric symmetry breaking of the MA ions, the space group becomes $I4cm$.[3] Others however assigned the $I4/mcm$ spacegroup[5] to this phase in MAPbI$_3$. This phase occurs in SrTiO$_3$ where it also exhibits rotation of the octahedra about the z-axis but which alternates between clockwise and counterclockwise along the c-axis, thereby doubling the cell again to $\sqrt{2} \times \sqrt{2} \times 2$. On the other hand, the $I4/mcm$ phase which does maintain an inversion symmetry could also result from alternating the MA dipole orientations.[10] The transition temperature to this phase depends on the material and occurs at ~180 K in MAPbI$_3$[5] and 200 K in MASnI$_3$.[3] Finally, a second transition occurs at a lower temperature to an orthorhombic γ-phase in which octahedral tilts occur about two orthogonal axes, and the cell is doubled in the c-direction. The full space group determination in this phase has not been achieved for the different organic ions but is $Pnma$ in the case of the symmetric A ion and is thus assumed to be derived from this phase.[5] In MAPbI$_3$, this transition occurs between 100 and 150 K,[5] while for the Sn case, it occurs closer to 100 K.[3] In the low-temperature structure, the BX_6 octahedra are strongly deformed and restrict the rotational motion of MA$^+$ cations.[5] In this case, the organic cations are fully ordered and pinned and can rotate only along the C–N axis.[5,9] When the temperature increases, tetragonal and cubic structures appear. In the high-temperature structures, the organic cations become free to rotate inside the dodecahedral cages, and they are disordered.[5,9] Nuclear magnetic resonance measurements[11] have shown that the probable location of the MA cations cannot be determined in the cubic phase, and the reorientation time of the MA cations is in the order of picoseconds. Therefore, the presence of organic molecules and their mobility are a challenge in the study of these types of materials.

In organic–inorganic halide perovskite materials, the MA-cation groups reside within the network of corner-sharing BX_6 octahedra and are stabilized by van der Waals (vdW) interactions. Some previous theoretical works[12–15] have already revealed the importance of the presence of dispersive forces in these types of materials on structural properties. The effect of the MA orientations on the electronic structure is less clear. Because the states near the band edges are either Pb-s, I-p mixed at the valence band maximum (VBM) or Pb-p like at the conduction band minimum (CBM), one may think that the MA has little effect on them. On the other hand, the MA orientations can affect the overall symmetry and this may lead to splitting of the CBM.

In this work, we conducted vdW-corrected density functional theory (DFT) calculations to examine the importance of vdW interactions on the MA-cation structural parameters and consequently to examine the electronic properties of the $MABX_3$ (B = Pb, Sn; X = I, Br, Cl) halide perovskite materials. Our results reveal that the inclusion of the vdW interactions in DFT calculations affects the MA-cation orientation, which influences the structural properties of the inorganic network and consequently affects the electronic properties of the materials. Because the Perdew–Burke–Ernzerhof (PBE) and even vdW-corrected DFT can significantly underestimate the gap, we also conduct calculations of the same structures using the quasiparticle self-consistent GW (QSGW) method. Finally,

spin–orbit coupling (SOC) is known to be important in particular in the Pb-based compounds. Thus, we study the effect of both GW self-energy corrections and SOC on the electronic structure in relation to the orientation of the MA molecules and their corresponding induced structural distortions. The SOC in combination with the electric field-induced symmetry breaking arising from the dipolar molecules leads to the Rashba effect, which can affect the location of CBM in k-space.

■ RESULTS AND DISCUSSION

Structural Relaxation. Before we go into our calculated results, we want to refer to two previous studies of the molecular orientations in the cubic phase of MAPbI$_3$ that are particularly relevant to our study. Motta et al.[16] performed a full structural optimization of MAPbI$_3$ within generalized gradient approximations (GGAs) including vdW corrections. It has been found that the results are sensitive to the initial orientation of the molecule being along [100] or [111]. In the former case, the molecule rotates toward a [110] or equivalent direction, while in the latter case, it remains in the [111] direction. Both the [110] and [111] orientations thus appear to be the favored orientations. We here extend that approach to the other halogens and to the case of Sn instead of Pb. Bechtel et al.,[17] on the other hand, took a more systematic approach for mapping out the energy landscape. They define all possible rotation degrees of freedom of the molecule, defined by a polar angle θ and azimuthal angle ϕ of the C–N axis of the molecule versus the [001] and [100] cubic axes, the rotation angle α of the molecule about its own axis, and the displacement of the molecule from its center along its own axis. They then map out the energy of the molecule as a function of these variables but while keeping the inorganic framework fixed. They found that the molecule translates along its own direction away from the nominal center of the dodecahedral site, in other words, the displacement of the molecule is important. The favored orientations found in this work are close [100] and [111] directions. Consequently, the initial orientation of the molecule for structural relaxations is either [100], [110], or [111] direction. The molecule and the framework are fully allowed to relax. Subsequently, we also performed calculations with constraint where the position of the molecule is kept at some angle as in the energy landscape studies of Bechtel et al.,[17] but the inorganic framework is allowed to fully relax along with the possible displacement of the molecule relative to the framework. All of these calculations were then performed with and without vdW corrections to ascertain their importance. After discussing the structural results, we will then examine their effect on the electronic band structure in the next section. Ferroelectric ordering was found to be slightly preferable energetically by Quarti et al.[10] On the other hand, Weller et al.[5] indicate the disordered alternating non-polar orientation of the MA molecules.

Let us start the discussion by presenting the relaxed crystal geometries. Initially, the structural optimizations have been performed at the level of the GGA–PBE calculations with and without including the vdW interactions for revealing the effects of internal interactions between the organic cation and the BX_6 inorganic framework. We perform a full structural relaxation without any symmetry constraints from the ideal cubic perovskite structure with staggered H-atoms arrangement (the H-atoms on the C-end and on the N-end are not aligned

with each other but rotated with respect to each other by 60°) adopted from Motta et al.'s calculation,[16] as depicted in Figure 1. The relaxations have been performed with various initial
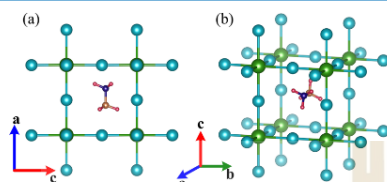
Figure 1. Illustration of the ideal cubic structure of $CH_3NH_3BX_3$ with staggered H-atoms arrangement in CH_3NH_3 molecule which is oriented along the [100] direction viewed along (a) b-crystallographic axis and (b) arbitrary crystallographic axis. Green, cyan, blue, orange, and red spheres represent the B-site atoms, X-site atoms, N-atoms, C-atoms, and H-atoms, respectively.

configurations of the MA cation, namely, oriented along the [100], [110], or [111] directions, as listed in Table 1. We note that the relaxation process is extremely sensitive to the initial MA-cation orientation. For example, when we started the relaxation with the MA$^+$ cation oriented along the [111] direction, the relaxed structure preserves its original MA$^+$ cation orientation in both cases of with and without including vdW interactions, as depicted in Figure 2c,d, respectively. This result is similar to that of Motta et al.[16] The calculated change in angle ($\Delta\theta$) of the C−N axis with respect to its initial orientation direction is very small, as shown in Table 1. In contrast, if we start the structural relaxation with the MA$^+$ cation oriented along the [100] direction, the relaxed structure does not preserve its original MA$^+$ cation orientation, instead, it may end up with the MA$^+$ cation orientated along the [10−
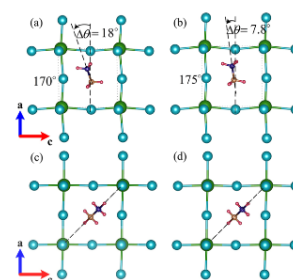

Figure 2. Illustration of relaxed structures of the cubic $CH_3NH_3PbI_3$ with and without vdW interactions (left and right panels, respectively) for different orientations of the MA$^+$ cation. (a,b) Relaxed structure of the MA cation initially oriented along the [100] direction. (c,d) Relaxed structure of the MA cation initially oriented along the [111] direction. The pictures are viewed along the y-axis or showing the x−z plane.

1] direction, as depicted in Figure 2a,b. The reason why particularly the [10−1] direction is favored as opposed to the in-principle equivalent [1±10] or [101] depends on the particular chosen orientation of the molecule about its own axis. As we will show later, the H atoms are in such positions to favor rotating in this particular direction by optimizing the hydrogen bonds with the halogen. This is why the vdW interactions are important in the structural optimization of these types of materials. In this case, the MA$^+$ cation shifts down along the x−z plane (see the inset of Figure 3) with the change in angle, ($\Delta\theta$) around 18° (in the case of MAPbI$_3$) when including the vdW interaction, as shown in Table 1. However, if one does not include the vdW interaction in the calculation, the calculated $\Delta\theta$ in this case is around 7.8° and

Table 1. Calculated Lattice Constants a, b, and c (Å), Unit Cell Volume V (Å^3), Deviate Angle from the Given Initial MA Orientation, $\Delta\theta$ (in Degree), Relative Energy (Rel. Energy, in meV), B−X−B Bond Angle (in Degree), and Hydrogen Bond Length (Å) of MABX_3 [a]

compounds	int. MA orient.	rel. energy	$\Delta\theta$	a	b	c	V	B−X−B bond angle	H_N−X	H_C−X
									calculated structural parameters	H-bonding
MAPbI$_3$	[100]	0.00	18 (7.8)	6.34 (6.48)	6.30 (6.43)	6.38 (6.49)	254.7 (270.2)	169.5 (174)	2.72 (2.8)	3.36 (3.6)
	[110]	14.4	9 (5.6)	6.34 (6.48)	6.40 (6.57)	6.27 (6.32)	252 (270.4)	175 (175)	2.75 (2.8)	3.40 (3.6)
	[111]	21.0	0.9 (0.5)	6.34 (6.47)	6.34 (6.47)	6.34 (6.47)	255.3 (270.4)	178 (178)	2.71 (2.7)	3.38 (3.6)
MAPbBr$_3$	[100]	0.00	23 (12.7)	5.94 (6.03)	5.89 (6.03)	6.03 (6.13)	211 (222.8)	169.1 (172)	2.45 (2.5)	3.31 (3.4)
	[110]	18.6	6.8 (4.6)	5.98 (6.08)	5.98 (6.08)	5.89 (6.03)	209.8 (221)	174 (173)	2.55 (2.5)	3.50 (3.5)
	[111]	35.4	0.9 (1.2)	5.97 (6.08)	5.97 (6.08)	5.97 (6.08)	212.7 (223.4)	177 (177)	2.41 (2.5)	3.10 (3.5)
MAPbCl$_3$	[100]	0.00	26 (17.5)	5.67 (5.74)	5.63 (5.73)	5.79 (5.90)	184.7 (193.8)	168 (171)	2.3 (2.4)	3.17 (3.2)
	[110]	23.1	6.6 (4.6)	5.73 (5.83)	5.73 (5.83)	5.63 (5.73)	184.2 (193.9)	174 (175)	2.3 (2.4)	3.3 (3.2)
	[111]	46.4	0.8 (1.3)	5.73 (5.83)	5.73 (5.83)	5.73 (5.83)	187.6 (197.2)	175 (176)	2.3 (2.4)	2.9 (3.2)
MASnI$_3$	[100]	0.00	20.1	6.26	6.19	2.27	243	172	2.7	3.3
	[110]	6.4	8.5	6.26	6.26	6.17	241.3	172	2.8	3.4
	[111]	20.3	0.01	6.24	6.24	6.24	243.4	177.4	2.7	3.3
MASnBr$_3$	[100]	0.00	26.5	5.89	5.80	5.95	202.9	170.6	2.43	3.2
	[110]	9.00	8.6	5.91	5.91	5.80	201.6	171	2.45	3.1
	[111]	34.6	0.03	5.88	5.79	5.95	204.5	176	2.47	3.05
MASnCl$_3$	[100]	0.00	28.4	5.72	5.55	5.75	182.6	171	2.25	2.89
	[110]	8.92	4.6	5.71	5.71	5.54	179.2	172	2.25	2.86
	[111]	33.17	0.03	5.70	5.70	5.70	185.4	176	2.26	2.85

[a]The numbers in parenthesis are obtained without including vdW.

Manuscript published in ACS Omega
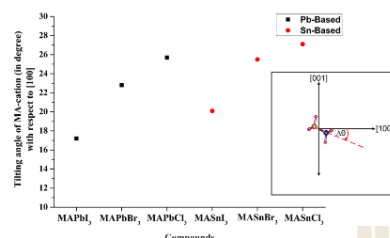
Figure 3. vdW-calculated tilting angle of the MA cation with respect to the initial [100] orientation ($\Delta\theta$), as represented in an inserted picture.

the relaxed structure is less distorted, as shown in Figure 2b. Including the vdW interaction, the calculated $\Delta\theta$ of the C−N axis with respect to the [100] direction increases when the halogen atom is changed from I⁻ to Br⁻ to Cl⁻ in both Pb- and Sn-based cases, as shown in Figure 3. The increase of the angle indicates a stronger interaction between the organic MA⁺ cation and the BX_6 inorganic framework and causes the relaxed structure to become more distorted, as indicated by a $B−X−B$ bond angle tabulated in Table 1. The calculated lattice parameters, when including the vdW interaction, are in very good agreement with the experimental values, with an error less than 1%. If the calculation does not include the vdW interaction, the calculated lattice parameters are larger than the experimental values by an error more than 3%. The calculated lattice constants of the MAPbX_3 (X = I, Br, and Cl) with vdW-included are 6.34, 5.96, and 5.71 Å which are in good agreement with the experimental values of 6.33, 5.90, and 5.67 Å, respectively.[1] For the MASnX_3 (X = I, Br, and Cl), the calculated lattice constants with vdW-included are 6.25, 5.89, and 5.68 Å, which are also in good agreement with the experimental values of 6.23, 5.88, and 5.67 Å, respectively.[3,18]

If we focus on the relaxed structures, the significant difference between these structures is the deformation of the BX_6 octahedra. In the case of initial [100] orientation, the relaxation of the MA⁻ cation induces the deformation and the symmetry reduction of the inorganic BX_6 octahedra. Such distortion causes the $B−X−B$ bonds to not lie parallel to the crystal directions but instead be slightly tilted by ∼10° from the ideal cubic structure when the vdW interaction is included (see Table 1). However, when excluding vdW interactions, they only tilted by ∼5° from the ideal cubic structure. In the case of [111] orientation, the $B−X−B$ bond angles are very close to 180°, indicating that the relaxed structure preserves a high symmetry cubic structure. In this case, the relaxed structure of the [111] orientation is still simple cubic (see Table 1). In contrast, the relaxed structure of the initial [100] orientation becomes tetragonal ($c/a \neq 1$).

Additionally, the hydrogen bond lengths were calculated and are listed in Table 1. The results show that the hydrogen atoms on the NH₃-side are closer to the BX_6 inorganic framework than those of the CH₃-side. It can be implied that the hydrogen atoms in NH₃-side dominate the strong interaction with the BX_6 inorganic framework. Although the relaxed structure is sensitive to the initial MA⁻ cation configuration, it is worth noting that the energy difference between these configurations is very small. The energy difference is calculated to be in the 21−50 meV range in favor of a direction near the [10−1] direction (tilted from [100] by $\Delta\theta \sim 18°$ in the case of MAPbI₃), which is consistent to the previous studies of MAPbI₃.[16,17] The lowest energy structure we found (MAPbI₃ case) is consistent with the lowest energy structure calculated by Qiaoling Xu et al.[19] using $2 \times 2 \times 2$ supercell calculations, the MA cations are found in favored orientation to the [012] direction with the relative energy of ∼60 meV per formula unit. Indeed, it can be implied that these MA⁺ cation configurations represent the local energy minima.

After the full structural relaxation of the initial [100] orientation has been carried out, it is still unclear why the MA⁺ cation rotated downward in the $x−z$ plane instead of other
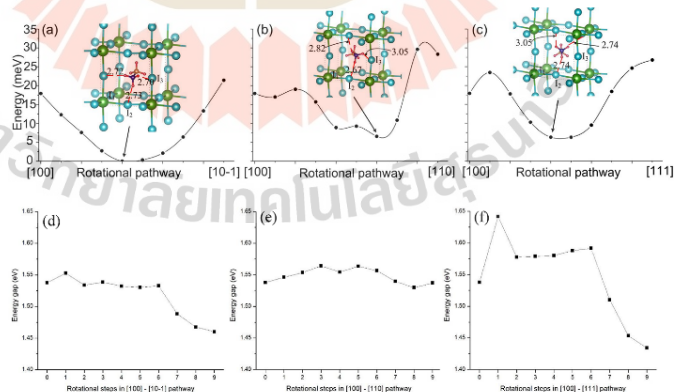
Figure 4. (a−c) Calculated relative energy and (d−f) variation of the band gap, for MAPbI₃ case, as a function of the rotational pathway of the C−N axis with respect to the [100] direction. (a,d) [100] → [10−1], (b,e) [100] → [110], and (c,f) [100] → [111]. The C−N atoms are fixed at each rotational angle, while the other atoms are allowed to relax. The inserts show the orientation and the hydrogen bond lengths (red dashed lines) that can be formed with the nearest halogen atoms near the minimum configuration.

Manuscript publised in ACS Omega

directions. Therefore, we have chosen the MAPbI$_3$ case as an example for further study. We performed the ground state energy calculation as a function of the rotational angle of the C−N axis with respect to the [100] direction, including the vdW interactions. Several pathways, namely, [100] → [10−1], [100] → [110], and [100] → [111] are considered. In the calculations, the staggered H-atoms arrangement is applied, the C−N axis and C−N bond length are fixed at each rotational angle while the other atoms and cell volume are allowed to relax. The calculated energies as a function of rotational angle in different pathways are depicted in Figure 4. From the plot, we can see that the calculated energies in the [100] → [10−1] pathway decrease until the rotational angle is around 20° and then the energy increases. This is consistent with the full unconstrained minimization presented above. At the lowest energy structure, three hydrogen atoms in NH$_3$-side bond with I$^-$ atoms almost equally, as depicted in Figure 4a. The energy difference between [100] and [10−1] orientations is very small, 3.5 meV. On the other hand, the calculated energies in the [100] → [110] pathway slightly fluctuate with the rotational angle and end up with the energy 10 meV higher than that of the [100] orientation. In this case, at the lowest energy point, one of the hydrogen atom in NH$_3$-side bonds with the I$^-$ atom stronger than other two hydrogen atoms, as depicted in Figure 4b. In the case of the [100] → [111] pathway, the calculated energy slightly increases and then decreases until the rotational angle is around 22°, then increase and end up with the energy 9 meV higher than that of the [100] orientation. In this case, at the lowest energy structure, two of hydrogen atoms on the NH$_3$-side present stronger bonds with the I$^-$ atoms than the other hydrogen atom, as depicted in Figure 4c. The lowest energies along the [100] → [110] and [100] → [111] pathways are ∼7 meV higher than along the [100] → [10−1] pathway. In addition, we can see that the energy difference in the 15−25° range of the [100] → [10−1] pathway is very shallow, indicating several local minima around that point. The difference in these different pathways lies in the way that the molecule's H-atoms are positioned relative to the halogen atoms along these paths. The more complex behavior for other than the optimal rotation pathway (a) shows that there is some optimal orientation of the molecule about its own axis such that it best optimizes the H bonds with the halogens.

From our calculated ground state energies in different pathways, we conclude that the fully structural relaxation process of the initial [100] orientation with the given staggered H-atoms arrangement, including the vdW interaction, ends up with the MA cation rotated downward in the x−z plane from [100] toward [10−1] in a local minimum energy near the [10−1] direction with the deviate angle, $\Delta\theta$, listed in Table 1.

Electronic Properties. The significant differences in the structural geometries are expected to impact on the electronic structure of the studied MABX_3. First, let us pick MAPbI$_3$ as an example to explain the effect of the vdW interaction on the electronic properties of the studied materials. The electronic band structures along the high symmetry points of the Brillouin zone calculated by using the GGA−PBE without SOC with different MA$^+$ cation orientations of the MAPbI$_3$ are depicted in Figure 5. Our GGA−PBE calculated band structures reveal that the orientations of the MA$^+$ cation have a profound impact on the nature of the band gap of MAPbI$_3$. In the case of the [111] orientation, the relaxed structure keeps the high symmetry of the cubic structure and
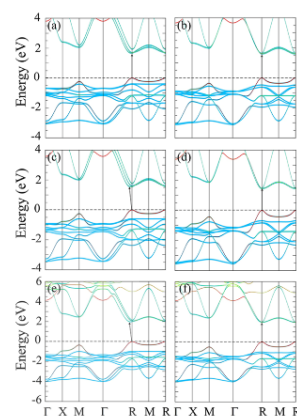

Figure 5. Calculated band structures without SOC of the CH$_3$NH$_3$PbI$_3$ for (a,b) PBE without including vdW, (c,d) PBE with including vdW, and (e,f) Heyd−Scuseria−Ernzerhof (HSE) with including vdW. Left and right panels represent the MA$^+$ cation initially orientated along [100] and [111] directions. The red, skyblue, and lime colors of each band represent the spd-projected wavefunction character of s, p, and d orbitals, respectively. The calculated VBM energies were shifted to zero.

gives the direct band gap at the R-point (0.5, 0.5, 0.5) of the Brillouin zone both with and without vdW interactions, as depicted in Figure 5b,d. On the other hand, in the case of the initial [100] orientation, the relaxed structures are strongly distorted due to the cation rotation and consequently affect the band structure: the CMB shifts along the $R \rightarrow \Gamma$ line, the band gap becomes indirect, as depicted in Figure 5c. These results are in good agreement with Motta et al.[16] Please note that the Grimme DFT-D3 approach changes the total energy and hence relaxation but not the exchange correlation potential used for the band structure calculations. In the case of exclusion of vdW interactions, the calculated band gap remains direct for both [100] and [111] orientations, as depicted in Figure 5a,b, respectively. This indicates that the relaxed structures do not present enough distortion to modify the band structure significantly, and the vdW correction is necessary for the structural relaxation of the halide perovskite systems.

The vdW-calculated band gap without SOC of MAPbI$_3$ lies in the 1.45−1.55 eV (see Table 2) range close to the experimental value of about 1.55 eV,[2,20] while the calculated band gap without vdW-interaction lies in 1.6−1.7 eV, slightly larger than the experimental values. The GGA−PBE calculations usually underestimate the band gap of semiconductors. However, as already shown in the case of MAPbI$_3$,[21] the agreement here is due to a fortuitous cancellation of the errors of the GGA underestimated band gap and the lack of spin−orbit interactions which would tend to overestimate the gap. To test the robustness of the indirect band gap, we also used the HSE06 hybrid functional to calculate the electronic band structures of the MAPbI$_3$ by using the GGA−PBE + vdW-relaxed structures. The band structures of the MAPbI$_3$ calculated by the HSE-functional without SOC are also depicted in Figure 5e,f, and we can see that the

Manuscript publised in ACS Omega

ACS Omega http://pubs.acs.org/journal/acsodf Article

Table 2. Calculated Band Gaps (in eV) of the Studied MABX_3 Compounds for Different MA Orientations at Varying Levels of Approximation and Compared with the Available Experimental Data[a]

compounds	int. MA orient.	PBE	PBE+SOC	HSE	QSGW	QSGW+SOC	expt.
				calculated band gap (eV)			
MAPbI$_3$	[100]	1.55	0.47	1.99	2.47	1.79	1.55
	[110]	1.50	0.48				
	[111]	1.45	0.44	1.95	2.40	1.65	
MAPbBr$_3$	[100]	1.93	0.84	2.51	3.13	2.55	2.30
	[110]	1.86	0.84				
	[111]	1.80	0.70	2.43	3.01	2.28	
MAPbCl$_3$	[100]	2.41	1.30	3.10	3.91	3.49	2.90
	[110]	2.30	1.33				
	[111]	2.31	1.23	3.04	3.80	3.33	
MASnI$_3$	[100]	0.50	0.10	1.29			1.20
	[110]	0.47	0.10				
	[111]	0.49	0.10	1.26 (0.77)			
MASnBr$_3$	[100]	0.76	0.32	1.90			2.14
	[110]	0.76	0.38				
	[111]	0.75	0.30	1.88			
MASnCl$_3$	[100]	1.83	1.46	3.10			3.6
	[110]	1.33	1.03				
	[111]	1.49	1.06	2.94			

[a]Note: the HSE band gaps of Pb-based are obtained with 25% exact exchange, while the HSE band gaps of Sn-based are obtained with 55% exact exchange based on the experimental band gap of MASnI$_3$, and a number in parenthesis is obtained with 25% exact exchange.

indirect band gap persists when the screened hybrid functional is included. However, the calculated band gap of the MAPbI$_3$ by using the HSE06 lies in the range of 1.90−1.95 eV (see Table 2), larger than that one from the experimental value, as expected.

We note that indirect gaps or, more specifically, a displacement of the CBM away from the high symmetry point has previously been obtained due to the Rashba[15] effect. However, the results here are obtained without SOC and thus have a different origin: namely the distortions of the inorganic framework in response to the orientation of the MA molecules. The B-$6p$ contributes to the CMB, while the X-$5p$ and B-$6s$ contribute to the VMB of these materials. From our calculated results, it is clear that the molecular orientation can strongly influence the electronic structure of the hybrid perovskites by affecting the X−B−X inorganic framework which take part in the frontier orbital and a little bit change the band gap of the materials, which will be discussed in the next section.

For the other studied compounds, the direct band gaps are also found in the case of the [111] orientation, while the indirect band gaps are found in all cases of distorted BX_6 octahedral due to the cation rotation. However, the GGA−PBE calculations now underestimate the band gap, as shown in Table 2, when compared with the experimental values. This shows that the good agreement for MAPbI$_3$ is really a coincidence, and less perfect cancellation of errors occurs in the other cases. The full band structures in GGA−PBE without SOC have significant errors even for methylammonium lead iodide. The electronic band structures of the other compounds are depicted in Figure 6. We can also see that the indirect band gaps persist for all studied compounds in the case of initial [100] orientation when the screened hybrid functional is included. The HSE-calculated band gap without SOC of MAPbBr$_3$ and MAPbCl$_3$ lies between 2.43 and 2.51 eV and 3.04 and 3.10 eV, respectively (see Table 2), which is slightly larger than the experimental values. The HSE-calculated band gap without SOC of Sn-based compounds lies in the 1.26−

1.29 eV range for MASnI$_3$, 1.88−1.90 eV for MASnBr$_3$, and 2.94−3.10 eV for MASnCl$_3$ which is slightly smaller than the experimental values (see Table 2).

While the above study indicates that the indirect gap found in the structures obtained from the initial [100] direction of the molecule is robust when considering different functionals, we need to further study the combined effect of SOC and the gap corrections beyond semilocal functionals. In fact, the distortion-induced shift of the CBM may be related to the closeness of the bands which remain nearly degenerate at the R-point when SOC is neglected. One might expect that adding SOC could remove this effect. However, when we add SOC alone without using hybrid functionals to open the gap, the latter will be so strongly reduced that the CBM is then close to the VBM and this may then lead to other artifacts. Instead of combining HSE with SOC, we decided here to use the QSGW+SO because it is in principle an even more accurate approach.

The band structures of the Pb-based compounds in QSGW approximation and at the GGA−PBE-relaxed structures are shown in Figure 7. We can see from our calculated results that the QSGW band structures of the initial [111] MA orientation exhibit the direct band gap at R-point both with and without SOC. On the other hand, the QSGW band structures of the near [10−1] MA$^+$ orientation are different: the CBM is slightly shifted from $R \rightarrow \Gamma$ as found in our DFT band structures without SOC. This indirect nature is already obtained in QSGW even without SOC. Nonetheless, the band structures are still substantially different when SOC is included, namely, they are spin-split and the origin of the indirect gap is now clearly affected by the Rashba effect.

Our calculated QSGW band structures in the case of MAPbI$_3$ are qualitatively consistent with the studies of Brivio et al.[15] results in which the representative [100] configuration of the MA$^+$ cation was selected. In their work, a similar spin-splitting of the CBM and a shift of the CBM away from the R-point is found. On the other hand, for a smaller NH$_4$ molecule instead of the MA, this Rashba effect is not observed. This is

Manuscript published in ACS Omega
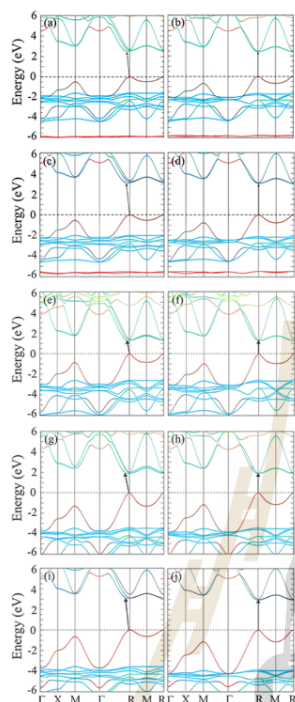
Figure 6. HSE-calculated band structures without SOC of the other studied compounds. (a,b) for MAPbBr$_3$, (c,d) for MAPbCl$_3$, (e,f) for MASnI$_3$, (g,h) for MASnBr$_3$, and (i,j) for MASnCl$_3$. Left and right panels represent the MA$^-$ cations initially orientated along [100] and [111] directions, respectively.
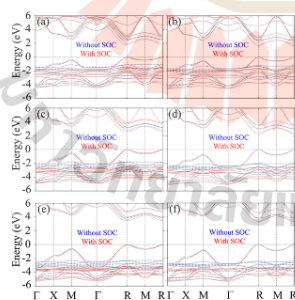

Figure 7. Calculated band structures in QSGW approximation with (red) and without (blue) SOC of the (a,b) CH$_3$NH$_3$PbI$_3$, (c,d) CH$_3$NH$_3$PbBr$_3$, and (e,f) CH$_3$NH$_3$PbCl$_3$. Left and right panels represent the MA$^-$ cation initially orientated along [100] and [111] directions, respectively.

because the NH$_4$ molecule has a much smaller molecular dipole character than the MA molecule. In recent work, the size of this effect was studied as a function of local distortions

obtained from molecular dynamics snapshots and found to be present even in CsPbI$_3$ due to the possibility of local Pb off-centering which like the MA molecules also can lead to the required symmetry breaking to have a Rashba effect.[15] Their calculated QSGW band gaps are 2.70 eV (SOC = 0) and 1.67 eV (added SOC). Our calculated band gaps in QSGW approximation are also listed in Table 2. We can see that the QSGW band gaps calculated without SOC are much larger than the experimental values, and the gaps are reduced by approximately 0.7 ± 0.1 eV when the SOC is considered. We note here that the orientations of the MA$^-$ cation are found to have an important impact on the nature of the band gap also at the level of QSGW approximation.

To further describe the indirect band gap, let us define the energy difference between the CBM and the conduction band at R-point of the Brillouin zone, $\Delta E \equiv E^R - E^{CBM}$, as shown by an inset in Figure 9. The PBE calculated ΔE of the studied
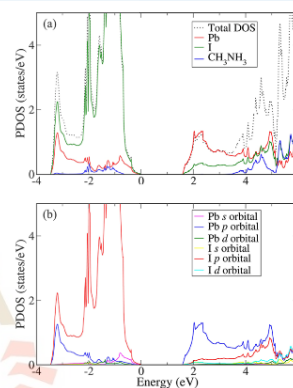
Figure 8. (a) Calculated total density of states (DOS) (dashed line) of CH$_3$NH$_3$PbI$_3$ for the case of [111]-oriented molecule and projected DOS (PDOS) on the Pb atom (red), I-atoms (green), and CH$_3$NH$_3$ (blue). (b) PDOS on orbitals of the Pb atom and I atoms.

compounds is depicted in Figure 9. From our calculated results, we can see that the ΔE of the Pb-based compounds is larger than that of the Sn-based compounds. This is resulting from the more distorted structure of the Pb-based compounds compared to the Sn-based ones. We note that the band gap
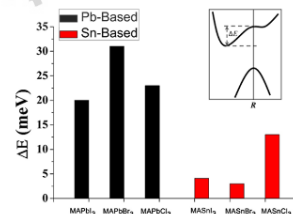

Figure 9. PBE-calculated energy difference, ΔE between the CBM and the conduction band at R-point (π/a, π/a, and π/a) of the Brillouin zone in the case of the indirect band gap.

Manuscript published in ACS Omega

shifting does not occur only with the $[10-1]$ orientation, the indirect band gap does appear for the equivalent orientations, for examples, $[10\pm1]$, $[01\pm1]$, and $[1\pm10]$. In addition, in the case of the $[101]$ orientation, the CBM shifts along the $R \to M$ line (Supporting Information, Figure S1).

The MA$^+$ cation has often been assumed to not have any significant contribution to the electronic structure around the band edges. From our calculated DOS results of MAPbI$_3$, it is obviously seen that the bottom of the conduction band mainly consists of the p orbitals of the Pb atom, while the top of the valence band is mainly derived from the p orbital of the I atoms and the Pb-s orbital, as depicted in Figure 8b. When considering the organic molecule, the highest occupied molecular orbital of the MA$^+$ cation is found deep below the valence band, $\sim$5 eV below the VBM. Thus, one may argue that there is no effect of the MA$^+$ cation in the optical and electronic response of such materials, rather it does only contribute to their structural cohesion by donating its charge to the rest of the system. However, a closer inspection of the DOS projected on the various atoms (Figure 8a) reveals that there is a small contribution of the MA cation, $\sim$0.5 eV below the VBM. This indicates that indeed there is an interaction between the MA cation and the inorganic PbI$_6$ octahedral framework in the form of hydrogen bonding. To further understand the effect of the interactions between the MA cation and the inorganic framework in electronic properties of these materials, we removed the MA cation from the PBE + vdW-relaxed structure of the initial $[100]$ orientation and calculated the electronic band structures. This is to check the interactions between the MA cation and the framework. Note that, by removing the MA cation, one electron is missing from the band, therefore there is a hole in the valence band and the Fermi-level shifted down, below the VBM. To do charge neutralizing, we added one electron to the system and then calculated the band structure. The calculated band structure in this case preserves the same feature of indirect band gap as one obtained from the MAPbI$_3$ unit cell (Supporting Information, Figure S2). This indicates that the MA cation in the system just donates its electron to the inorganic framework, it does not affect the band structure near the band edge. However, its orientations played a role in the relaxed structure of the inorganic framework and caused the structural distortion of the framework, leading to the symmetry breaking and the CBM is a bit shifted away from high symmetry point. In our cases, the rotation of the MA cation can create a variation of the band gap of MAPbI$_3$ $\sim$0.2 eV ($\sim$13% wrt. experimental gap of 1.55 eV), as shown in Figure 4d–f. Therefore, in the real system, the cation rotations would slightly change the band gap. The lowest and highest band gaps are found to be 1.43 and 1.64 eV which correspond to the calculated absorption spectrum of $\sim$865 and $\sim$756 nm, respectively. It is expected that the variation of the band gap for this material would be within 0.2 eV. The average band gap of MAPbI$_3$ is 1.54 eV which corresponded to the calculated absorption spectrum $\sim$805 nm. From all our calculated results, it has been revealed that the vdW correction is important to obtain an accurate description of the interactions between the MA cation and the inorganic framework for the structural relaxation of the halide perovskite system. This interaction induces the deformation of the PbI$_6$ octahedral framework, leading to the distorted structure of PbI$_6$ framework; the band structure is changed from direct to indirect band gap.

■ CONCLUSIONS

In this work, we have performed DFT + vdW correction calculations with various initial MA$^+$ cation orientations, namely $[100]$, $[110]$, and $[111]$ for revealing the effects of the internal interactions between the MA$^+$ cation and the BX_6 inorganic framework of the CH$_3$NH$_3$$BX_3$ (B = Pb, Sn; X = I, Br, Cl) halide perovskite materials. Our calculations reveal that the vdW interactions between the MA$^+$ cation and the inorganic framework are critical for internal geometry optimization and electronic properties calculations. Full structural relaxations, including vdW-corrected DFT, give the better agreement of the lattice parameters with the experimental values than obtained without them. More importantly, full relaxations, including vdW interactions of the MA cation initially oriented along the $[100]$ direction, give a strongly distorted structure of the BX_6 inorganic framework, which results from the MA$^+$ cation rotation and consequently affects the electronic band structure, which changes from direct to indirect band gap. On the other hand, the relaxations without vdW correction do not present enough distortion of the BX_6 inorganic framework, the electronic band structures remain direct band gap.

This result is found to be robust when considering different halogens and occurs in both Sn- and Pb-based compounds. It is also robust when using a more accurate hybrid functional or the GW method. Finally, the indirect gap is maintained for this orientation when including both quasiparticle self-energy corrections at the GW level and SOC. The latter leads to the Rashba effect which spin-splits the bands, but the indirect nature is already present before adding the SOC. This clearly demonstrates that the main origin of the indirect gap lies in the distortions resulting from the structural distortions of the organic ion with the inorganic framework.

Computational Methods. The structural properties of studied materials were predicted using the first-principle DFT which is implemented in the Vienna *ab initio* simulation package (VASP) code.[22,23] The semilocal GGAs combined with the PBE[24] functional are used as the primary exchange–correlation functional. The vdW corrections were also employed to study their effects on the structural and electronic properties of the materials. The projected augmented wave[23,25] method with plane-wave basis set cut-off energy of 520 eV is employed in all calculations. The conjugate gradient algorithm[26] is used for the structural optimization until the change of the energy on each atom is less than 1×10^{-4} eV. For the structural optimization and electronic properties calculations, the Monkhorst–Pack k-points sampling[27] with 8 $\times$ 8$\times$8 mesh is used for the Brillouin-zone integrations. Recent studies[12–14] revealed that vdW force plays an important role in the range of materials with weak interactions, such as organic–inorganic halide perovskite compounds, especially in their geometry optimization. Therefore, in order to study the effects of internal interactions between the MA$^+$ cation and BX_6 inorganic framework, full structural relaxations (volume and atomic position are allowed to relax), including vdW interactions, have been performed using the zero damping DFT-D3 method described by Grimme et al.[28] Then, the relaxed structures have been used to calculate the corresponding electronic band structures both at the DFT and many-body perturbation theory GW level.[29–31]

The cubic primitive cell of the MABX_3 (12 atoms per unit cell) has been used in this work. As a matter of fact, under

Manuscript published in ACS Omega

working temperature, the MA molecules are nearly free to rotate inside the cuboctahedral BX_6. It is more important to investigate the range of the change in the energy level near the band edge. In this work, various MA orientations within the cubic unit cell have been studied in order to determine the range of variation of electronic structures as molecules rotating inside the perovskite cage. Our calculated results are able to qualitatively explain the change of CBM of MAPbI$_3$ which is affected by molecular rotational and is in good agreement with both other calculations using the supercell approach[13,16,19] and the experiment performed by Hutter et al.[32] The orientation of the MA cation significantly affects the BX_6 inorganic framework and consequently the electronic properties of the materials.

It is well known that the GGA−PBE usually underestimates band gaps of semiconductors. However, for MAPbI$_3$, the GGA−PBE without SOC gives fortuitously good agreement of the calculated band gap with the experimental measurement. This is due to a compensation of the errors of the GGA−PBE and the lack of SOC. Therefore, the more accurate HSE-screened hybrid functional (HSE06)[33] is also used to calculate the band structures without including SOC for the band gaps. It is well known that the DFT method treats core electrons by effective pseudopotential. In order to study the effects of core electrons, one may need the full-potential all-electron methods to explain the electronic properties of the materials. Subsequently, to compare with the DFT method, we also calculated the band structures using the full-potential linearized muffin-tin orbital all-electron method,[34,35] as implemented in Questaal Suite.[31] In this method, the band structures are calculated using the QSGW method.[35,36] The GW method is a many-body perturbation theoretical method introduced by Hedin[37,38] in which the self-energy is approximated in terms of the one-electron Green's function G and screened Coulomb interaction, W, schematically $\Sigma = iGW$. While the GW self-energy operator is energy-dependent and non-Hermitian in the QSGW approach, we replace it by an energy-independent but still non-local operator, determined in a self-consistent manner. From a starting independent particle Hamiltonian H_0, and its eigenvalues and eigenfunctions, we obtain both the Green's function G_0 and the polarization function P_0. The screened Coulomb interaction is then given by $W = v + vP_0W$, and the self-energy is obtained as $\Sigma = iG_0W_0$. This quantity is actually obtained in the basis set of the eigenstates of H_0. From it, we then extract a correction to the exchange correlation potential

$$[\Delta v_{xc}]_{ij} = \frac{1}{2} \operatorname{Re} \left\{ \Sigma_{ij}(\varepsilon_i) + \Sigma_{ij}(\varepsilon_j) \right\} - v_{xc}^0$$

which is added to the previous H_0 to obtain a new H_0, and the procedure is iterated until $\Delta v_{xc} = 0$. At convergence, the quasiparticle energies equal the Kohn−Sham eigenvalues. Hence, the name quasiparticle self-consistent. The energy dependence of the GW self-energy and its imaginary part or lifetime are thus ignored, but the quasiparticle energies are correctly including the dynamical effects of the electron−electron interaction.

■ ASSOCIATED CONTENT

Ⓢ Supporting Information

The Supporting Information is available free of charge at https://pubs.acs.org/doi/10.1021/acsomega.0c03016.

Band structures of the fully relaxed crystal structure including vdW interactions calculated using the GGA−PBE without SOC of MAPbI3 for the MA cation initially orientated along the [101] direction; calculated band structures of the PBE + vdW-relaxed structure of the MAPbI3 unit cell with the MA cation initially orientated in the [100] direction; and calculated band structures of the PBE + vdW-relaxed structure of Pb−I host without the MA cation in the structure (PDF)

■ AUTHOR INFORMATION

Corresponding Author

Sirichok Jungthawan − *School of Physics, Institute of Science and Center of Excellence in Advanced Functional Materials, Suranaree University of Technology, Nakhon Ratchasima 30000, Thailand; Thailand Center of Excellence in Physics, Ministry of Higher Education, Science, Research and Innovation, Bangkok 10400, Thailand;* ⓞ orcid.org/0000-0003-0989-6512; Email: sirichok@g.sut.ac.th

Authors

Narasak Pandech − *School of Physics, Institute of Science, Suranaree University of Technology, Nakhon Ratchasima 30000, Thailand; Thailand Center of Excellence in Physics, Ministry of Higher Education, Science, Research and Innovation, Bangkok 10400, Thailand*

Thanundon Kongnok − *School of Physics, Institute of Science, Suranaree University of Technology, Nakhon Ratchasima 30000, Thailand; Thailand Center of Excellence in Physics, Ministry of Higher Education, Science, Research and Innovation, Bangkok 10400, Thailand*

Nirawith Palakawong − *School of Physics, Institute of Science, Suranaree University of Technology, Nakhon Ratchasima 30000, Thailand; Thailand Center of Excellence in Physics, Ministry of Higher Education, Science, Research and Innovation, Bangkok 10400, Thailand*

Sukit Limpijumnong − *School of Physics, Institute of Science, Suranaree University of Technology, Nakhon Ratchasima 30000, Thailand; The Institute for the Promotion of Teaching Science and Technology, Bangkok 10110, Thailand*

Walter R. L. Lambrecht − *Department of Physics, Case Western Reserve University, Cleveland, Ohio 44106-7079, United States;* ⓞ orcid.org/0000-0002-5377-0143

Complete contact information is available at:
https://pubs.acs.org/10.1021/acsomega.0c03016

Notes

The authors declare no competing financial interest.

■ REFERENCES

(1) Poglitsch, A.; Weber, D. Dynamic disorder in methylammoniumtrihalogenoplumbates (II)observed by millimeter-wave spectroscopy. *J. Chem. Phys.* **1987**, *87*, 6373−6378.

(2) Kojima, A.; Teshima, K.; Shirai, Y.; Miyasaka, T. Organometal Halide Perovskites as Visible-Light Sensitizers for Photovoltaic Cells. *J. Am. Chem. Soc.* **2009**, *131*, 6050−6051.

(3) Stoumpos, C. C.; Malliakas, C. D.; Kanatzidis, M. G. Semiconducting Tin and Lead Iodide Perovskites with Organic Cations: Phase Transitions, High Mobilities, and Near-Infrared Photoluminescent Properties. *Inorg. Chem.* **2013**, *52*, 9019−9038.

(4) Park, J.-S.; Choi, S.; Yan, Y.; Yang, Y.; Luther, J. M.; Wei, S.-H.; Parilla, P.; Zhu, K. Electronic Structure and Optical Properties of α-$CH_3NH_3PbBr_3$ Perovskite Single Crystal. *J. Phys. Chem. Lett.* **2015**, *6*, 4304−4308.

(5) Weller, M. T.; Weber, O. J.; Henry, P. F.; Di Pumpo, A. M.; Hansen, T. C. Complete structure and cation orientation in the perovskite photovoltaic methylammonium lead iodide between 100 and 352 K. *Chem. Commun.* **2015**, *51*, 4180−4183.

(6) Sahoo, S. K.; Manoharan, B.; Sivakumar, N. Chapter 1—Introduction: Why Perovskite and Perovskite Solar Cells? In *Perovskite Photovoltaics*; Thomas, S., Thankappan, A., Eds.; Academic Press, 2018; pp 1−24.

(7) Tonui, P.; Oseni, S. O.; Sharma, G.; Yan, Q.; Tessema Mola, G. Perovskites photovoltaic solar cells: An overview of current status. *Renewable Sustainable Energy Rev.* **2018**, *91*, 1025−1044.

(8) Shi, Z.; Jayatissa, A. Perovskites-Based Solar Cells: A Review of Recent Progress, Materials and Processing Methods. *Materials* **2018**, *11*, 729.

(9) Whitfield, P. S.; Herron, N.; Guise, W. E.; Page, K.; Cheng, Y. Q.; Milas, I.; Crawford, M. K. Structures, Phase Transitions and Tricritical Behavior of the Hybrid Perovskite Methyl Ammonium Lead Iodide. *Sci. Rep.* **2016**, *6*, 35685.

(10) Quarti, C.; Mosconi, E.; De Angelis, F. Interplay of Orientational Order and Electronic Structure in Methylammonium Lead Iodide: Implications for Solar Cell Operation. *Chem. Mater.* **2014**, *26*, 6557−6569.

(11) Knop, O.; Wasylishen, R. E.; White, M. A.; Cameron, T. S.; Oort, M. J. M. V. Alkylammonium lead halides. Part 2. $CH_3NH_3PbX_3$ (X = Cl, Br, I) perovskites: cuboctahedral halide cages with isotropic cation reorientation. *Can. J. Chem.* **1990**, *68*, 412−422.

(12) Egger, D. A.; Kronik, L. Role of Dispersive Interactions in Determining Structural Properties of Organic−Inorganic Halide Perovskites: Insights from First-Principles Calculations. *J. Phys. Chem. Lett.* **2014**, *5*, 2728−2733.

(13) Li, J.; Rinke, P. Atomic structure of metal-halide perovskites from first principles: The chicken-and-egg paradox of the organic-inorganic interaction. *Phys. Rev. B* **2016**, *94*, 045201.

(14) Yin, W.-J.; Shi, T.; Yan, Y. Unusual defect physics in $CH_3NH_3PbI_3$ perovskite solar cell absorber. *Appl. Phys. Lett.* **2014**, *104*, 063903.

(15) Brivio, F.; Butler, K. T.; Walsh, A.; van Schilfgaarde, M. Relativistic quasiparticle self-consistent electronic structure of hybrid halide perovskite photovoltaic absorbers. *Phys. Rev. B: Condens. Matter Mater. Phys.* **2014**, *89*, 155204.

(16) Motta, C.; El-Mellouhi, F.; Kais, S.; Tabet, N.; Alharbi, F.; Sanvito, S. Revealing the role of organic cations in hybrid halide perovskite $CH_3NH_3PbI_3$. *Nat. Commun.* **2015**, *6*, 7026.

(17) Bechtel, J. S.; Seshadri, R.; Van der Ven, A. Energy Landscape of Molecular Motion in Cubic Methylammonium Lead Iodide from First-Principles. *J. Phys. Chem. C* **2016**, *120*, 12403−12410.

(18) Chiarella, F.; Zappettini, A.; Licci, F.; Borriello, I.; Cantele, G.; Ninno, D.; Cassinese, A.; Vaglio, R. Combined experimental and theoretical investigation of optical, structural, and electronic properties of $CH_3NH_3SnX_3$ thin films (X=Cl, Br). *Phys. Rev. B: Condens. Matter Mater. Phys.* **2008**, *77*, 045129.

(19) Xu, Q.; Stroppa, A.; Lv, J.; Zhao, X.; Yang, D.; Biswas, K.; Zhang, L. Impact of organic molecule rotation on the optoelectronic properties of hybrid halide perovskites. *Phys. Rev. Mater.* **2019**, *3*, 125401.

(20) Lee, M. M.; Teuscher, J.; Miyasaka, T.; Murakami, T. N.; Snaith, H. J. Efficient Hybrid Solar Cells Based on Meso-Super-structured Organometal Halide Perovskites. *Sci* **2012**, *338*, 643.

(21) Mosconi, E.; Amat, A.; Nazeeruddin, M. K.; Grätzel, M.; De Angelis, F. First-Principles Modeling of Mixed Halide Organometal Perovskites for Photovoltaic Applications. *J. Phys. Chem. C* **2013**, *117*, 13902−13913.

(22) Kresse, G.; Furthmüller, J. Efficient iterative schemes for ab initio total-energy calculations using a plane-wave basis set. *Phys. Rev. B: Condens. Matter Mater. Phys.* **1996**, *54*, 11169−11186.

(23) Kresse, G.; Joubert, D. From ultrasoft pseudopotentials to the projector augmented-wave method. *Phys. Rev. B: Condens. Matter Mater. Phys.* **1999**, *59*, 1758−1775.

(24) Perdew, J. P.; Burke, K.; Ernzerhof, M. Generalized Gradient Approximation Made Simple. *Phys. Rev. Lett.* **1996**, *77*, 3865−3868.

(25) Blöchl, P. E. Projector augmented-wave method. *Phys. Rev. B: Condens. Matter Mater. Phys.* **1994**, *50*, 17953−17979.

(26) Golub, G. H.; Ye, Q. Inexact Preconditioned Conjugate Gradient Method with Inner-Outer Iteration. *SIAM J. Sci. Comput.* **1999**, *21*, 1305−1320.

(27) Monkhorst, H. J.; Pack, J. D. Special points for Brillouin-zone integrations. *Phys. Rev. B: Condens. Matter Mater. Phys.* **1976**, *13*, 5188−5192.

(28) Grimme, S.; Antony, J.; Ehrlich, S.; Krieg, H. A consistent and accurate ab initio parametrization of density functional dispersion correction (DFT-D) for the 94 elements H-Pu. *J. Chem. Phys.* **2010**, *132*, 154104.

(29) Bhandari, C.; Lambrecht, W. R. L.; van Schilfgaarde, M. Quasiparticle self-consistent GW calculations of the electronic band structure of bulk and monolayer V_2O_5. *Phys. Rev. B: Condens. Matter Mater. Phys.* **2015**, *91*, 125116.

(30) Bhandari, C.; van Schilfgaarde, M.; Kotani, T.; Lambrecht, W. R. L. All-electron quasiparticle self-consistent GW band structures for $SrTiO_3$ including lattice polarization corrections in different phases. *Phys. Rev. Mater.* **2018**, *2*, 013807.

(31) Pashov, D.; Acharya, S.; Lambrecht, W. R. L.; Jackson, J.; Belashchenko, K. D.; Chantis, A.; Jamet, F.; van Schilfgaarde, M. Questaal: A package of electronic structure methods based on the linear muffin-tin orbital technique. *Comput. Phys. Commun.* **2020**, *249*, 107065.

(32) Hutter, E. M.; Gélvez-Rueda, M. C.; Osherov, A.; Bulović, V.; Grozema, F. C.; Stranks, S. D.; Savenije, T. J. Direct−indirect character of the bandgap in methylammonium lead iodide perovskite. *Nat. Mater.* **2017**, *16*, 115−120.

(33) Heyd, J.; Scuseria, G. E.; Ernzerhof, M. Hybrid functionals based on a screened Coulomb potential. *J. Chem. Phys.* **2003**, *118*, 8207−8215.

(34) Methfessel, M.; van Schilfgaarde, M.; Casali, R. A. In *A Full-Potential LMTO Method Based on Smooth Hankel Functions, Electronic Structure and Physical Properties of Solids*; Dreyssé, H., Ed.; Springer Berlin Heidelberg: Berlin, Heidelberg, 2000; pp 114−147.

(35) Kotani, T.; van Schilfgaarde, M.; Faleev, S. V. Quasiparticle self-consistent GW method: A basis for the independent-particle approximation. *Phys. Rev. B: Condens. Matter Mater. Phys.* **2007**, *76*, 165106.

(36) van Schilfgaarde, M.; Kotani, T.; Faleev, S. Quasiparticle Self-Consistent GW Theory. *Phys. Rev. Lett.* **2006**, *96*, 226402.

(37) Hedin, L. New Method for Calculating the One-Particle Green's Function with Application to the Electron-Gas Problem. *Phys. Rev.* **1965**, *139*, A796−A823.

(38) Hedin, L.; Lundqvist, S. Effects of Electron-Electron and Electron-Phonon Interactions on the One-Electron States of Solids. In *Solid State Physics*; Seitz, F., Turnbull, D., Ehrenreich, H., Eds.; Academic Press, 1970; Vol. 23, pp 1−181.

Abstract presented at the American Physical Society Meeting

(APS March Meeting 2018)

First-principles Investigation of The Role of Organic Molecules Inside The α-phase of

Hybrid Halide Perovskite CH₃NH₃*BX*₃ (B= Pb, Sn; X= I, Br, Cl)

Narasak Pandech[a,b], Thanundon Kongnok[a,b],

Sirichok Jungthawan[a,b,c] , Sukit Limpijumnong[a,d], Walter R. L. Lambrecht[e]

[a]School of Physics, Institute of Science, Suranaree University of Technology, Nakhon Ratchasima 30000, Thailand

[b]Thailand Center of Excellence in Physics, Ministry of Higher Education, Science, Research and Innovation, 328 Si Ayutthaya Road, Bangkok 10400, Thailand

[c]Center of Excellence in Advanced Functional Materials, Suranaree University of Technology, Nakhon Ratchasima 30000, Thailand

[d]The Institute for the Promotion of Teaching Science and Technology, 924 Sukhumvit Road, Phra Khanong, Klong Toei, Bangkok 10110, Thailand

[e]Department of Physics, Case Western Reserve University, Cleveland, Ohio 44106-7079, USA.

Abstract

The hybrid halide perovskite materials, have attracted significant research attention because of their potential application in low cost highly efficient photovoltaics. While the device efficiencies have rapidly improved, the microscopic origin behind the success of these materials is still unclear. Especially, the presence of mobile cations in the $CH_3NH_3BX_3$, ($MABX_3$) materials is expected to play an important role in their fundamental properties. Here we performed a van der Waals-corrected density functional theory investigation of the MA^+ cation structural and electronic properties in the α-phase of $CH_3NH_3BX_3$ with B=Pb and Sn. Our results reveal that the MA^+ cation orientation influences the structural properties of the inorganic network and consequently effects the electronic properties of the materials. For example, if the MA^+ cation is oriented along a (101)-like direction, the BX_6 octahedral cage will be distorted and the band gap becomes indirect.

Abstract presented at the International Union of Materials Research Society – International Conference on Electronic Materials 2018 (IUMRS-ICEM 2018)

Abstract provided for iumrs-icem 2018 conference

First principles study on structural and electronic properties of Ge-based hybrid perovskites

Narasak Pandech[a,b,c], Thanundon Kongnok[a,b],

Sukit Limpijumnong[a,b], Walter R. L Lambrecht[c]

[a]School of Physics and NANOTEC-SUT Center of Excellence on Advanced Functional Nanomaterials, Suranaree University of Technology, Nakhon Ratchasima 30000, Thailand
[b]Thailand Center of Excellence in Physics (ThEP Center), Commission on Higher Education, Bangkok 10400, Thailand
[c]Department of Physics, Case Western Reserve University, Cleveland, Ohio 44106-7079, USA.

Recently, $CH_3NH_3PbI_3$ hybrid perovskite is of great interest as a high efficiency absorber for photovoltaic applications. However, Pb-containing materials have environmental issues. To explore environmental friendly materials, many Pb-free hybrid perovskites have been developed. Germanium (Ge^{2+}) is one of potential element to substitute Pb in hybrid perovskite. In this work, structural and electronic properties of $MAGeX_3$ ($X = I^-$, Br^-, Cl^-) were investigated by using van der Waals density functional theory (vdW-DFT). Results showed that the Ge-X bonds, which represent the covalent interactions, are separated into short-bonds and long-bonds. This is unlike the case of $MAPbI_3$. Regarding the effects of X-anions, we found that the bond lengths decrease when the X-anion changed from I^- to Cl^-. Consequently, the crystal structure is slightly distorted and the bandgap increases. Electronic property analyses revealed that the valence band maximum (VBM) is dominated by I p-orbital and Ge s-orbital, while the conduction band minimum (CBM) is dominated by Ge p-orbital. Our results provide a fundamental understanding for a new generation of photovoltaic materials.

Abstract presented at The 9th International Conference on Multiscale Materials Modeling (MMM 2018).

First-principles Study on Electronic Properties of Hybrid MABX_3 perovskites

(MA= CH$_3$NH$_3$$^+$; B = Pb, Sn, Ge; X = I, Br, Cl)

Narasak Pandech[a,b,c], Thanundon Kongnok[a,b], Sirichok Jungthawan[a.b,]

Sukit Limpijumnong[a,b], Walter R. L Lambrecht[c]

[a]*School of Physics and NANOTEC-SUT Center of Excellence on Advanced Functional Nanomaterials, Suranaree University of Technology, NakhonRatchasima 30000, Thailand.*
[b]*Synchrotron Light Research Institute, NakhonRatchasima 30000, Thailand*
[c]*Department of Physics, Case Western Reserve University, Cleveland, Ohio 44106-7079, USA.*

Recently, hybrid MABX_3 perovskites (MA= CH$_3$NH$_3$$^+$; B = Pb, Sn, Ge; X = I, Br, Cl) have revolutionized emerging photovoltaic technologies with the development of highly efficient solar cells, and have attracted significant fundamental research interest. Despite the extremely fast progress in device fabrication, the materials electronic properties, which determine the photovoltaic performance, are not yet fully understood. Here, we performed calculations of these materials, using a van der Waals-corrected density functional theory (DFT) method using the Perdew–Burke–Ernzerhof (PBE) and Heyd–Scuseria–Ernzerhof (HSE) hybrid functionals. Subsequently, we use the GW-approximation to calculate the bands as quasiparticle excitations including also the spin-orbit coupling. The orientation and position of the MA-cation is found to significantly affect the electronic properties around the band edges of the Pb and Sn based compounds. Because Ge based halides already prefer a rhombohedrally distorted perovskite structure with off-centered Ge even for a simple inorganic cation (e.g. Cs), the three-fold symmetry of the MA ion is compatible with a preferred orientation of the molecules along the rhombohedral axis. The interplay between its dipole and the Ge off-centering leads to interesting ferro-electric behavior.

CURRICULUM VITAE

Narasak Pandech was born on April 10, 1986 in Yasothon, one of the northeastern province of Thailand. He received his Bachelor degree of science with the second class honor in 2008 from the Department of Physics, Faculty of Science, Khon Kaen University. In 2009, he was granted the scholarship from the Development and Promotion of Science and Technology Talents Project (DPST, THAILAND) to pursue the master program at the School of Physics, Suranaree University of Technology under the supervision of Prof. Dr. Sukit Limpijumnong and he received his Master degree of science in 2013. In 2014, he was continuously granted the scholarship from the DPST to study the Ph.D. program at the same school under the supervision of Prof. Dr. Sukit Limpijumnong and Assoc. Prof. Dr. Sirichok Jungthawan. In 2017, he visited the Electronic Structure Group with supervised of Prof. Dr. Walter R. L. Lambrecht at Case Western Reserve University (CWRU), Ohio, USA. He interested in condense matter physics using first principles and density functional calculations. He has published the articles in the international journals and participated in several national and international conferences during the course of his Ph.D. program education. Detail of the publications and abstracts of his presentations can be found in the APPENDIX.